THE UNIVERSITY of ADELAIDE

Department of Earth Science

School of Physical Sciences

Faculty of Sciences

Improving Next-Generation Hydrogeological Models with Geophysics

Ho Yin Li (Chris)

PhD Thesis

August 2020

In fulfilment of the requirement for the degree of Doctor of Philosophy
in the subject of Hydrogeophysics

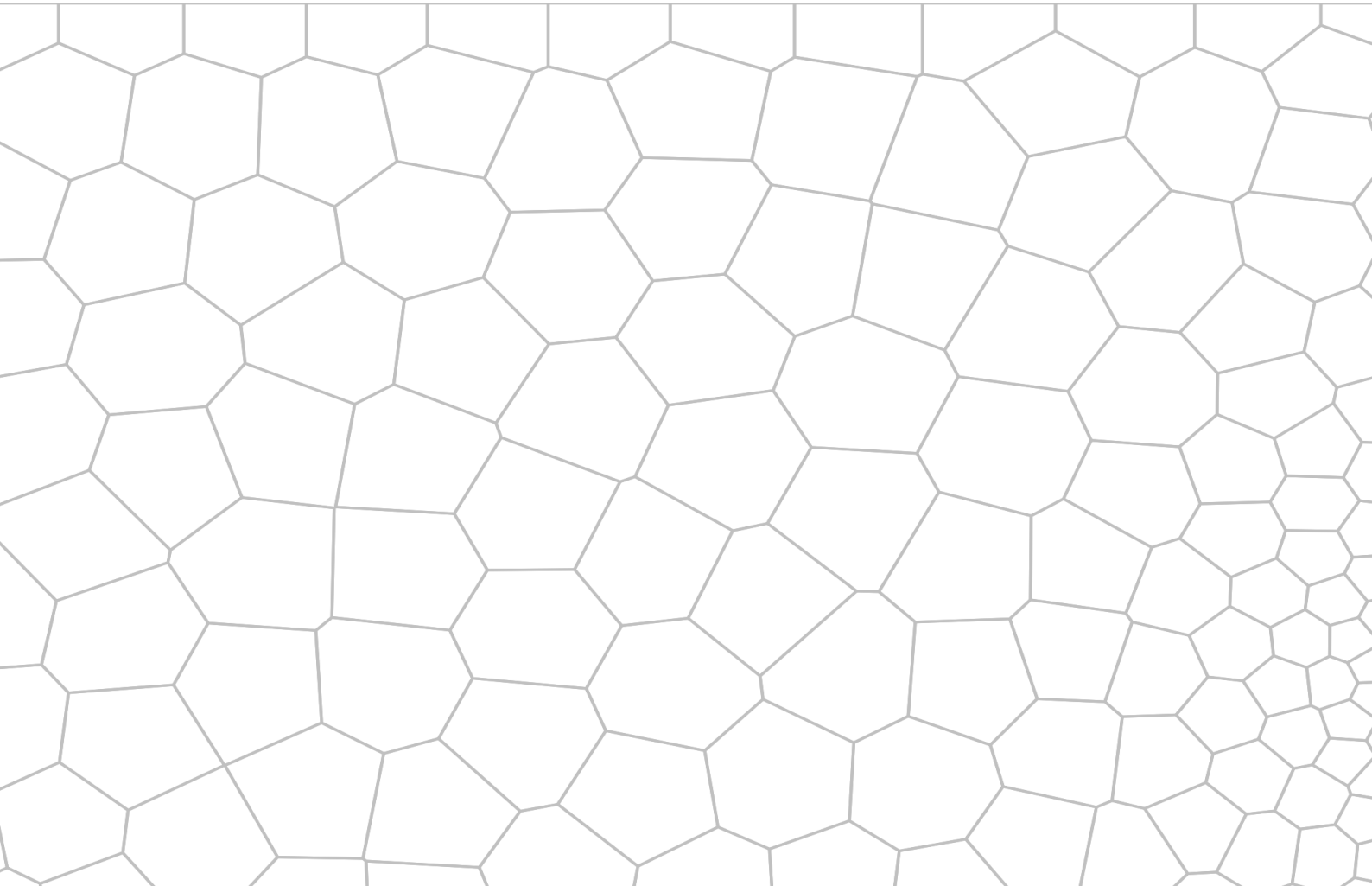

Table of Contents

Abstract

This thesis presents advancements to the disciplines of geophysics and hydrogeological modelling. There are three main scientific contributions in this work. In Chapter 1 I propose a method to couple time-domain electromagnetics (TEM) and surface nuclear magnetic resonance (NMR) datasets with limited drillhole data to provide information on hydrogeological properties in a non-invasive manner, including groundwater salinity and hydraulic conductivity. This method reduces ambiguity in the hydrogeological interpretation of TEM-derived conductivity information by coupling conductivity to porosity values estimated using surface NMR data collected in the same field area. The method was applied to a South Australian River Murray floodplain to investigate the impact of artificial watering on the shallow groundwater salinity. In Chapter 2 I evaluate the impact of incorporating TEM and surface NMR datasets on the prediction error and uncertainty of groundwater models under different hydrogeological conditions using a synthetic approach. A method is presented to couple TEM and surface NMR to derive hydraulic conductivity using the Markov-Chain Monte Carlo method. In Chapter 3 I propose a modelling framework to couple multiple geophysical techniques, including TEM, borehole NMR and audio-frequency magnetotellurics (AMT), with stochastic groundwater modelling through the ensemble-smoother method. This approach allows the uncertainty in geophysical data to be expressed as a prior probability distribution that can be incorporated and accounted for in groundwater model inversion. This framework is applied to a potential in-situ recovery site in Kapunda, South Australia to estimate the regional-scale impact of a hypothetical operation trial in a probabilistic manner. Together, these three novel studies represent a contribution to the coupling between geophysics and hydrogeological modelling.

Thesis Declaration

I certify that this work contains no material which has been accepted for the award of any other degree or diploma in my name, in any university or other tertiary institution and, to the best of my knowledge and belief, contains no material previously published or written by another person, except where due reference has been made in the text. In addition, I certify that no part of this work will, in the future, be used in a submission in my name, for any other degree or diploma in any university or other tertiary institution without the prior approval of the University of Adelaide and where applicable, any partner institution responsible for the joint-award of this degree.

I acknowledge that copyright of published works contained within this thesis resides with the copyright holder(s) of those works.

I also give permission for the digital version of my thesis to be made available on the web, via the University's digital research repository, the Library Search and also through web search engines, unless permission has been granted by the University to restrict access for a period of time.

I acknowledge the support I have received for my research through the provision of an Australian Government Research Training Program Scholarship and a CSIRO Research Plus Scholarship. In addition, I acknowledge the funding I have received for my research from the Department for Environment and Water of South Australia and the Cooperative Research Centres Projects Grant entitled "Kapunda In-Situ Copper and Gold Field Recovery Trial".

Ho Yin Li (Chris)

26 August 2020

Acknowledgements

First and foremost, I would like to thank my supervisors Rebecca Doble, Michael Hatch and Graham Heinson for their guidance and support throughout my PhD. I would also like to thank Luk Peeters and Chris Turnadge for their advice on groundwater modelling, and Brady Flinchum, Kevin Cahill and Aaron Davis for their guidance in geophysical inversion and field surveys.

I would like to acknowledge the project support from CSIRO, the University of Adelaide, EnviroCopper, Groundwater Science, Flinders University and the Department for Environment and Water of South Australia (DEW), which made this thesis work possible. A special thanks to my DEW colleagues, especially Graham Green, Juliette Woods and Virginia Riches for making it possible for me to undertake my PhD whilst working, as well as my team members for their continuous support and encouragement. I would also like to thank my fellow PhD students and researchers at CSIRO and the University of Adelaide for providing me with an enjoyable working atmosphere.

Finally, I would like to thank my family and friends, especially my wife Helen for her selfless support and patience.

1 Introduction

1.1 Overview of groundwater modelling

Groundwater is water that exists below the land surface in the saturated zone (Fetter, 2018). From a global perspective, groundwater is important as it accounts for approximately 99% of the planet's liquid fresh water (Shiklomanov, 1993). It is the primary water source for more than two billion people (Alley et al., 2002) and provides more than half of the irrigation water used to grow the world's food (Siebert et al., 2010). Groundwater also serves as an emergency reserve in times of drought (Famiglietti, 2014) and supports numerous native species and ecosystem worldwide (Rohde et al., 2017). Therefore, proper management of groundwater resources is essential and there is a need for tools to assist decision-making (Ferré, 2017).

Numerical modelling is commonly used to inform and support management decisions about groundwater resources (Doherty and Simmons, 2013). It is a process of mathematically representing the key physical processes of a groundwater system and enables the prediction of impact from different management options based on the currently available data and knowledge (Anderson et al., 2015). Numerical groundwater modelling has been applied to solve numerous environmental problems. For example, Narayan et al. (2007) applied a variable density flow and solute transport model to predict the extent of seawater intrusion under a variety of recharge and pumping conditions in the Burdekin Delta, Australia. Joyce et al. (2014) used multi-scale groundwater flow modelling to assess the safety of a geological repository for spent high-level nuclear fuel in Forsmark, Sweden. Almasri and Kaluarachchi (2007) applied a flow and solute transport model to simulate the impact of land use practices and management options on the nitrate pollution of groundwater in Washington, United States.

Traditionally, groundwater modelling involves calibrating the model against field data such as groundwater level observations (Hill and Tiedeman, 2006). Once calibrated, the model is used to make predictions based on the notion that if the model can reproduce the past, it can predict the future (Doherty and Vogwill, 2016). Despite being calibrated, groundwater models can still have large prediction errors (Freyberg, 1988). There are a number of possible explanations for these discrepancies. First, groundwater models are non-unique in that there are potentially many parameter combinations that can achieve a similar fit to the observations (McKenna et al., 2003). Second, it remains challenging to parameterise groundwater models with accurate conceptualisations and quantitative hydrogeological parameters, resulting in a large uncertainty in their predictions (Højberg and Refsgaard, 2005). Third, historical observations may not

contain the information needed to constrain parameters that have a significant bearing on the prediction (Moore and Doherty, 2005). For example, historical observations collected from an area that has never been subject to coal seam gas development may not provide constraints on parameters that are critical for coal seam gas simulation (Moore et al., 2015, Cui et al., 2018).

The root of these problems may lie within our inadequate characterisation of the subsurface, as classical hydrogeological techniques provide mostly point-scale information, while groundwater models generally require spatially-continuous data (Brunner et al., 2006). It is therefore desirable to complement groundwater models with techniques that can provide hydrogeological information at a higher spatial density.

1.2 Coupling geophysics with groundwater modelling

There is a wide range of geophysical techniques that can provide information on hydrogeological properties, such as electromagnetics, nuclear magnetic resonance, magnetotellurics, ground penetrating radar, seismic and gravity (Telford et al., 1990). This thesis focuses on two geophysical techniques: time-domain electromagnetics (TEM) and nuclear magnetic resonance (NMR). These geophysical techniques can complement groundwater models due to their denser spatial coverage (compared to drillhole-based hydrogeological techniques), non-invasiveness and relatively low cost on an areal basis compared to classical hydrogeological techniques (Slater, 2007).

TEM is commonly used to assist groundwater modelling. For example, Marker et al. (2015) used TEM to improve the hydrostratigraphic characterisation of a hydrological model to estimate groundwater levels in Norsminde, Denmark. Herckenrath et al. (2013) parameterised a saltwater intrusion model using TEM data for Pajaro Valley, California.

Although not as commonly used in groundwater modelling as TEM, NMR is gaining traction in hydrogeological modelling due to its ability to detect subsurface water directly and estimate hydrogeological parameters such as porosity and hydraulic conductivity. For example, Boucher et al. (2012) applied NMR to estimate transmissivity and specific yield for a groundwater model to assess recharge for a sandstone aquifer in Niger. Lubczynski and Gurwin (2005) applied NMR to derive storativity and improve the hydrogeological conceptualisation and stratigraphy for a groundwater model to assess groundwater recharge and evapotranspiration in Sardon, Spain.

However, it is challenging to couple these geophysical techniques with groundwater models as the techniques rarely provide direct quantification of hydrogeological properties (Rubin and Hubbard, 2006). For example, electrical conductivity (EC) from TEM is related to fluid salinity,

clay content, saturation, mineralogy and, to some extent, temperature (Everett, 2013, Telford et al., 1990). This causes ambiguity in the hydrogeological interpretations of EC data, which has the potential to lead to incorrect hydrogeological conceptualisation (Legchenko et al., 2009).

In addition to hydrogeological interpretations, geophysical data can be used to derive hydraulic parameters via petrophysical relationships (Slater, 2007). For instance, bulk EC from TEM can be related to porosity and fluid EC via Archie's Law (Archie, 1942). Zghibi et al. (2016) derived porosity from electrical resistivity tomography via Archie's Law for a groundwater flow and solute transport model to predict the tracer movement in the Paris Basin, France.

Another example of petrophysical relationship is the Schlumberger-Doll Research equation, which relates saturated porosity and the decay time constant T_2 from NMR to hydraulic conductivity (Kenyon et al., 1988). Vilhelmsen et al. (2014) estimated hydraulic conductivity from NMR data via the Schlumberger-Doll Research equation for simulating an aquifer system in Platte River Valley, Nebraska.

Petrophysical relationships often contain empirical constants that need to be calibrated against field data (Slater, 2007). However, due to non-uniqueness, there are different combinations of empirical constants that can achieve a similar fit to the field data (Cardiff et al., 2010). Additionally, there are usually limited literature values to provide constraints for the empirical constants, hence petrophysical relationships can contain a large degree of uncertainty (Moore et al., 2011). When using petrophysical relationships to derive observations for groundwater modelling, it is critical to quantify and account for the uncertainty in these observations to avoid incorrectly biasing modelling outcomes (Brunetti and Linde, 2018).

1.3 Objectives and contributions

The objective of this thesis is to investigate how geophysical techniques can be used to assist and improve hydrogeological modelling in a quantitative manner. There are three main contributions to the discipline of hydrogeophysics, which are presented:

1. Classical hydrogeological techniques generally involve collecting data from drillholes, which may be limited in, for example, environmentally sensitive areas. A coupling method is presented in this thesis to use TEM and NMR measurements with limited drillhole data to infer groundwater salinity and hydraulic conductivity, which can be useful for groundwater flow and solute transport modelling.
2. The point-scale nature of hydrogeological data rarely satisfies the continuous data requirement of groundwater models. This mismatch can be mitigated using geophysics due

to its denser spatial coverage. A method is presented in this chapter to use TEM and surface NMR to derive hydraulic conductivity for groundwater models. The impact of this method on the prediction error and uncertainty of groundwater models is evaluated in a systematic manner using a synthetic approach.

3. Geophysical data are commonly coupled with groundwater modelling in an explicit and deterministic manner. Additionally, the uncertainty in geophysical data is rarely quantified and accounted for in groundwater model inversion, potentially biasing modelling outcomes. A modelling framework is presented in this chapter to couple multiple geophysical techniques with stochastic groundwater modelling. This framework enables the expression of uncertainty in geophysical data as a prior probability distribution that can be incorporated into groundwater model inversion.

1.4 Thesis outline

This thesis is structured as follows. Chapter 2 describes the theory of groundwater modelling, the two geophysical techniques of NMR and TEM, and hydrogeophysical coupling. In Chapter 3, a method is presented to use TEM and NMR with limited drillhole data to estimate groundwater salinity and hydraulic conductivity; this Chapter has been published in the journal *Hydrological Processes* (Li et al., 2020). Chapter 4 describes a synthetic study that uses TEM and NMR to derive hydraulic conductivity for groundwater modelling and evaluates the impact of these geophysical techniques on the prediction error and uncertainty of groundwater models. This work has been submitted to the journal *Geophysics* as a paper. In Chapter 5, a modelling framework is presented that couples multiple geophysical techniques, including TEM, NMR and audio-frequency MT, with stochastic groundwater modelling. This framework enables the uncertainty in geophysical data to be expressed and accounted for in groundwater model inversion. This work has been submitted to the *Journal of Hydrology* as a paper. Finally, Chapter 6 provides an overview of the main contributions of this thesis and recommendations for future research in hydrogeophysical modelling.

2 Background

2.1 Groundwater modelling theory

Groundwater flow in 1-dimensional porous media is described by Darcy's Law (Darcy, 1856) as follows:

$$Q = -KA\frac{dh}{dl} \qquad 2.1$$

where Q is the rate of groundwater discharge (m^3/d), K is hydraulic conductivity (m/d), A is the cross-sectional area perpendicular to the groundwater flow direction (m^2), dh (m) and dl (m) are the head difference and distance between two points respectively. Equation 2.1 shows that groundwater discharge is proportional to hydraulic conductivity, the cross-sectional area normal to the flow direction and the hydraulic gradient (i.e. $\frac{dh}{dl}$). The negative sign is included because groundwater flows towards the lower head value. Another relevant quantity is specific discharge q (m/d), which represents the apparent velocity at which groundwater would flow through an aquifer if the aquifer was an open conduit and is defined as follows:

$$q = \frac{Q}{A} \qquad 2.2$$

Darcy's Law (Equation 2.1) provides the basis for the partial-differential equation that governs three-dimensional transient groundwater flow (Rushton and Redshaw, 1979) as follows:

$$\frac{\partial}{\partial x}\left(K_x\frac{\partial h}{\partial x}\right) + \frac{\partial}{\partial y}\left(K_y\frac{\partial h}{\partial y}\right) + \frac{\partial}{\partial z}\left(K_z\frac{\partial h}{\partial z}\right) = S_S\frac{\partial h}{\partial t} - W \qquad 2.3$$

where the three terms on the left represent changes in specific discharge for a unit volume of porous medium along the x, y and z axes respectively. Together they represent the net change in water volume, which is balanced by changes in storage (the first term on the right) and a source and sink term W. The term S_S refers to specific storage (m^{-1}) and represents the water volume released from storage per unit change in head per unit volume of porous medium. The sink and source term W accounts for various hydrogeological processes such as groundwater extraction and recharge.

MODFLOW (Harbaugh, 2005) is a numerical code that is commonly used for groundwater modelling. Consider a grid of model cells with i, j and k representing column, row and layer. MODFLOW solves the partial-differential equation (Equation 2.3) for $\text{cell}_{i,j,k}$ using a finite-difference approach as follows:

$$\begin{aligned} &C_{i,j-\frac{1}{2},k}\left(h_{i,j-1,k}^{m}-h_{i,j,k}^{m}\right)+C_{i,j+\frac{1}{2},k}\left(h_{i,j+1,k}^{m}-h_{i,j,k}^{m}\right)+\\ &+C_{i-\frac{1}{2},j,k}\left(h_{i-1,j,k}^{m}-h_{i,j,k}^{m}\right)+C_{i+\frac{1}{2},j,k}\left(h_{i+1,j,k}^{m}-h_{i,j,k}^{m}\right)\\ &+C_{i,j,k-\frac{1}{2}}\left(h_{i,j,k-1}^{m}-h_{i,j,k}^{m}\right)+C_{i,j,k+\frac{1}{2}}\left(h_{i,j,k+1}^{m}-h_{i,j,k}^{m}\right)\\ &+P_{i,j,k}h_{i,j,k}^{m}+Q_{i,j,k}=S_{i,j,k}\frac{h_{i,j,k}^{m}-h_{i,j,k}^{m-1}}{t^{m}-t^{m-1}} \end{aligned} \qquad 2.4$$

where C is the hydraulic conductance (m^2/d) between $\text{cell}_{i,j,k}$ and its adjacent cell (the $\frac{1}{2}$ in the i,j,k indexing refers to the interface between cells), m is stress period (i.e. a time period where there are no changes in groundwater stresses such as pumping and recharge), $P_{i,j,k}h_{i,j,k}^{m}$ is a head-dependent sink and source term, $Q_{i,j,k}$ is a head-independent sink and source term, S is specific yield (i.e. the water volume released from storage per unit change in head per unit area of porous medium; unitless) for unconfined condition or the product of specific storage and cell volume for confined condition, and t is time (d). Using $C_{i,j-\frac{1}{2},k}$ as an example, hydraulic conductance is defined as:

$$C_{i,j-\frac{1}{2},k}=\frac{K_{i,j-\frac{1}{2},k}A_{i,j-\frac{1}{2},k}}{dl_{i,j-\frac{1}{2},k}} \qquad 2.5$$

where K is usually the harmonic mean (other mean options are available) of hydraulic conductivity between $\text{cell}_{i,j,k}$ and $\text{cell}_{i,j\text{-}1,k}$, $A_{i,j-\frac{1}{2},k}$ is the saturated area of interface between the two cells, and $dl_{i,j-\frac{1}{2},k}$ is the distance between the nodes of the two cells. Equation 2.5 combines the K, A and dl terms in Equation 2.1 into a single term as hydraulic conductance.

Equation 2.4 is applied to every model cell to form an array of equations, which is solved by MODFLOW using an iterative approach (Harbaugh, 2005). Initially a trial head value is arbitrarily assigned to each cell node. The head values are then altered successively to achieve a closer agreement with the equations. Eventually the equations are satisfied and changes in the head values between iterations become small. The model is considered converged if the maximum

head change between iterations and the mass balance error (i.e. total inflow – total outflow) are both below the specified thresholds.

Traditional MODFLOW (Harbaugh, 2005) is based on a rectangular finite-difference grid, which makes it difficult to fit irregularly shaped boundaries such as rivers. Additionally, refining cell size in areas of interest introduces unnecessary computational burden as the added resolution is carried out to the model edges. Panday et al. (2017) developed an unstructured grid version of MODFLOW, referred to as MODFLOW-USG, which supports a wide range of cell shapes and mitigates the limitations described above. MODFLOW-USG reformulates the partial-differential equation (Equation 2.3) by integrating it over a small control volume V (m^3/d) and then converting it to a surface integral as follows:

$$\int_s (K\nabla h) \cdot n dS_A = S_S V \frac{\partial h}{\partial t} + W_V V \qquad 2.6$$

where S_A is the surface area of the control volume (m^2), n is an outward-pointing unit normal vector on the volume surface and W_v is a source or sink term per unit volume. Equation 2.6 shows that the sum of inflows and outflows across the surface of a control volume is balanced by changes in storage and internal sources and sinks (Panday et al., 2017).

2.2 Groundwater model inversion theory

Groundwater model inversion generally involves minimising an objective function, which describes the mismatch between observations and their simulated equivalents as the sum of weighted squared residuals. The Gauss-Levenberg-Marquardt (GLM) algorithm is commonly used in groundwater model inversion as follows:

$$\delta_\theta = -\left(\left(J^T \Sigma_\varepsilon^{-1} J\right) + (1+\lambda)\Sigma_\theta^{-1}\right)^{-1} \left(\Sigma_\theta^{-1}(\theta - \theta_0) + J^T(d_{sim} - d_{obs})\right) \qquad 2.7$$

where δ_θ is the parameter upgrade vector, J is a sensitivity matrix known as the Jacobian matrix, Σ_ε is the covariance matrix of measurement noise, λ is the Marquardt dampening parameter, Σ_θ is the prior parameter covariance matrix, θ and θ_0 are the current and initial parameter vector respectively, $d_{sim} - d_{obs}$ is the residual factor, and T denotes the transpose of a matrix.

The GLM algorithm is widely implemented in inversion programs such as PEST (Doherty et al., 1994), UCODE (Poeter et al., 2014) and PESTPP (Welter et al., 2015). As shown in Equation 2.7, this algorithm requires a Jacobian matrix that is usually filled using finite-difference

approximations, where each parameter is perturbed separately by a small amount and the resulting changes in the simulated equivalents of observations are recorded in the Jacobian matrix. Although this approach is effective, it requires at least one model run per parameter being estimated, resulting in very long computational time for highly parameterised models.

A different approach, known as the ensemble-smoother, was proposed by Chen and Oliver (2013) and implemented by White (2018) into the PESTPP suite as PESTPP-IES. They reformulated the GLM algorithm to use a Jacobian matrix that is empirically derived from an ensemble of randomly-generated parameter values (White, 2018, Chen and Oliver, 2013):

$$\Delta_\theta = -\left(\left(\mathrm{J}_{\mathrm{emp}}^{\mathrm{T}}\Sigma_\varepsilon^{-1}\mathrm{J}_{\mathrm{emp}}\right) + (1+\lambda)\Sigma_\theta^{-1}\right)^{-1}\left(\Sigma_\theta^{-1}(\Theta - \Theta_0) + \mathrm{J}_{\mathrm{emp}}^{\mathrm{T}}(\mathrm{D}_{\mathrm{sim}} - \mathrm{D}_{\mathrm{obs}})\right) \quad 2.8$$

where

$$\mathrm{J}_{\mathrm{emp}} \approx \Sigma_\varepsilon^{\frac{1}{2}}\Delta_{\mathrm{sim}}\Delta_{\mathrm{par}}^{-1}\Sigma_\theta^{-\frac{1}{2}} \quad 2.9$$

$$\Delta_{\mathrm{sim}} = \frac{\Sigma_\varepsilon^{-\frac{1}{2}}(\mathrm{D}_{\mathrm{sim}} \ominus \overline{\mathrm{D}}_{\mathrm{sim}})}{\sqrt{\mathrm{N_e} - 1}} \quad 2.10$$

$$\Delta_{\mathrm{par}} = \frac{\Sigma_\theta^{-\frac{1}{2}}(\Theta \ominus \overline{\Theta})}{\sqrt{\mathrm{N_e} - 1}} \quad 2.11$$

where Δ_θ is the parameter upgrade matrix, $\mathrm{J}_{\mathrm{emp}}$ is the empirically-derived Jacobian matrix, Θ and Θ_0 are the current and initial parameter vector respectively, $\mathrm{D}_{\mathrm{obs}}$ and $\mathrm{D}_{\mathrm{sim}}$ are the observation and simulated-equivalent ensembles respectively, $\overline{\mathrm{D}}_{\mathrm{sim}}$ and $\overline{\Theta}$ are the mean of the simulated-equivalents to observations and parameters across their respective ensembles respectively, $\mathrm{N_e}$ is the number of realisations, and $\ominus$ denotes broadcast subtraction (broadcasting is an array manipulation technique that handles arrays of different sizes) (White, 2018).

The ensemble-smoother approach has a number of advantages in addition to the computational efficiency described above. Firstly, it produces an ensemble of calibrated models that can be considered to represent the posterior distribution of parameters and predictions, which can be readily used for non-linear uncertainty analysis and allows the prediction results to be presented in a probabilistic manner. Furthermore, it enables the uncertainty in observations to be

expressed as a prior probability distribution, allowing the inversion to fit to the observation distribution instead of the observation itself. This is important for geophysically-derived observations that often contain a considerable degree of uncertainty.

2.3 Nuclear Magnetic Resonance theory

In the context of hydrogeophysics, NMR uses properties of the hydrogen nuclei in subsurface water to directly estimate the quantity of subsurface water, along with other aquifer-related properties such as hydraulic conductivity. NMR measures changes in the magnetic field produced by the magnetic moments of precessing hydrogen protons (Behroozmand et al., 2015, Coates et al., 1999). When the magnetic moments of these hydrogen nuclei are placed within a static magnetic field B_0, they align with the static field. Once in equilibrium, the NMR instrument is used to emit an energising pulse oscillating at the Larmor frequency f_L (Hz) to flip the magnetic moments out of equilibrium. The Larmor frequency is defined by:

$$f_L = \frac{-\gamma|B_0|}{2\pi} \qquad 2.12$$

where γ is the gyromagnetic ratio that describes the strength of nuclear magnetism and has a constant value of 0.2675 x 10^9 Hz T^{-1} for hydrogen. The Larmor frequency is directly proportional to the strength of static magnetic field (Equation 2.12). For surface NMR, the static field is the Earth's magnetic field, while for borehole NMR the static field is generated by magnets mounted in the instrument.

The energising pulse emitted by the NMR instrument tips the hydrogen nuclei away from equilibrium, the angle to which is referred to as the tip angle and is proportional to the intensity and duration of the pulse (the ideal tip angle is perpendicular to the background magnetic field vector). Then the pulse is turned off, causing the hydrogen nuclei to relax back to equilibrium, during which they emit a measurable magnetic signal.

The key NMR parameters that are important for hydrogeological studies are the initial signal amplitude E_0 (V) and the decay time constant: T_2^* (s) for surface NMR or T_2 (s) for borehole NMR. For surface NMR, the Free Induction Decay (FID) pulse sequence is commonly used, which applies a single pulse with a tip angle of 90° (Walsh, 2008). The decay pattern of the measured signal is described as follows:

$$V(t) = E_0 e^{-\frac{t}{T_2^*}} \qquad 2.13$$

where V(t) is the signal amplitude (V) measured at time t (d). The initial signal amplitude is directly proportional to the water content and is therefore a proxy for porosity in the saturated zone. The initial time is defined as when relaxation first occurs, which in most instruments is often during the pulse. As signal cannot be measured during the pulse, the estimation of initial signal amplitude requires extrapolating the measured signal back to the start of signal decay.

The decay time constant T_2^* is related to pore size and can be used to estimate hydraulic conductivity via various petrophysical relationships (Maurer and Knight, 2016). However, T_2^* is susceptible to magnetic heterogeneity, which can be caused by regional-scale magnetic field gradients and the magnetic susceptibility contrast between porous material components (Knight et al., 2012). Therefore, T_2^* as a direct estimator of saturated porosity is generally more useful in areas where the subsurface materials are mostly weakly magnetic and generally without materials with high magnetic susceptibility, such as magnetite.

In comparison, the decay time constant T_2 is less susceptible to magnetic heterogeneity. This constant is commonly estimated using borehole NMR with the Carr-Purcell-Meiboom-Gill (CPMG) pulse sequence (Carr and Purcell, 1954, Meiboom and Gill, 1958), which consists of a 90° pulse followed by a train of 180° pulses to refocus the dephased spins, between which a signal referred to as echo is measured. The exponential decay of T_2 (V_d) formed from the echo peaks is described as follows:

$$V_d = E_0 e^{-\frac{\tau_e}{T_2}} \qquad 2.14$$

where τ_e is the time between the beginning of a refocusing pulse and the resulting echo peak (s). Compared to T_2^* from surface NMR, T_2 from borehole NMR has a well-established relationship with hydraulic conductivity (Knight et al., 2012) but is relatively difficult to measure at the surface, so its use is often restricted to borehole surveys.

2.4 Time-domain electromagnetics theory

TEM is an electromagnetic method that estimates subsurface electrical resistivity. A brief overview of TEM theory is provided below; more details can be found in Telford et al. (1990) and Everett (2013).

As with all electromagnetic methods, TEM is physically governed by the Maxwell's equations:

Gauss's Law $$\nabla \cdot \mathrm{E} = \frac{\rho}{\epsilon_0}$$ 2.15

Gauss's Magnetism Law $$\nabla \cdot \mathrm{B} = 0$$ 2.16

Faraday's Law $$\nabla \times \mathrm{E} = -\frac{\mathrm{dB}}{\mathrm{dt}}$$ 2.17

Ampère's Law $$\nabla \times \mathrm{B} = \mu_0 \left(\mathrm{J} + \epsilon_0 \frac{\partial \mathrm{E}}{\partial \mathrm{t}} \right)$$ 2.18

where E is the electric field (Vm^{-1}), B is the magnetic field (T), ρ is electric charge density (Cm^{-3}), J is electric current density (Am^{-2}), ϵ_0 is the permittivity of free space (Fm^{-1}), μ_0 is the permeability of free space (Hm^{-1}), and t is time (s). Gauss's Law (Equation 2.15) shows that electric field diverges from positive charge and converges to negative charge. Gauss's Magnetism Law (Equation 2.16) describes the conservation of magnetic flux, which states that the total magnetic flux through a closed surface must be zero and the magnetic field lines must be closed loops. Faraday's Law (Equation 2.17) indicates that a time-varying magnetic field produces a circulating electric field, while Ampere's Law (Equation 2.18) shows that an electric current and a time-varying electric field produce a circulating magnetic field.

There are two broad types of electromagnetic methods: frequency-domain and time-domain (Everett, 2013). Frequency-domain electromagnetics involves emitting a transmitter current that varies sinusoidally with time at a constant frequency. For TEM, a transmitter current is applied and then turned off abruptly as a square wave. This induces currents in the ground that can be pictured travelling into the earth as an expanding smoke ring. These eddy currents produce a secondary magnetic field, the decay of which induces a measurable voltage in the receiver loop that is usually placed at the centre of the transmitter loop.

The induced voltage is measured over a series of time windows, each sampling sequentially to measure the signal at successive times. The signal is strong at the beginning and hence the early time windows are relatively narrow. As the signal decays over time, the late time windows are wider to improve the signal-to-noise ratio. The ground signal eventually disappears into the system noise; this relates directly to the maximum depth of investigation.

2.5 Petrophysical relationships

Geophysical data can be related to hydrogeological properties such as porosity and hydraulic conductivity via petrophysical relationships (Slater, 2007). One commonly used petrophysical relationship is Archie's Law, which relates bulk EC to fluid EC and porosity (Archie, 1942, Winsauer et al., 1952):

$$\sigma_{\mathrm{bulk}} = a\sigma_{\mathrm{fluid}}\phi^{\mathrm{m}} \qquad 2.19$$

where σ is EC (S m^{-1}), ϕ is porosity, a and m are commonly referred to as the tortuosity constant and cementation index, respectively. The tortuosity constant commonly ranges between 0.004 and 17.7 for sandstones (i.e. four orders of magnitude) and between 0.33 and 78 for carbonates (i.e. two orders of magnitude) (Glover, 2016, Rivero, 1977). The cementation index describes the connectivity between pores and commonly varies over a much smaller range between 1.5 and 2.5 for most porous arenaceous sediments (Glover et al., 1997) and between 2.5 and 5 for carbonates, which generally have a lower pore connectivity (Tiab and Donaldson, 2015). Archie's Law is only valid for areas where fluid is the main contributor to electric current flow and therefore not applicable to sediments that contain a significant amount of clay.

Hydraulic conductivity is the key hydraulic parameter in most hydrogeological and groundwater modelling studies and can be related to EC using a log-log linear relationship as follows (Purvance and Andricevic, 2000):

$$\mathrm{K} = \alpha\sigma^{\beta} \qquad 2.20$$

where K is hydraulic conductivity (m/d), σ is bulk EC (S m^{-1}), and α and β are empirical constants. The constant β is positive for resistive materials such as sand where a higher σ indicates a higher interconnected pore volume and hence a higher K. Meanwhile, the constant β is negative for conductive materials such as clay where a higher σ indicates a higher clay and silt content and hence a lower K. There is little literature that describes the range of values for β, with most on the order of 0.52 to 0.93 for resistive materials (Frohlich et al., 1996, Heigold et al., 1979, Purvance and Andricevic, 2000) and -5.36 to -0.063 for conductive materials (Kosinski and Kelly, 1981, Ponzini et al., 1984, Purvance and Andricevic, 2000). Meanwhile, the constant α is not even this well defined in the literature, as it seems to be heavily dependent on site conditions (Purvance and Andricevic, 2000, Slater, 2007). This relationship (Equation 2.20) was applied by

Christensen et al. (2017) to convert airborne-EM data to a hydraulic conductivity distribution that was used to evaluate the prediction accuracy of a groundwater model.

There are also petrophysical relationships that relate hydraulic conductivity to the NMR parameters. These include the Schlumberger-Doll Research equation (Kenyon et al., 1988) and the Sum-of-Echoes equation (Allen et al., 2000):

Schlumberger-Doll Research $$K = c\phi^{m}{T_{2ML}}^{n} \quad (2.21)$$

Sum-of-Echoes $$K = c_{SOE}SOE^{d} \quad (2.22)$$

where K is hydraulic conductivity (m/s), ϕ is porosity (dimensionless), T_{2ML} is the geometric mean of the T_2 distribution (s), SOE is the sum of signal amplitudes of the FID decay (V), and c, m, n, c_{SOE} and d are empirical constants, which are often calibrated against field data to account for local conditions (Behroozmand et al., 2015). Knight et al. (2016) report that the optimal values are m = 1, n = 2 and c between 0.05 and 0.12 ms^{-3} for unconsolidated aquifers. Compared to the commonly used SDR equation, the sum-of-echoes equation has the advantages of a higher signal-to-noise ratio and it does not require the full T_2 distribution to be inverted for each decay curve (Maurer and Knight, 2016).

3 Investigating the impact of artificial environmental watering on a semi-arid, highly saline floodplain using electromagnetics and surface nuclear magnetic resonance

Chris Li[a, b]

Rebecca Doble[a]

Michael Hatch[b]

Graham Heinson[b]

[a] CSIRO Land and Water, Glen Osmond, South Australia, Australia

[b] The University of Adelaide, Adelaide, South Australia, Australia

Published in *Hydrological Processes*

https://doi.org/10.1002/hyp.13732

Statement of Authorship

Title of Paper	Investigating the impact of artificial environmental watering on a semi-arid, highly saline floodplain using electromagnetics and surface nuclear magnetic resonance
Publication Status	Published
Publication Details	Published in the journal *Hydrological Processes* vol. 34 issue 11 pp. 2337-2350

Principal Author

Name of Principal Author (Candidate)	Ho Yin Li (Chris)		
Contribution to the Paper	Conception and design Collection, analysis and interpretation of data Writing the manuscript		
Overall percentage (%)	90		
Certification:	This paper reports on original research I conducted during the period of my Higher Degree by Research candidature and is not subject to any obligations or contractual agreements with a third party that would constrain its inclusion in this thesis. I am the primary author of this paper.		
Signature		Date	20 August 2020

Co-Author Contributions

By signing the Statement of Authorship, each author certifies that:

i. the candidate's stated contribution to the publication is accurate (as detailed above);

ii. permission is granted for the candidate in include the publication in the thesis; and

iii. the sum of all co-author contributions is equal to 100% less the candidate's stated contribution.

Name of Co-Author	Rebecca Doble		
Contribution to the Paper	Conception and design Critically revising the manuscript		
Signature		Date	20 August 2020

Name of Co-Author	Michael Hatch		
Contribution to the Paper	Conception and design Collection and analysis of data Critically revising the manuscript		
Signature		Date	20 August 2020

Name of Co-Author	Graham Heinson		
Contribution to the Paper	Conception and design Critically revising the manuscript		
Signature		Date	20 August 2020

Abstract

Floodplains have ecological and cultural significance and need to be managed properly. However, floodplains along the River Murray in South Australia are showing a substantial vegetation health decline due to increased salinization. To improve floodplain health, water resource managers are experimenting with the delivery of fresh water to the high priority floodplains. However, the salinity impact of watering on the shallow, saline groundwater is not well understood due to the presence of a spatially variable and impermeable surface clay layer. This study uses time-domain electromagnetics (EM) and surface Nuclear Magnetic Resonance (NMR) to assess the impact of watering on groundwater salinity in a South Australian River Murray floodplain. We examined the changes in bulk electrical conductivity (EC) from time-domain EM data collected at five sites before and after a watering event. Only one site showed a bulk EC reduction of up to 5,200 µS/cm, suggesting groundwater was freshened, while the remaining sites showed little change in bulk EC. Our results suggest the salinity impact of watering is highly localised and heterogeneous. For ecological management purposes, it is also desirable to estimate groundwater EC after watering. This study presents a method to estimate groundwater EC in a highly conductive environment by coupling EM with surface NMR. We also extended the analysis to an airborne-EM survey to derive spatial distribution of groundwater EC, which provides additional insights into the floodplain processes and shows an overall good agreement with field observations. This study demonstrates the potential benefits of using geophysics to investigate floodplain dynamics. The methodology developed in this study is useful for first-pass assessments of groundwater quality in a non-invasive manner, which is transferrable to many other fresh or saline groundwater systems, especially in ecologically sensitive areas where traditional hydrogeological techniques may be unsuitable due to the potential disturbance of local ecosystems.

3.1 Introduction

Floodplains have ecological and cultural significance and need to be managed properly (Tockner and Stanford, 2002). For floodplains with shallow groundwater, a sound understanding of hydrogeology is essential for environmental management. Floodplain hydrogeology is usually informed by traditional, borehole-based hydrogeological techniques such as drilling, aquifer tests and groundwater sampling (e.g. Postma et al., 2007, Chakka and Munster, 1997). However, the effectiveness of these techniques in characterising the subsurface depends on the number and distribution of boreholes (Slater, 2007). The use of these invasive techniques may be prohibited in floodplains that are protected due to their ecological and/or cultural significance, where disturbance to the system must be kept to a minimum. Therefore, there is a need for methods that can maximise the value of the limited borehole data in these floodplains to characterise the subsurface.

Geophysical techniques provide information about the subsurface and have several advantages compared to the traditional hydrogeological techniques: (i) geophysical techniques are non-invasive, (ii) they tend to have larger spatial coverage (especially via airborne techniques) and (iii) they cost less on an areal basis (Slater, 2007). Time-domain Electromagnetics (EM) is a geophysical technique that is commonly used in hydrogeology to estimate subsurface bulk electrical conductivity (EC), which is then used to infer information about soil saturation, lithology and groundwater salinity (Everett, 2013). For example, time-domain EM has been used to study salt water transport in the Okavango Delta (Bauer-Gottwein et al., 2010) and characterise surface water-groundwater interactions in the Australian River Murray floodplains (Hatch et al., 2010). However, the interpretation of time-domain EM is ambiguous in environments with saline groundwater and clay, where a conductive response may reflect the existence of saline groundwater in a sand unit or a moist clay (Everett, 2013). This interpretation ambiguity may be reduced by coupling time-domain EM with surface nuclear magnetic resonance (NMR) (Legchenko et al., 2009).

Surface NMR is a geophysical technique that exploits the nuclear properties of subsurface water hydrogen protons to gain hydrogeological information. The initial signal amplitude is related to water content, which is a proxy for porosity in the saturated zone, and a relaxation time constant T_2* can be estimated from the signal envelope to inform the pore size (Legchenko et al., 2002). The use of surface NMR to estimate permeability has been demonstrated in a number of studies, such as Gunther and Muller-Petke (2012) and Vilhelmsen et al. (2016). This is achieved by applying permeability models, such as the Schlumberger-Doll-Research equation (Kenyon et al.,

1988) and the Sum-of-Echoes equation (Allen et al., 2000), to relate NMR parameters to permeability. Compared to time-domain EM, surface NMR has a considerably longer measurement time and hence the data sets that are collected are generally not as spatially exhaustive. Nevertheless, by coupling EM data with surface NMR data, the interpretation ambiguity in time-domain EM results may be reduced (Legchenko et al., 2009), which can aid the study of hydrogeology and processes in floodplains with clay and shallow, saline groundwater, such as the South Australian River Murray floodplains.

The River Murray is an extensive river in Australia that spans 2,500 km across South Australia, Victoria and New South Wales; much of the river system is lined by extensive floodplains with exceptional ecological and cultural values (Mooney and Tan, 2012, Kingsford, 2000). These floodplains are home to many iconic native species, including River Red Gum (Eucalyptus Camaldulensis) and Black Box (Eucalyptus Largiflorens) (George et al., 2005). Additionally, many of these floodplains are listed as Ramsar sites, which are wetlands designated as being of international importance (Ramsar Convention Bureau, 1971).

In South Australia, the River Murray floodplains are showing a substantial decline in tree health due to increased salinization (Jolly et al., 1993). Weirs that were built along the river in the 1920s for flow regulation and provision of steady water supply for irrigation hold river water at artificially high levels (Maheshwari et al., 1995), thereby act to increase the floodplain groundwater level (Jolly et al., 1993). Additionally, irrigation on the highlands adjacent to the floodplains increases groundwater discharge to the floodplains, further raising the floodplain groundwater level (Jolly et al., 1993, Doble et al., 2006). The floodplain groundwater is naturally saline and has a fluid EC of 2,000 – 80,000 µS/cm with a mean of 37,000 µS/cm (a total dissolved solids of approximately 25,000 mg/L) (Herczeg et al., 2001). When the saline groundwater rises close to the surface, salt deposition in the overlying soil increases due to capillary rise and evaporation (Jolly et al., 1993). Meanwhile, the weirs and increasing river extraction for irrigation have substantially reduced flood frequency and size (Jolly et al., 1993, Maheshwari et al., 1995), which would naturally dilute salt concentrations in the soil (Crosbie et al., 2009, Evans and Kellett, 1989). These conditions have resulted in very high levels of soil salinity, damaging floodplain tree health.

To improve the floodplain condition, water resource managers are experimenting with artificial delivery of low salinity water to the floodplains via channels and wetlands, referred to as environmental watering, to reduce soil salinity and improve soil water availability (Docker and Robinson, 2014, Garrick et al., 2012). However, the impact of watering on groundwater salinity

is not well understood as the floodplains are overlain by a clay layer, which is highly impermeable but can be absent in places and/or contain preferential flow features.

This artificial environmental watering is hypothesised to considerably freshen at least the top portion of the floodplain groundwater. We test this hypothesis by examining the changes in bulk EC before and after a watering event using time-domain EM. For ecological management purposes, it is also desirable to estimate groundwater EC after the watering event. This study presents a method to estimate groundwater EC in a highly conductive floodplain environment by coupling EM data with coincident surface NMR data through a modified version of Archie's Law. We also extended the salinity analysis to an airborne-EM survey to derive spatial distribution of groundwater EC at various depths, providing additional insights into the floodplain processes.

3.2 Methods

3.2.1 Site descriptions

The study area is in the Calperum floodplain of the South Australian River Murray region (Figure 3.1). It has a semi-arid climate with a mean annual rainfall of 263 mm/a and potential evaporation of 1935 mm/a (Bureau of Meteorology, 2018). The hydrogeological conceptualisation of a typical South Australian River Murray floodplain is illustrated in Figure 3.2 (Holland et al., 2009). Conceptually, the floodplain receives saline groundwater from the highland and delivers it to the river, with salt being accumulated in the overlying floodplain soil through evapotranspiration. The key hydrogeological formations are the Coonambidgal Clay Formation and the Monoman Sands Formation (Evans and Kellett, 1989, Holland et al., 2009). The Coonambidgal Formation comprises fluvial clays and silts that were deposited during episodic flooding (Evans and Kellett, 1989). This mostly impermeable layer occurs across the floodplain surface but can be absent in places, and is 1 to 7 m thick in the study area (Amerasinghe et al., 2011). The underlying unit is the Monoman Formation, which comprises a mixture of channel and sheet sand deposits with occasional presence of intervening silty clay sequences (Evans and Kellett, 1989). It is a semi-confined aquifer and can be up to 32 m thick in the study area (Amerasinghe et al., 2011). The Monoman Formation is underlain by an effective regional aquitard limiting vertical influx of deeper groundwater into the floodplain aquifer system (Evans and Kellett, 1989).

In the study area, the water table generally resides in the Coonambidgal Formation and can be as shallow as 1 m depth near drainage and lake features (Amerasinghe et al., 2011). The water table may also be found in the Monoman Formation, at up to about 10 m depth in areas of relatively high elevation and distant from surface waterbodies (Amerasinghe et al., 2011). Groundwater flows towards the River Murray, which is the regional sink (Evans and Kellett, 1989). Groundwater salinity is high with a mean fluid EC of approximately 23,000 µS/cm in the study area (Amerasinghe et al., 2011).

Artificial environmental watering was trialled at three sites in the study area between 2015 and 2018, including Clover Lake, Woolpolool Swamp and Merreti East (Figure 3.1 and Table 3.1). Clover Lake and Woolpolool Swamp each received ~2,000,000 m^3 of freshwater over the period between November 2017 and March 2018. Merreti East has been receiving freshwater annually since 2015, with a relatively small volume of 100,000 m^3 over the time period pertinent to this survey. It was filled in November 2017 and dried out between December 2017 and January 2018.

Assuming a total watering area of 2 km², an evaporation of 1226 mm during the watering period (Bureau of Meteorology, 2018), and an average porosity of 20%, a simple water balance model suggests the total watering volume of 4,100,000 m³ may influence at most the top 5 m of the floodplain groundwater. This is based on the assumption that the fresh water has relatively lower density and will float on top of the saline groundwater (Werner and Laattoe, 2016).

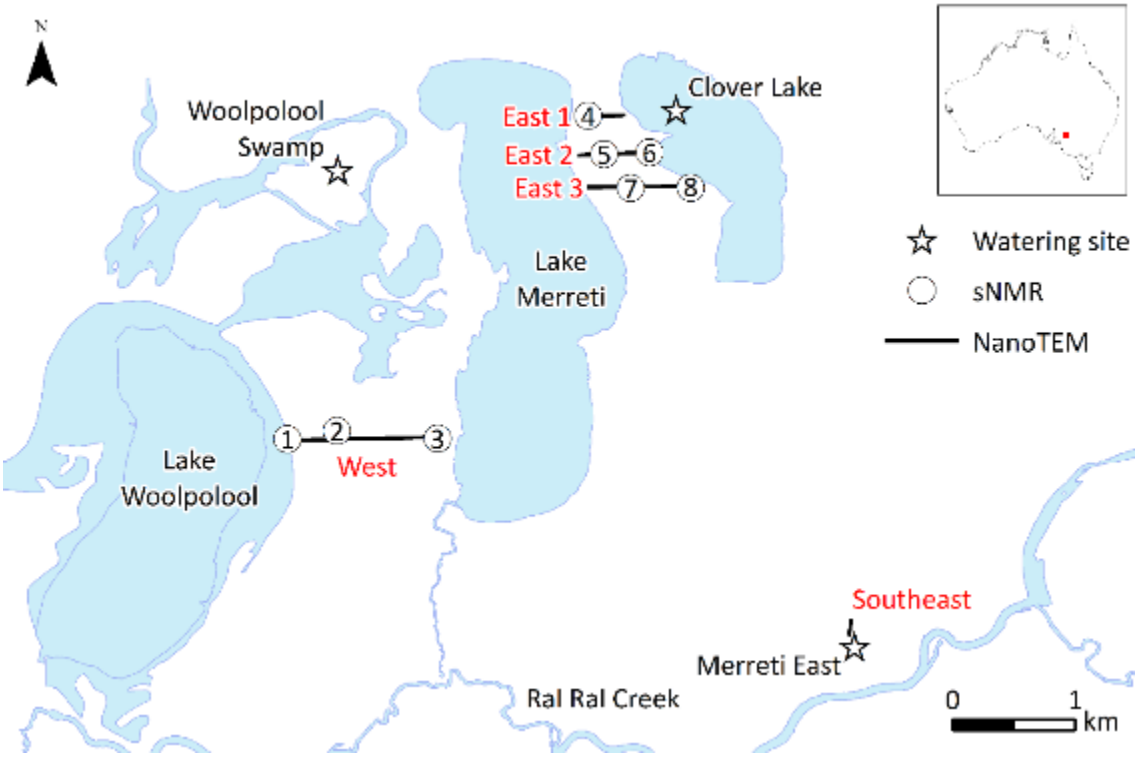

Figure 3.1 Site map showing the locations of geophysical soundings, surface water features and watering sites in the study area of Calperum floodplain in South Australia. The number within the surface NMR (sNMR) symbols represents the site number. The River Murray is located to the south of Ral Ral Creek.

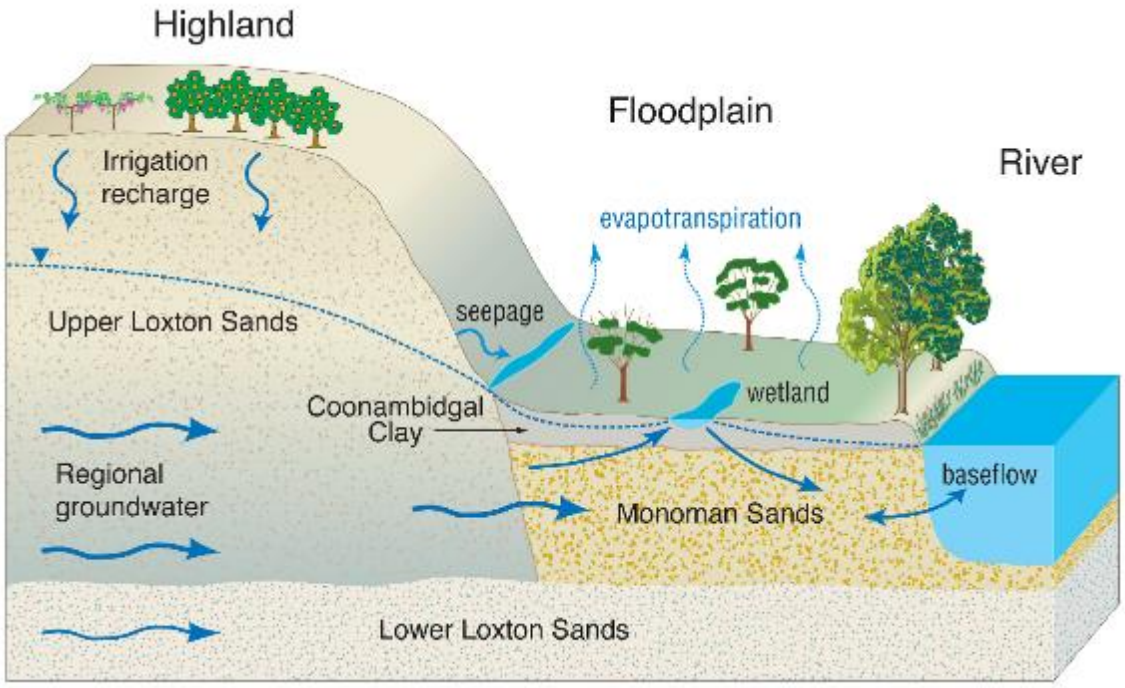

Figure 3.2 Cross-section diagram showing the key hydrogeological formations and conceptualisation of a typical South Australian River Murray floodplain (Holland et al., 2009).

Table 3.1 Details of environmental watering at Calperum

Site	Time	Volume (m^3)
Clover Lake	November 2017 - March 2018	2,000,000
Woolpolool Swamp	November 2017 - March 2018	2,000,000
Merreti East	Annually since 2015	100,000

3.2.2 Land-based surveys

Two land-based geophysical surveys were undertaken over the field area. The first ran from 18 to 22 September 2017; while the second ran from 5 to 16 March 2018. These were timed to measure the ground conditions along a number of transects before and after the November to March Clover Lake/Woolpolool Swamp watering event. Time-domain EM and surface NMR data were collected during the surveys; station locations are shown in Figure 3.1. The time-domain EM Transects East 1 to 3 were set up to estimate the watering impact from Clover Lake, while Transect Southeast was set up for the Merreti East watering site. Transect West is distant from the watering sites and serves as a control. Transects East 1 and 3 are additional sites introduced in the 2018 survey to better capture the watering impact from Clover Lake and were not surveyed in 2017. Subsurface porosity has been estimated at most transects with at least one

surface NMR sounding, except for Transect Southeast where no surface NMR data were collected.

3.2.2.1 Time-domain EM

Time-domain EM data are collected using a transmitter loop and a receiver loop, often laid on the ground surface. A direct current is passed through the transmitter loop and then turned off abruptly. The rapid turn-off produces a time-varying magnetic field. As the magnetic field passes through the subsurface, eddy currents are generated in subsurface conductors. The flow of eddy currents creates a decaying secondary magnetic field that is measured by the receiver loop. The decay rate of the secondary magnetic field (relative to the turnoff time) is related to the bulk EC of the ground. The decay curves are inverted to depth and electrical resistivity to describe the electrical structure of the Earth under a given sounding. For a more comprehensive description the readers are referred to Parasnis (2012) and Telford et al. (1990).

In this study, time-domain EM data were collected using Zonge Engineering's NanoTEM system. This system is fast sampling, and the transmitter has a fast turn-off time (about 1.5 µS), making it suitable for near-surface applications. Data were collected using a central loop configuration, where a 5 m x 5 m receiver loop was placed at the centre of a 20 m x 20 m transmitter loop, both of which were single turn. The transmitter was set to 2 amps and powered by a 12 V battery. Data were acquired at a frequency of 32 Hz and a sampling period of 1.6 µS. The stations had a nominal spacing of 20 m (i.e. adjacent to each other) and three data stacks were collected at each station. The measurements were processed to remove noisy late time data.

We performed 1-D inversion on the time-domain EM data using AarhusInv (Auken et al., 2015). Data were inverted as smooth-models using 20 layers, where the inverse problem was regularised using a vertical constraint of 0.3. The inversion outputs were used to define the conductive Earth profiles for the surface NMR inversion.

3.2.2.2 Surface NMR

Hydrogen protons in subsurface water produce a bulk magnetization vector that align with the Earth's magnetic field orientation. This bulk magnetization vector can be tipped away from the Earth's magnetic field by applying an external magnetic pulse oscillating at the Larmor frequency (f_0) given by:

$$f_0 = B_0 \gamma \qquad 3.1$$

where B_0 is the Earth's magnetic field and γ is the gyromagnetic ratio, which has a constant value of 42.58 MHz/Tesla for hydrogen (Coates et al., 1999).

The Free Induction Decay (FID) is the most commonly used pulse sequence in a surface NMR survey (Behroozmand et al., 2015). It involves applying an alternating current at the Larmor frequency to a coil loop laid on the ground surface to create a magnetic pulse (which is different from time-domain EM where the pulse is generated after the current is switched off). The pulse propagates downward through the Earth, tipping the net magnetisation of subsurface water hydrogen protons into a plane at right angles to the Earth's magnetic field. The pulse is then switched off and the nuclei relax back to their previous alignment with the Earth's magnetic field. During this relaxation process, a time-varying secondary magnetic field oscillating at the Larmor frequency is created, inducing a voltage in the surface loop that is measured by the surface NMR instrument. The decay envelope of the voltage forms the FID signal and is a function of the effective transverse relaxation time constant (T_2*) and initial amplitude (E_0) given by:

$$V(t) = E_0 \, e^{\frac{-t}{T_2^*}} \qquad 3.2$$

where V(t) is the voltage measured at time t.

The subsurface water content is directly proportional to the initial amplitude E_0 (Knight et al., 2012) and is a proxy for porosity in the saturated zone where all pores are completely filled with water. As the surface loop is used as both a transmitter and receiver, the FID signal is only measured after the pulse duration time and instrumental dead-time (the time delay between applying an excitation field and the start of data recording). Therefore, the estimation of E_0 requires extrapolating the signal back to the initial time when the received signal would be at its maximum.

The effective transverse relaxation time constant T_2* is related to pore size but is also sensitive to magnetic field heterogeneities. These heterogeneities may be caused by large-scale Earth's magnetic field variations and/or small scale magnetic susceptibility differences between pore water and solid material (Behroozmand et al., 2015). Three relaxation processes are included in T_2*:

$$\frac{1}{T_2^*} = \frac{1}{T_{2B}} + \frac{1}{T_{2S}} + \frac{1}{T_{2IH}} \qquad 3.3$$

where T_{2B} is the transverse relaxation time of bulk fluid, T_{2S} is the transverse relaxation time of solid matrix surface, and T_{2IH} is the dephasing relaxation time that accounts for relaxation in a heterogeneous magnetic field (Behroozmand et al., 2015).

In contrast, the transverse relaxation time constant T_2 is different from T_2* in that it is less susceptible to magnetic field heterogeneities and contains only the T_{2B}^{-1} and T_{2S}^{-1} terms in Equation 3.3 (Knight et al., 2012). The constant T_2 is commonly estimated using borehole NMR with the Carr-Purcell-Meiboom-Gill (CPMG) pulse sequence (Carr and Purcell, 1954, Meiboom and Gill, 1958) and has a well-established link to hydraulic conductivity (Knight et al., 2012).

If the term T_{2IH}^{-1} in Equation 3.3 is small, then T_2* is similar to T_2. Information about T_{2IH} is commonly inferred from site mineralogy and/or by using borehole NMR so that T_2 and T_2* can be compared. However, the bores in our study area are too shallow to provide useful borehole NMR information. Available bore logs (Amerasinghe et al., 2011) and examination of airborne-EM data sets (Fitzpatrick and Munday, 2009) suggest that there is little or no material with high magnetic susceptibility. Therefore, we have assumed that our study area is weakly magnetic, the T_{2IH}^{-1} term is small, and T_2* is similar to T_2. This approach has been used in other studies, such as Gunther and Muller-Petke (2012) and Vilhelmsen et al. (2016). This assumption allows us to estimate hydraulic conductivity through equations such as the Sum-of-Echoes equation (Allen et al., 2000). More details about surface NMR are comprehensively discussed in Behroozmand et al. (2015).

In this study, surface NMR data were collected using Vista Clara's GMR system. The instrument has a relatively short dead-time of approximately 4 ms (Walsh et al., 2011) to enable detection of water in very small pores. The control station consisted of a 540 V DC/DC converter, a 4,000 V transmitter and a 16 µF tuning unit. A 70 m x 70 m square loop with a single turn was used; cancellation loops were not needed as noise levels were very low in the study area. The Earth's magnetic field was measured using a magnetometer and all eight surface NMR sites showed a similar value of 58,600 nT, equating to a Larmor frequency of 2,495 Hz (Equation 3.1). A pulse duration time of 40 ms was used at all sites; another pulse duration time of 20 ms was tested at Site 6 to evaluate the impact of pulse duration time on the NMR-derived hydraulic conductivity. Depending on local conditions, 8 to 16 stacks of readings were recorded and each stack contained 24 to 36 pulse moments, which ranged between 0.1 and 15 As.

The field data were pre-processed using Vista Clara's QC software. The bandwidth filter was set to 300 Hz. As the data were essentially noise-free, each decay was truncated at 1,000 ms, and neither spike removal nor harmonic subtraction was applied. All data stacks were visually

inspected on a spectral display and rejected if excessive noise was found; most rejection was attributed to the electromagnetic noise from the occasional vehicular traffic in the area.

The data were inverted using the 1D, multi-exponential inversion algorithm from Walsh (2008). The magnetic field incident angle was estimated to be -66° based on the world magnetic model developed by Chulliat et al. (2015). The declination angle with respect to the coil geometry was set to 0° as the coil loop was aligned with magnetic north. The regularization factor is a trade-off between spatial resolution and noise stability and was set to 0.01, which is the value recommended by Vista Clara (2015). The inversion's maximum depth parameter was set to 120 m, slightly deeper than 1.5 times the coil side length as recommended by Vista Clara (2015). As the ground conditions were saline, inversion results were improved by using the land-based time-domain EM results to define the conductive Earth profile.

As part of the inversion process, hydraulic conductivities were estimated using the Sum-of-Echoes equation, which relates the sum of signal amplitudes in the FID decay (assuming T_2* is similar to T_2) to hydraulic conductivity (Allen et al., 2000, Maurer and Knight, 2016) given by:

$$\mathrm{K} = \mathrm{c}\ \mathrm{SOE}^{\mathrm{d}} \qquad 3.4$$

where K is hydraulic conductivity, SOE is the sum of signal amplitudes in the FID decay, and c and d are empirical constants. As there are currently no field measurements of hydraulic conductivity available in the study area to calibrate the empirical constants c and d, the inversion's default value of 2 is used for d (Maurer and Knight, 2016) and 4200 for c (Vista Clara, 2015). To enable comparison between sites, the hydraulic conductivity estimates were normalised to the global maximum value across all soundings (i.e. the highest hydraulic conductivity value at Site 6).

3.2.3 Airborne electromagnetics

Airborne-EM involves carrying an EM system using an aircraft and provides subsurface bulk EC distribution at a large scale. The study area is covered by an airborne-EM survey undertaken by Fugro Airborne Surveys using the helicopter EM system RESOLVE during July and August 2008, which was reported by Fitzpatrick and Munday (2009).

The RESOLVE system is a helicopter frequency-domain EM system, which is different from time-domain EM in that it emits a sinusoidally varying current at specific frequencies, with each frequency providing conductivity information at different depths. The RESOLVE system collects

data at six frequencies, ranging from approximately 380 Hz to 131,000 Hz, thereby collecting data at a range of depths. Five of the six transmitter-receiver antenna pairs are oriented using a horizontal coplanar geometry; one pair is oriented as a vertical-coaxial pair. With a helicopter travel speed of approximately 120 km/h and a sampling rate of 0.1 s during the survey, data were acquired every 3 – 5 m along the flight lines; the flight lines had a nominal separation of 200 m. In parts of the survey area that are particularly conductive, the depth of investigation was estimated to be ~20 m (Fitzpatrick and Munday, 2009).

The collected data were calibrated, processed and inverted simultaneously (Brodie and Sambridge, 2006) as smooth models consisting of 18 layers with an initial conductivity of 100 mS/m and layer thicknesses ranging between 2 and 9.18 m. The resulting bulk EC distributions were used by Amerasinghe et al. (2011) to map the water table, flush-zones, groundwater salinity and recharge zones over the Calperum Floodplain.

3.2.4 Groundwater electrical conductivity (EC) workflow

In this paper, we present a method to estimate groundwater EC in a highly conductive environment by coupling EM with surface NMR data sets (Figure 3.3). This method is based on a modified version of Archie's Law (Archie, 1942, Winsauer et al., 1952), which relates bulk EC (σ_{bulk}) to pore water EC (σ_{water}) given by:

$$\sigma_{\mathrm{water}} = \alpha\, \sigma_{\mathrm{bulk}}\, \phi^{-\mathrm{m}} \qquad 3.5$$

where α is the tortuosity constant that describes the diffusion process in a porous media, ϕ is porosity and m is the cementation index that describes the pore connectedness (Glover, 2009). As the Monoman aquifer is dominated by sands, the cementation index m is set to 1.3, which is a typical value for sand (Archie, 1942).

Archie's Law assumes that the bulk electrical current flow is mainly contributed by pore water, while the contribution from the particle matrix surface is minor. This is not valid for clayey sediments where the particle matrix surface is conductive and contributes considerably to current flow (Glover et al., 2000). Over much of the South Australian Murray Basin, the Monoman Sands aquifer is known to be predominately made up of sands and may occasionally contain some intervening sequences of silty clay. In the study area, the drill logs show that the amount of silty clay is small (Amerasinghe et al., 2011). Additionally, the groundwater salinity is so high that it is likely to dominate the contribution to current flow despite the occasional presence of silty clay.

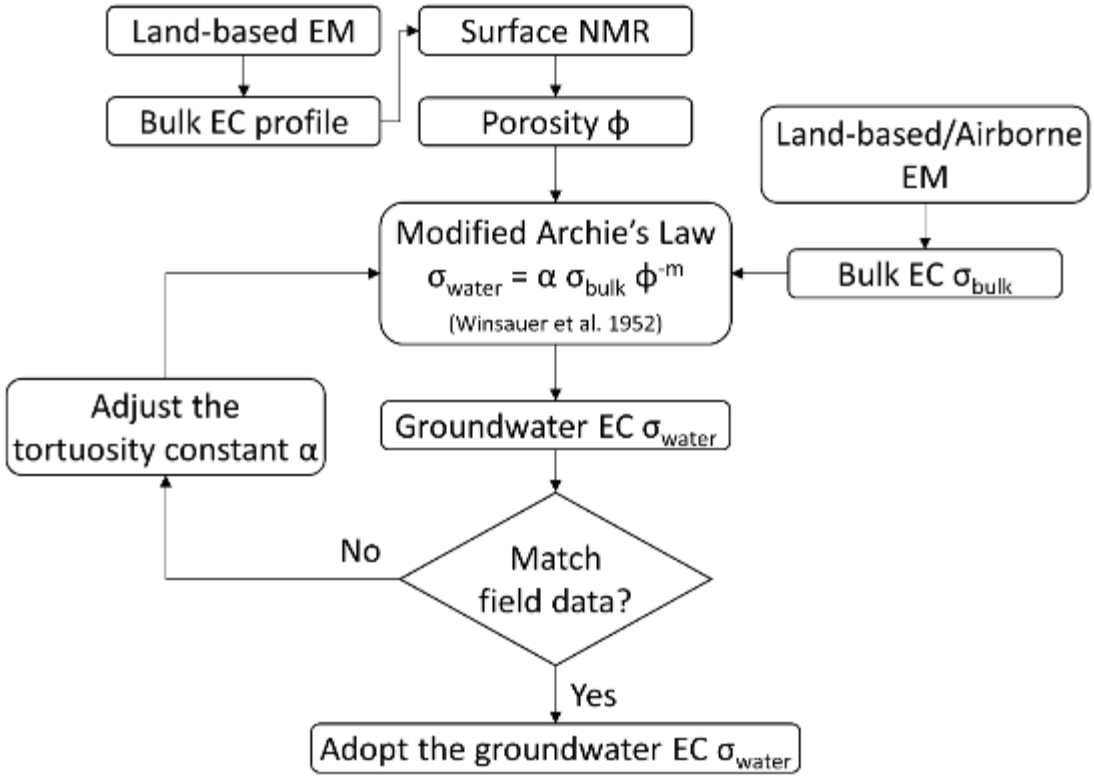

Figure 3.3 A workflow schematic for estimating groundwater EC in a highly conductive environment by coupling EM with surface NMR data sets. This method is only applicable in areas where pore water is the dominanting component contributing to current flow. While both land-based and airborne EM can be used as input for the modified Archie's Law, we recommend using the land-based EM for the surface NMR inversion due to their similarity in scale.

Porosity information (ϕ in Equation 3.5) is provided by the surface NMR water content data, as water content is a proxy for porosity in the saturated zone where all pores are completely filled with water. Surface NMR data were interpolated linearly for transects with multiple surface NMR soundings, and applied uniformly for Transect East 1 where only a single surface NMR sounding was available. Bulk EC information (σ_{bulk} in Equation 3.5) is provided by the time-domain EM data, which were also used to define the conductive Earth profile for the surface NMR inversion. This workflow converts bulk EC cross-sections to cross-sections of groundwater EC estimates.

We extended the analysis to the airborne-EM data to develop spatial distribution of groundwater EC estimates at various depths and at expansive scales. The workflow involved using the airborne EM data to provide bulk EC information (σ_{bulk} in Equation 3.5) and extrapolating porosity values from the surface NMR sites to the whole study area. For the surface NMR inversion, the land-based time-domain EM data were used instead of the

airborne-EM data to define the conductive Earth profile, as the former had a similar scale to the surface NMR survey.

The tortuosity constant α was estimated by calibrating the maps of groundwater EC estimates against field measurements of groundwater EC, which were sourced from the South Australian government drillhole database and the drilling program reported by Amerasinghe et al. (2011). The airborne-EM survey was conducted in 2008 during a multi-year drought, which started in 2001 and ended in 2009. Temporal changes in groundwater EC during this period was assumed to be minimal due to the water restrictions and limited groundwater affecting activities. Therefore, it was considered appropriate to use field observations between 2001 and 2009 for the groundwater EC calibration. This resulted in 53 field observations ranging between 1,900 and 85,000 µS/cm. Whilst it was possible to use a spatially variable tortuosity constant, without geological justification this might lead to overfitting to the observations and unrealistic representation of the system. Therefore, we adopted a parsimonious approach and applied a spatially uniform tortuosity constant. Tortuosity constant values between 0.1 and 2 were evaluated; the scaled root mean squared (SRMS) error ranged from 22% to 92% when compared to the observations. The optimal value was found to be 0.8 which produced the lowest SRMS error. This value is within the range of 0.47 to 1.8 reported by Hill and Milburn (1956) and Carothers (1968). The tortuosity constant value of 0.8 was adopted for both the profiles and maps of groundwater EC estimates.

3.3 Results

3.3.1 Time-domain EM

Inverted bulk EC-depth sections from the time-domain EM data collected in 2017 and 2018 are shown in Figure 3.4. Additionally, we have included bulk EC-depth sections extracted from the 2008 airborne-EM survey (Fitzpatrick and Munday, 2009). Some dissimilarities between the airborne-EM and land-based time-domain EM results are expected due to the difference in resolution, survey method, inversion scheme, as well as site conditions at the time of the survey, including soil wetness, groundwater salinity and climate. The depth of investigation was estimated to be ~20 m for the airborne-EM (Fitzpatrick and Munday, 2009) and between 19 and 28 m for the land-based time-domain EM. The noise level for the land-based time-domain EM is generally less than 1%. Figure 3.4 shows a resistive layer near the surface at all sites, with a thickness of 4 – 6 m for most transects except Transect West which has a thickness of up to 11 m. Below the resistive layer, a conductive layer was found at all sites with varying bulk EC ranging between 18,000 and 26,000 µS/cm.

Time-lapse comparison of transects can inform the impact of watering on groundwater salinity. The simple water balance model (Section 3.2.1) indicates the watering may freshen at most the top 5 m of the floodplain groundwater. However, Figure 3.4 shows little bulk EC change before and after watering at most sites, except Transect East 2 where bulk EC decreased considerably after the watering. This is further delineated in Figure 3.5, which shows the percentage change of bulk EC between the 2017 and 2018 surveys for Transect East 2. A negative value indicates a bulk EC reduction while a positive value indicates a bulk EC increase after the watering. Figure 3.5 shows an increase in bulk EC in the resistive layer near the surface and a decrease in bulk EC in the conductive layer (except the western part of the transect) after watering.

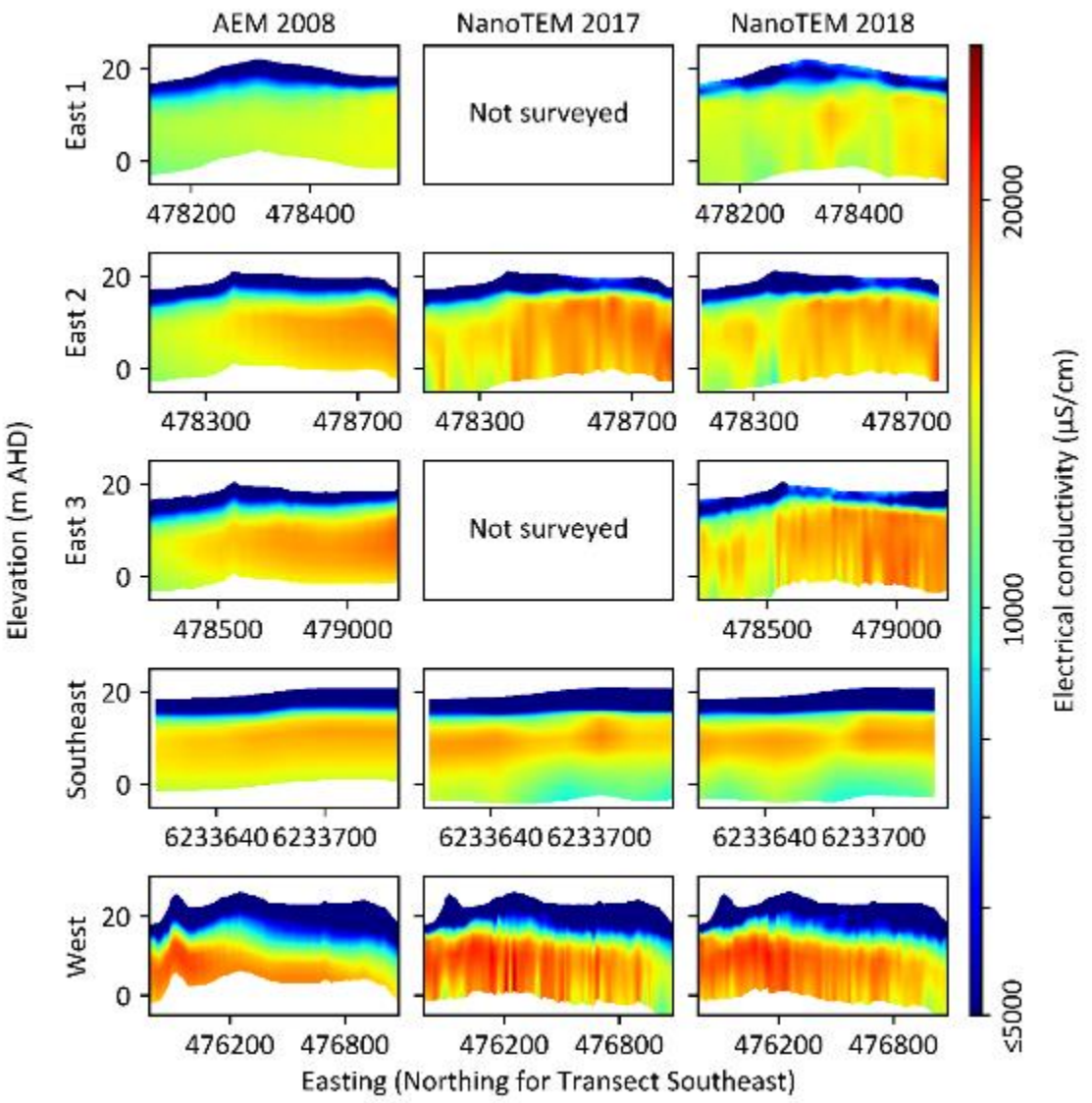

Figure 3.4 Bulk EC profiles from the 2008 airborne-EM survey (Fitzpatrick and Munday, 2009) and the 2017 and 2018 time-domain EM surveys. Some dissimilarities between the airborne-EM and land-based time-domain EM results may be attributed to the difference in resolution, survey method, inversion scheme, as well as site conditions at the time of the survey. Transects East 1 and 3 were new sites added in the 2018 survey and not surveyed in 2017. Transect West is a control site and shows the seasonal variation of bulk EC is minimal. Transient changes in bulk EC are mostly attributed to changes in saturation in the unsaturated zone and groundwater salinity in the saturated zone.

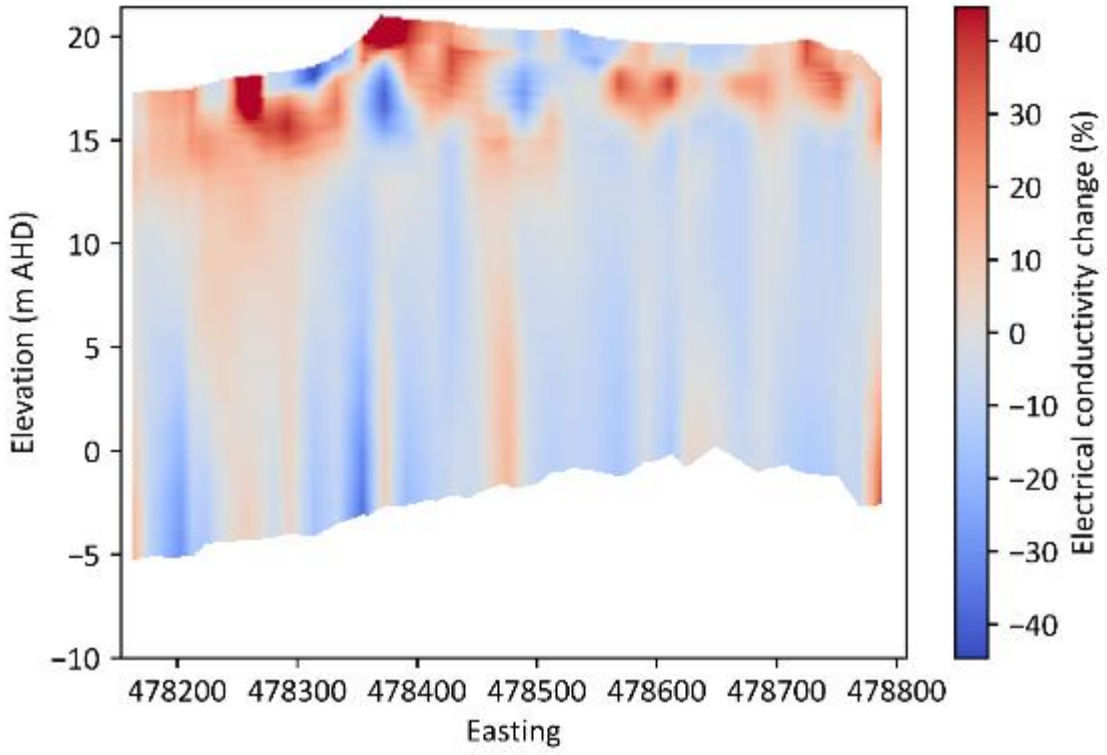

Figure 3.5 Percentage change of bulk EC at Transect East 2 between the 2017 and 2018 surveys, where negative values indicate a bulk EC reduction while positive values indicate a bulk EC increase after the watering.

3.3.2 Surface NMR

The pulse moment and observed FID sequence for all surface NMR sites are shown in Figure 3.6. Most signal comes from pulse moments between 0.1 and 1 As, with measurable decays to 300 – 500 ms. The surface NMR results consist of thee plots for each site, including decay time constant T_2*, volumetric water content and hydraulic conductivity (Figure 3.7). The decay time constant T_2* plot is useful for lithological interpretations where a longer T_2* generally indicates a larger pore, and vice versa. The total water content is a proxy for porosity in the saturated zone where all pores are filled with water. However, this proxy relationship is not applicable to the unsaturated zone where pores are not completely filled with water. Depending on the degree of saturation, the unsaturated zone generally has a very short decay time, making it difficult to be detected by conventional surface NMR systems (Walsh et al., 2011). Similarly, units with large amounts of clay and silt are hard to detect using surface NMR as the dead-time is often too long to detect the short decays that characterise clays and silts (Walsh et al., 2011).

Applying this information to our field area, it is likely that the porosity of the surface Coonambidgal Clay unit is underestimated due to its short decay time, both due to the fact that parts of the unit may be unsaturated, as well as the fact that the clays are hard for the surface

NMR to detect. In this study, the unit that we are most interested in is the underlying Monoman Sands unit. As stated earlier, we expect this unit to be primarily made up of sand, with only occasional presence of silty clay.

In Figure 3.7, the T_2* distributions, water content and hydraulic conductivity plots all decrease toward the bottom of each plot, which is likely to be due to signal attenuation. The depth of investigation was estimated by the inversion algorithm to be between 27 and 33 m. Figure 3.7 also shows the noise levels estimated by the inversion for all sites to be less than 3%. The overall signal-to-noise ratios were calculated to range from 40.0 at site 1 to 74.8 at site 6 with a mean of 59.8, justifying the use of multi-exponential inversion for the surface NMR data (Lubczynski and Roy, 2003, Boucher et al., 2011).

We undertook an additional surface NMR sounding at Site 6 with a shorter pulse duration time of 20 ms to evaluate the impact of pulse duration time on the NMR-derived hydraulic conductivity (Figure 3.8). The two sets of hydraulic conductivity estimates are similar until about 9 m depth, below which hydraulic conductivity is overestimated by the 40 ms pulse due to the missing short signals from the silty clays. Since we are only interested in the spatial trends of hydraulic conductivity (not the actual values), and the two sets of hydraulic conductivity estimates show similar trends, we believe it is reasonable to use the 40 ms pulse duration time to estimate relative hydraulic conductivity.

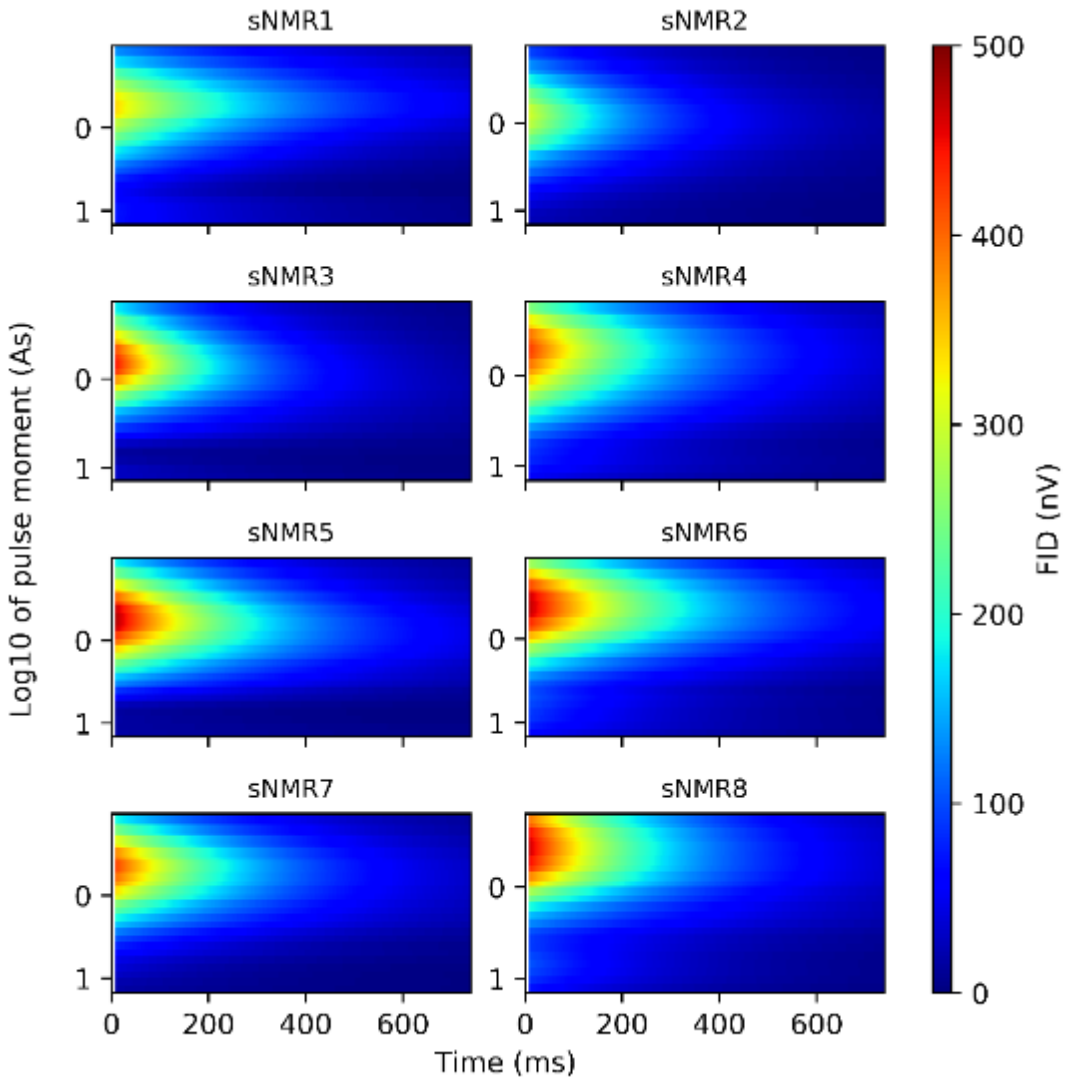

Figure 3.6 Pulse moment and observed FID sequence for all surface NMR sites. Most signal comes from pulse moments between 0.1 and 1 As, with measurable decays to 300 – 500 ms.

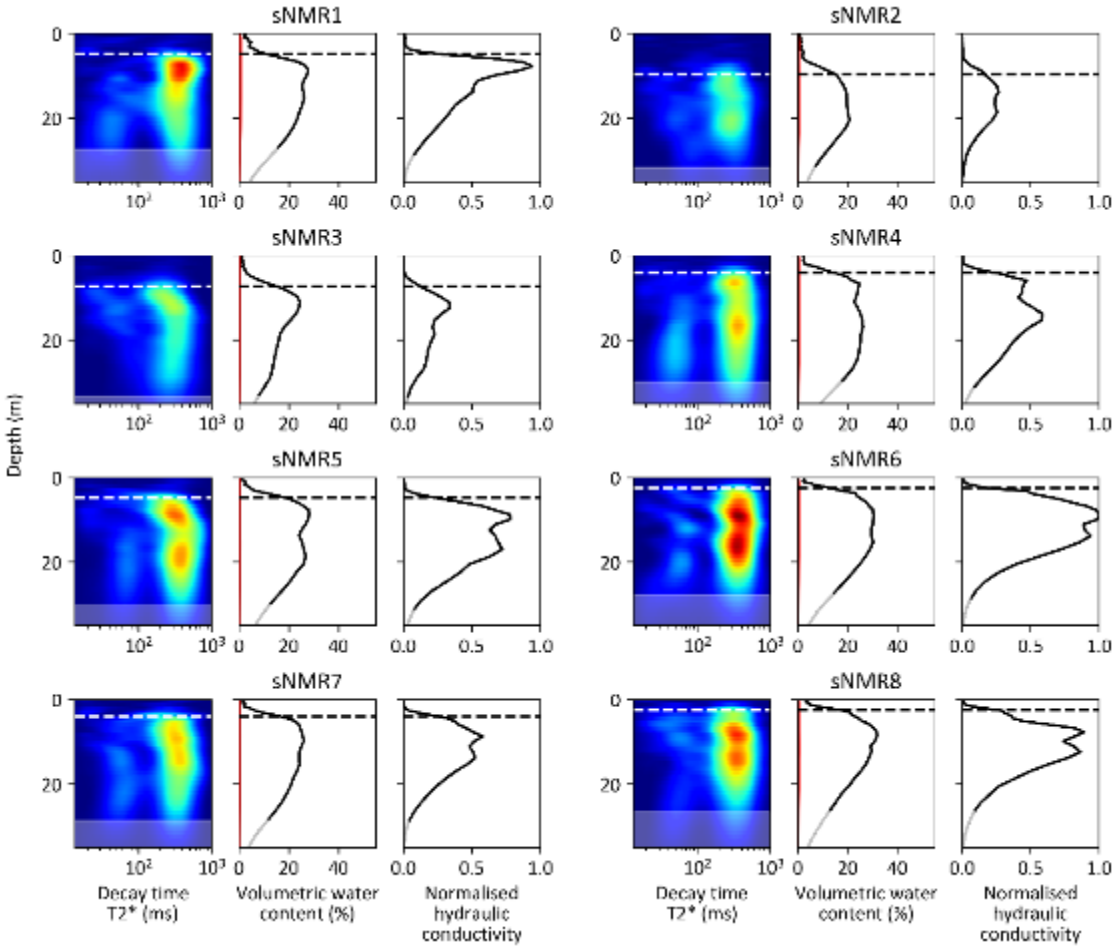

Figure 3.7 Surface NMR results for all sites. Warm colours in the decay time T_2* plots correspond to high signal amplitudes, interpreted water table is denoted by dotted lines, and noise is denoted by red lines. The depth of investigation ranges between 27 - 33 m. Data below the depth of investigation are masked to indicate the lower confidence on these values.

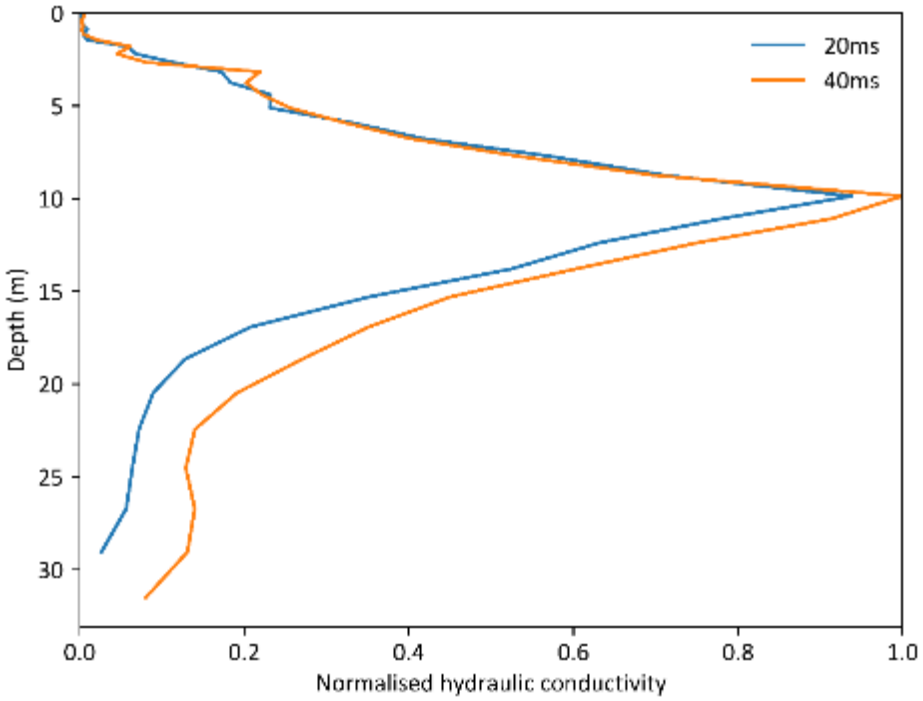

Figure 3.8 Comparison of NMR-derived hydraulic conductivity estimates between the pulse duration time of 20 ms and 40 ms at site 6.

3.3.3 Groundwater EC

Groundwater EC profiles were developed using the time-domain EM and surface NMR. Both results from the ground EM surveys and the older airborne-EM data are shown in Figure 3.9. Note that Transects East 1 and 3 were not surveyed in 2017.

As described earlier, our method is not applicable to the unsaturated zone where the water content data from surface NMR cannot be used as a proxy for porosity, hence this zone has been greyed out in Figure 3.9 and was not used in our calculations. For a given EM transect, the depth to water table was estimated from the surface NMR data (Figure 3.7) and linearly interpolated between the NMR sites, or applied uniformly if the transect only has one NMR sounding. As there are no surface NMR soundings near Transect Southeast, the 2008 water table map from Amerasinghe et al. (2011) was used to estimate groundwater depth along this transect. Given the minimal groundwater-affecting activities and the small watering volume in this area, this approach is not likely to cause large errors in our analysis.

Groundwater EC maps at various depths were also created using the airborne-EM data (Figure 3.10). The depth of investigation for the airborne-EM was estimated by Fitzpatrick and Munday (2009) to be ~20 m, hence we only used depths from the airborne-EM inversion up to 19.4 m

below the surface. Similarly, depth slices shallower than the mean water table depth of 4.9 m are considered influenced by the unsaturated zone and excluded. The calculated groundwater EC maps are compared with field observations in Figure 3.11, with the observation locations shown in Figure 3.10. A 1:1 reference line is included Figure 3.11 to represent the ideal situation where the calculations match the observations. The residuals range approximately between 950 and 36,000 µS/cm, with a SRMS error of 21%.

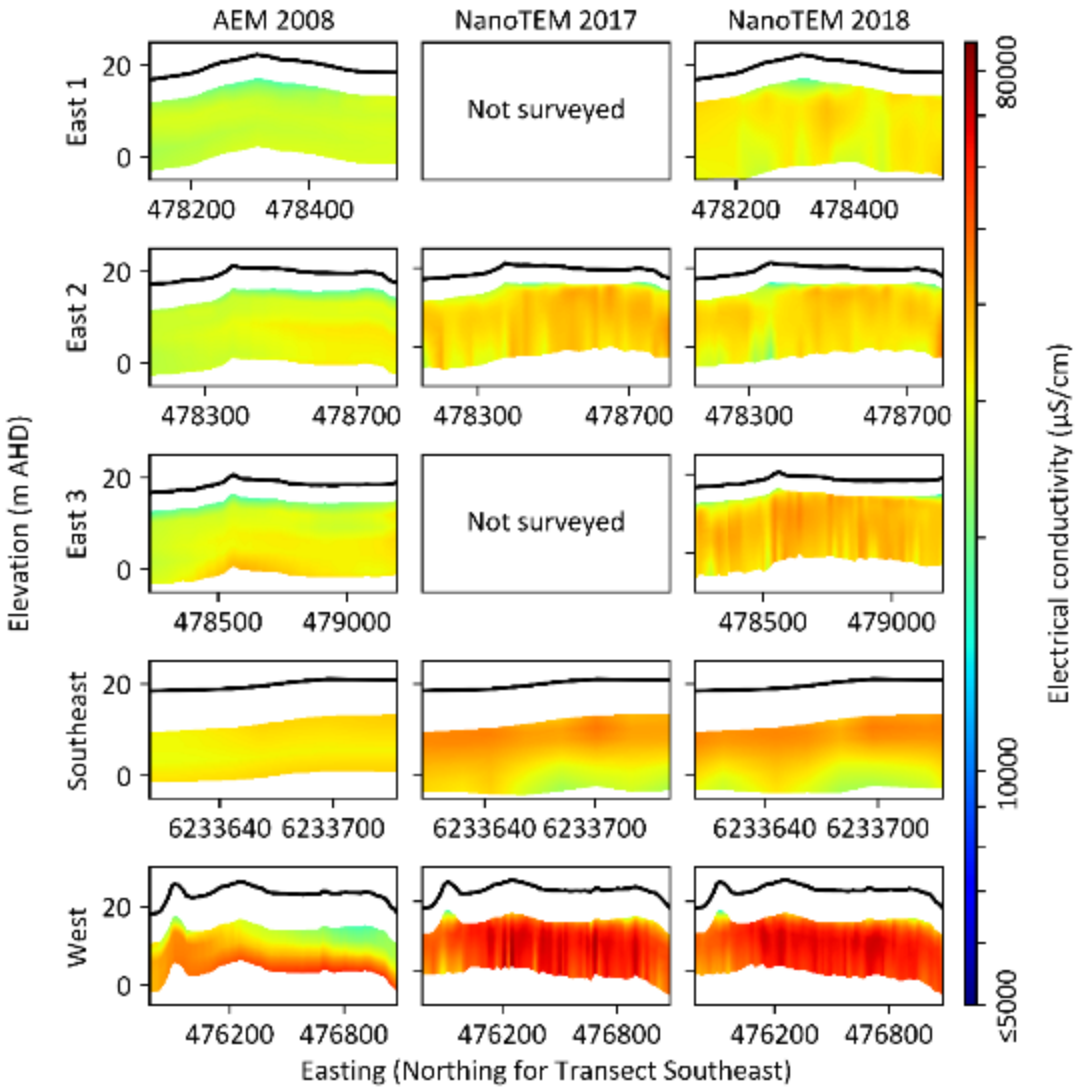

Figure 3.9 Groundwater EC profiles developed using surface NMR and EM. The unsaturated zone has been greyed out as the water content from surface NMR cannot be used as a proxy for porosity in this zone. Some dissimilarities between the airborne-EM and land-based time-domain EM results may be attributed to the difference in resolution, survey method, inversion scheme, as well as site conditions at the time of the survey. Transects East 1 and 3 were not surveyed in 2017.

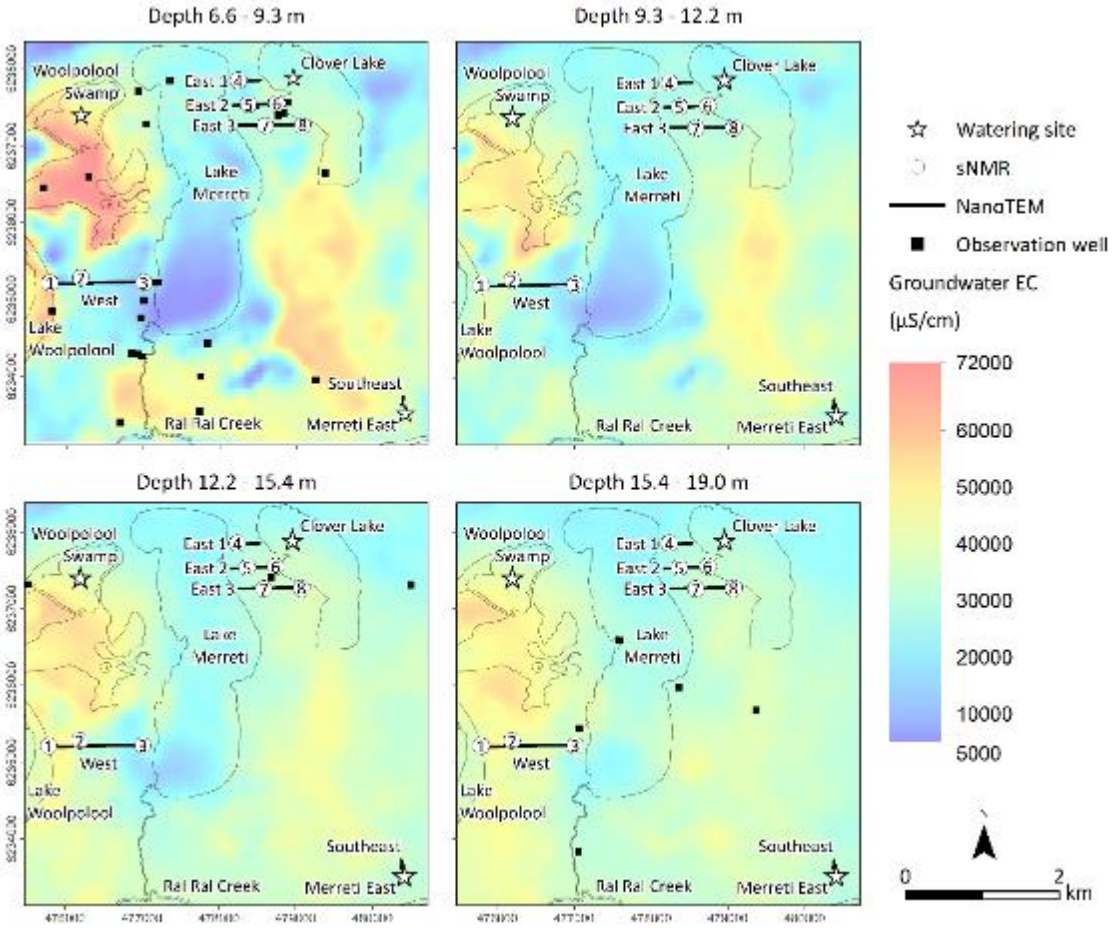

Figure 3.10 Groundwater EC maps developed using surface NMR (sNMR) and airborne-EM. The airborne-EM depth slices deeper than 19 m are beyond the penetration depth of surface NMR and airborne-EM and therefore excluded. Depth slices shallower than 6.6 m are considered influenced by the unsaturated zone and also excluded. Observation wells are displayed in the depth slices based on their screen depth.

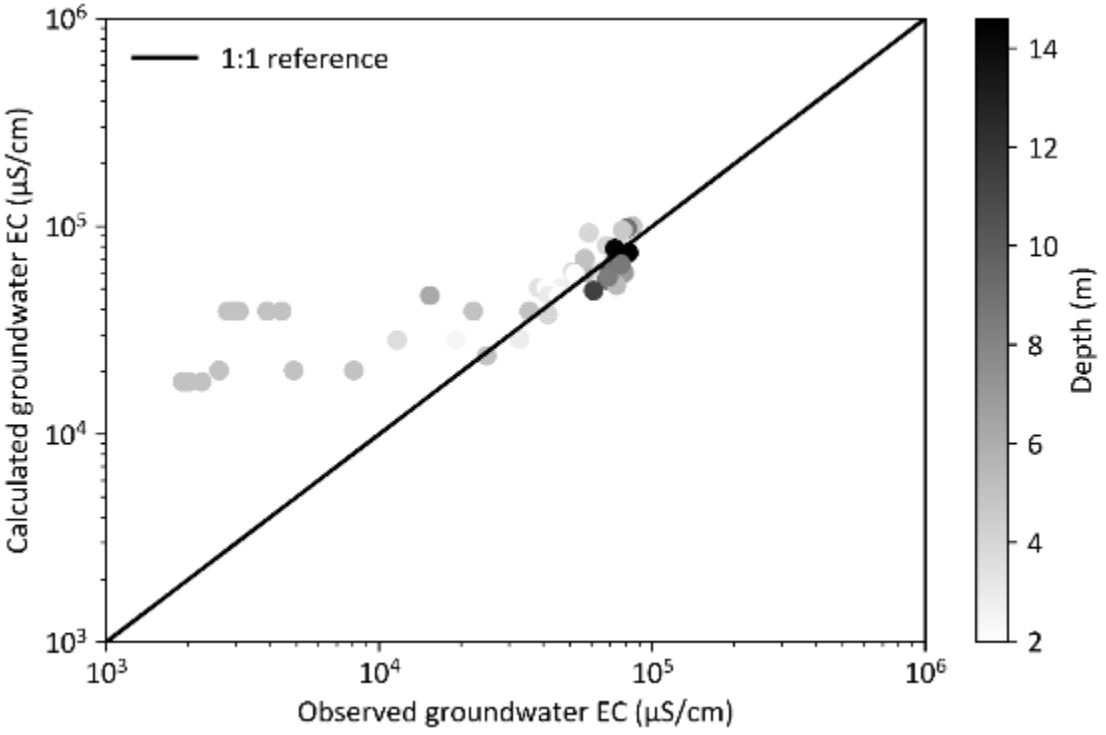

Figure 3.11 Comparison of the calculated groundwater EC maps with field observations. The point colour intensity indicates the borehole screen depth. The 1:1 reference line represents the ideal situation where the calculations match the observations.

3.4 Discussion

3.4.1 Floodplain processes and hydrogeology

In this study EM and surface NMR are used to assess the salinity impact of watering on the saline groundwater in the study area. This section describes what insights can be provided by these techniques individually, and what additional information can be gained when they are used jointly.

3.4.1.1 Time-domain EM interpretations

The bulk EC transects based on the time-domain survey results (Figure 3.4) provide insight into the how the floodplain responds to watering. Interpretation on the watering impact based on a single set of data collected at an instant in time is likely to be ambiguous as it is difficult to distinguish the influence of clay and groundwater EC on the measured bulk EC. When looking at two sets of data that reflect a change in hydrological conditions, the clay content is assumed to remain constant, while groundwater EC can change with time. Bulk EC may also be affected by temperature changes but its impact is expected to be minimal given the small air temperature difference between the first survey (26.3°C) and second survey (31.2°C) (Bureau of Meteorology, 2018, Bureau of Meteorology, 2019). Additionally, the temperature difference between surface water (19°C from the nearest monitoring site) and groundwater (21°C from the drillhole data) is also small. Therefore, nearly all transient changes in bulk EC in the saturated zone can be attributed to changes in groundwater EC, which may be caused by seasonal variations and/or artificial watering. It is therefore necessary (as was done here) to repeat surveys during at least different seasonal conditions and, if possible, different climatic conditions to be able to quantify bulk EC temporal variability. In this study the data collected at Transect West is used as a control, given its relatively long distance of 2.2 km from its closest watering site at Woolpolool Swamp. The logarithmic mean of bulk EC at this transect is 10,000 µS/cm for the 2017 survey and 10,224 µS/cm for the 2018 survey, suggesting seasonal variation in bulk EC is minimal (approximately 2%).

The locations of Transects East 2 and 3 were designed to estimate the impact of watering from Clover Lake. Comparison of the EM results at Transect East 2 (Figure 3.4 and Figure 3.5) demonstrates how some parts of the floodplain may respond rapidly to a single watering event. Figure 3.5 shows the bulk EC changes at this transect before and after the watering event. An increase in bulk EC is observed after the watering in the near-surface, up to approximately 5 m depth. This is mostly the unsaturated zone (Figure 3.9), where an increase in bulk EC may suggest a rise in soil moisture. Below the unsaturated zone, Figure 3.5 shows a considerable

bulk EC reduction after the watering in the top 20 – 25 m depth with a mean reduction of approximately 7% (930 µS/cm), ranging up to 45% (5,200 µS/cm) at some locations.

No ground EM data were collected at Transect East 3 in 2017, so it is more difficult to interpret the results at this site. The airborne-EM data show that Transects East 2 and 3 had similar bulk EC in 2008 well before the watering (Figure 3.4). However, the 2018 ground EM data show that Transect East 3 has a notably higher bulk EC than Transect East 2 after the watering (Figure 3.4), suggesting the impact of watering on groundwater salinity is potentially less profound at Transect East 3. Furthermore, given the proximity of the two transects, this result suggests that the impact of watering on groundwater salinity is highly localised and heterogeneous.

3.4.1.2 Surface NMR interpretations

Surface NMR provides valuable information on the floodplain hydrogeological parameters. Figure 3.7 shows that the Monoman Sands aquifer in this area is characterised by relatively long T_2*, reflecting large pore size. From these plots the water table was interpreted to occur between 2.4 m depth near surface water bodies and 9.6 m in the higher elevation areas.

The water content plots (Figure 3.7) are used as a proxy for porosity in the saturated zone where all pores are filled with water. The south-western sites (Sites 1 – 3) show a porosity of 10% - 36% (with a mean of 16%), while the north-eastern sites (Sites 4 – 8) show a porosity of 16% - 38% (with a mean of 23%). Normalised hydraulic conductivity is relatively low in the south-western area, especially at Sites 2 and 3 with a normalised mean of 0.12 – 0.13. In the north-eastern area, sites near Clover Lake (Sites 6 and 8) show a considerably higher normalised mean hydraulic conductivity of 0.73 – 1, while the sites near Lake Merreti (Sites 4, 5 and 7) show a slightly lower normalised mean of 0.43 – 0.62.

3.4.1.3 Joint EM - surface NMR interpretations

Groundwater EC profiles were created using EM and surface NMR (Figure 3.9). Transect East 1 is close to a natural flood channel and is therefore an example of a site with natural access to fresh surface water. Figure 3.9 shows that groundwater EC at this transect was already relatively low prior to the watering, possibly due to mixing with surface water. This indicates the watering benefit on this type of sites may be relatively small as there is not much room for further improvement.

Transect Southeast is close to the watering site Merreti East, which is different from the other watering sites in that it has been receiving relatively small amount of watering annually since 2015 (100,000 m^3/y). This study was part of a larger field campaign that included an

independent ecological survey, which reports the tree conditions at this site have improved since the onset of watering in 2015, implying an increase in soil water availability and/or decrease in soil water salinity. However, the calculated groundwater EC at this site is relatively high with a mean of 35,000 µS/cm (Figure 3.9). It is hypothesized that the limited watering was sufficient to flush some salt away from the unsaturated zone; this process adds more salt to the saturated zone and a larger amount of watering is needed to dilute this extra salt. This hypothesis can be tested by trialling a larger amount of watering and observing how groundwater EC changes after the watering.

The calculated groundwater EC at Transect West is considerably higher than the other transects, with a mean of 50,400 µS/cm, with values up to 82,000 µS/cm at some locations. The nearby borehole data show a large groundwater EC range between 10,000 and 62,000 µS/cm, where the lower groundwater EC values are observed near Lake Merreti and believed to be influenced by mixing. This very high level of calculated groundwater EC, although uncommon, has been observed in other nearby River Murray sites in the government drillhole database, including the Pike floodplain (106,000 µS/cm), Gurra Gurra Lake (108,000 µS/cm), Yatco Lagoon (114,000 µS/cm), Lake Bonney (109,000 µS/cm), Wongulla Lagoon (144,000 µS/cm) and Tapoo Lagoon (124,000 µS/cm). On the other hand, the mean calculated groundwater EC is approximately 29,500 µS/cm at East 1, 32,600 µS/cm at East 2, 33,500 µS/cm at East 3 and 35,300 µS/cm at Southeast, all similar to the mean field observation of 22,700 µS/cm in the study area.

Spatial distributions of groundwater EC were developed using airborne-EM and surface NMR for various depths (Figure 3.10). These groundwater EC maps represent the 2008 condition and hence do not inform the impact of watering. Nevertheless, these maps provided information on the surface water-groundwater interactions in the study area, which was useful for managing water levels at Lake Merreti and Woolpolool. It is a management concern whether over-filling Lake Merreti without filling Lake Woolpolool would drive the saline groundwater towards Lake Woolpolool and cause adverse impacts. The groundwater EC map for the 6.6 – 9.3 m depth interval shows that the groundwater EC under Lake Woolpolool is higher than the surrounding area. Therefore, it seems unlikely that filling Lake Merreti will cause much negative impact on the salinity of groundwater underneath Lake Woolpolool. However, the hydrogeological processes are complex, and filling Lake Merreti may raise the groundwater pressure below Lake Woolpolool, resulting in increased saline groundwater discharge to the lake. This hydraulic effect is considered out of scope for this study and is a matter for future investigations.

Lake Merreti is a freshwater lake with a mean EC of 650 µS/cm. It loses water to the aquifer in its vicinity (Steggles and Tucker, 2003), creating a low EC plume in the southwest corner of the lake (Figure 3.10). The groundwater EC maps indicate the freshening impact of Lake Merreti has a lateral extent of about 100 m at 6.6 – 9.3 m depth, which diminishes with depth (compare with deeper slices in this area).

3.4.2 Evaluation of the groundwater EC estimation

Airborne-EM and surface NMR are used to develop groundwater EC maps at various depths (Figure 3.10). These groundwater EC maps are compared with field observations in Figure 3.11, with a 1:1 reference line to represent the ideal situation where the calculations match the observations. Figure 3.11 shows that for the higher observed groundwater EC range (higher than approximately 24,000 µS/cm), the calculations match the observations reasonably well. However, the calculations overestimate groundwater EC in the lower observed groundwater EC range. Figure 3.11 shows that these observations are relatively shallow, mostly with a depth of 5 m or less. Given their shallowness, it is possible that their airborne-EM readings were influenced by the presence of the surface Coonambidgal Clay, which increases their bulk EC readings and causes groundwater EC to be overestimated.

When applying this methodology to other areas, one needs to be aware of its underlying assumptions and limitations. The key assumption is that there is minimal silt and clay in the aquifer of interest, so that Archie's Law can be applied (Archie, 1942). The main limitation of our method is its inability to provide information on the unsaturated zone, which is important for managing vegetation health. The water signal in the unsaturated zone is generally too small to be detected by conventional surface NMR (Walsh et al., 2011). In addition, the proxy relationship between water content and porosity is only applicable to the saturated zone, where all pores are completely filled with water. This is not the case in the unsaturated zone, where porosity may be larger than water content. Unfortunately, usually only limited information about soil saturation is provided by EM. Further research on using EM and surface NMR to estimate water salinity in the unsaturated zone would be highly beneficial for floodplain management.

3.5 Conclusions

This study uses EM and surface NMR to investigate the salinity impact of artificial environmental watering on the Calperum floodplain, a semi-arid, highly conductive floodplain in the South Australian River Murray region. We examined the changes in bulk EC at five sites before and after a watering event, where one site showed a bulk EC reduction of up to 5,200 µS/cm, suggesting groundwater was freshened, while data collected at nearby locations showed very little change in bulk EC. This demonstrates the salinity impact of watering is highly localised and heterogeneous.

For ecological management purpose, it is also desirable to estimate groundwater EC so that groundwater results may be compared directly, both before and after the watering. EM alone is inadequate for this purpose due to the interpretation ambiguity between clay and groundwater EC and the need to convert bulk EC to groundwater EC. This study presents a method to reduce this interpretation ambiguity in a highly conductive environment by coupling EM with surface NMR through a modified version of Archie's Law. This method enables the estimation of groundwater EC as well as improves the conceptualisation of floodplain processes. We extended the salinity analysis to an airborne-EM survey to derive spatial distribution of groundwater EC at various depths, which shows an overall good agreement with field observations, with a few exceptions at shallow depths which may have been influenced by the surface clay.

This study demonstrates the potential benefits of using geophysics to improve the understanding of floodplain dynamics. In this study we used time-domain EM to characterise the EC distribution of the subsurface and surface NMR to help understand the gaps in knowledge presented by the time-domain EM. The methodology and framework developed in this study are useful for first-pass assessments of subsurface water quantity and quality in a non-invasive manner, which are transferrable to many other fresh or saline groundwater systems, especially in ecologically sensitive areas where traditional hydrogeological techniques may not be suitable due to the potential disturbance of local ecosystems.

Acknowledgements

This research is supported by an Australian Government Research Training Program (RTP) Scholarship through the University of Adelaide of South Australia, a CSIRO scholarship and the Department of Environment and Water of South Australia. We would like to thank Brady Flinchum, Kevin Cahill, Aaron Davis, Tim Munday, Luk Peeters, Todd Wallace, Tanya Doody, Chris Turnadge, Kate Holland, Elliot Grunewald, Juliette Woods, Graham Green and Peter Cale for their technical and field assistance.

4 Integrating TEM and surface NMR with hydrogeological modelling

Chris Li[a, b]

Rebecca Doble[a]

Michael Hatch[b]

Graham Heinson[b]

[a] CSIRO Land and Water, Glen Osmond, South Australia, Australia

[b] The University of Adelaide, Adelaide, South Australia, Australia

Submitted to *Geophysics* in July 2020

Statement of Authorship

Title of Paper	Integrating TEM and surface NMR with hydrogeological modelling
Publication Status	Submitted for Publication
Publication Details	In review with the journal *Geophysics* (submitted 29 July 2020)

Principal Author

Name of Principal Author (Candidate)	Ho Yin Li (Chris)		
Contribution to the Paper	Conception and design Collection, analysis and interpretation of data Writing the manuscript		
Overall percentage (%)	90		
Certification:	This paper reports on original research I conducted during the period of my Higher Degree by Research candidature and is not subject to any obligations or contractual agreements with a third party that would constrain its inclusion in this thesis. I am the primary author of this paper.		
Signature		Date	20 August 2020

Co-Author Contributions

By signing the Statement of Authorship, each author certifies that:

i. the candidate's stated contribution to the publication is accurate (as detailed above);

ii. permission is granted for the candidate in include the publication in the thesis; and

iii. the sum of all co-author contributions is equal to 100% less the candidate's stated contribution.

Name of Co-Author	Rebecca Doble		
Contribution to the Paper	Conception and design Critically revising the manuscript		
Signature		Date	20 August 2020

Name of Co-Author	Michael Hatch		
Contribution to the Paper	Conception and design Critically revising the manuscript		
Signature		Date	20 August 2020

Name of Co-Author	Graham Heinson		
Contribution to the Paper	Conception and design Critically revising the manuscript		
Signature		Date	20 August 2020

Abstract

Groundwater models have an implicit uncertainty due to an inadequate characterization of the hydrogeological properties of the sub-surface. Such uncertainty may be reduced by using geophysics to provide additional hydrogeological constraints. This study evaluates the use of Time-domain Electromagnetics (TEM) and Surface Nuclear Magnetic Resonance (SNMR) to derive hydraulic conductivity for groundwater modelling in a sedimentary setting. A suite of reference models was developed to represent various hydrogeological scenarios. Hydrogeological and geophysical data were computed from these reference models and used in different combinations to create a range of groundwater model ensembles. The performance of these model ensembles was evaluated by comparing their predictions to those of the reference models. We found that using only TEM to derive hydraulic conductivity via an empirical petrophysical relationship does not necessarily reduce the prediction uncertainty of groundwater models, due to uncertainty of the empirical constants in the petrophysical relationship. However, SNMR provides additional constraints on the empirical constants and hence hydraulic conductivity, greatly reducing the prediction error and uncertainty of groundwater models. Our method of coupling TEM and SNMR with groundwater modelling can be useful especially in areas with limited aquifer test data.

4.1 Introduction

Numerical modelling is a useful tool for groundwater resource management as it enables the prediction of impact from different management options based on the currently available data and knowledge (Doherty & Simmons, 2013). However, these predictions may potentially be erroneous due to the uncertainty in data, conceptualization and parameterization (Voss, 2011a, 2011b). This is partly due to an inadequate characterization of the sub-surface as classical hydrogeological techniques provide mostly point-scale information, while groundwater models generally require spatially continuous data (Brunner, Franssen, Kgotlhang, Bauer-Gottwein, & Kinzelbach, 2007). This mismatch can be mitigated using geophysics due to its denser spatial coverage, non-invasiveness and relatively low-cost on an area basis (Slater, 2007).

Time-domain electromagnetics (TEM) is commonly used to assist groundwater modelling. For example, Harrington, Gardner, and Munday (2014) applied TEM to provide information on aquifer structure and groundwater salinity for estimating groundwater discharge to the Fitzroy River in Western Australia. Herckenrath et al. (2013) used TEM data to assist parameterization of a saltwater intrusion model for Pajaro Valley, California. For model parameterization, electrical conductivity (EC) estimated by TEM can be related to hydraulic conductivity via a petrophysical relationship, which often contains empirical constants that need to be calibrated against field data, ideally aquifer test data (Slater, 2007). However, aquifer test data typically represent an areal average with a considerably different scale compared to TEM data. It may be beneficial to have an additional set of hydraulic conductivity estimates, preferably at a similar scale to TEM, to provide constraints on the empirical constants.

Surface Nuclear Magnetic Resonance (SNMR) is gaining traction in hydrogeology as it detects sub-surface water directly (Legchenko, Baltassat, Beauce, & Bernard, 2002). This technique involves exploiting the nuclear properties of hydrogen protons in sub-surface water to provide hydrogeological information. The initial amplitude and decay pattern of the received signal are used to estimate water content and the decay time constant T_2* respectively. The former is a proxy for porosity in the saturated zone, while the latter is related to pore size and can be used to derive hydraulic conductivity via a petrophysical relationship (Behroozmand, Keating, & Auken, 2014).

Despite the potential described above, application of SNMR in groundwater modelling is not common. Lubczynski and Gurwin (2005) applied SNMR to improve the hydrogeological conceptualization, identify the hydrostratigraphic boundaries and derive storage coefficients for a groundwater model to evaluate the variability of groundwater recharge and

evapotranspiration in Sardon, Spain. Boucher et al. (2012) used SNMR to estimate transmissivity and specific yield for an existing groundwater model to evaluate groundwater recharge in southwestern Niger. Despite these efforts, however, the benefits of incorporating SNMR into groundwater modelling, such as the impact on prediction error and uncertainty, have not been formally evaluated in a systematic manner and remain as a knowledge gap.

The research objective of this study is to evaluate the use of TEM and SNMR to derive hydraulic conductivity for groundwater modelling in a sedimentary setting using a synthetic approach. To isolate the improvement on hydraulic conductivity, other potential benefits from these geophysical techniques, such as improved conceptualization, are considered out of scope in this study. A suite of reference models was developed to represent various hydrogeological conditions. Hydrogeological and geophysical data were then synthetically sampled from these reference models and used in different combinations to create various ensembles of groundwater models. Performance of these model ensembles was evaluated by comparing their predictions with those of the reference models. This study addresses the knowledge gap of the usefulness of TEM and SNMR for groundwater modelling in a systematic manner, particularly for scenarios of areas with limited aquifer test data.

4.2 Methods

Numerical models characterized by hydrogeological and geophysical properties were developed and referred to as the reference models. From these models, synthetic hydrogeological, TEM and SNMR data were generated based on typical field operations. Such data were then combined in various ways to generate a range of groundwater model ensembles to predict the impact of a groundwater extraction well on the water loss of a nearby river after one year of operation. The performance of the model ensembles was evaluated by comparing their predictions with those of the reference models.

The reference models were qualitatively based on the South Australian River Murray floodplains, which have high ecological value (Connell and Grafton, 2011). The hydrogeology of these floodplains typically consists of a sand layer overlying a clay layer, which has a typical thickness of 5 m but may be absent in places (Evans and Kellett, 1989). Groundwater in these floodplains is naturally saline with a mean EC of 40,000 µS/cm (Herczeg et al., 2001). However, losing surface water features may create freshwater lenses with a typical salinity of 550 µS/cm (Werner and Laattoe, 2016). The River Murray is the regional groundwater sink and receives saline groundwater discharges from the floodplains (Evans and Kellett, 1989). This is of concern for water managers as the River Murray is one of the principal water supplies for the city of Adelaide and other regional towns. Various hydrogeological conditions may be observed in a typical South Australian River Murray floodplain, including (1) the presence/absence of a surface clay layer, (2) high and low groundwater salinities, and (3) homogeneity and heterogeneity of aquifer properties.

The presence of clay and/or a higher groundwater salinity decreases the penetration depth of TEM and SNMR (Everett, 2013), resulting in less information for groundwater modelling. Heterogeneity affects the relative value of TEM and SNMR for groundwater modelling as their denser spatial coverage is more advantageous for characterizing highly heterogeneous groundwater systems.

4.2.1 Hydrogeological reference models

Four hydrogeological reference models were created (Figure 4.1) using MODFLOW-2005 (Harbaugh, 2005). These are 2D cross-sectional models consisting of 500 columns and 50 layers. With a uniform cell height and width of 1 m, these models cover an extent of 500 m horizontally and 50 m vertically. The ground surface was set to be flat at 50 m above sea level (asl).

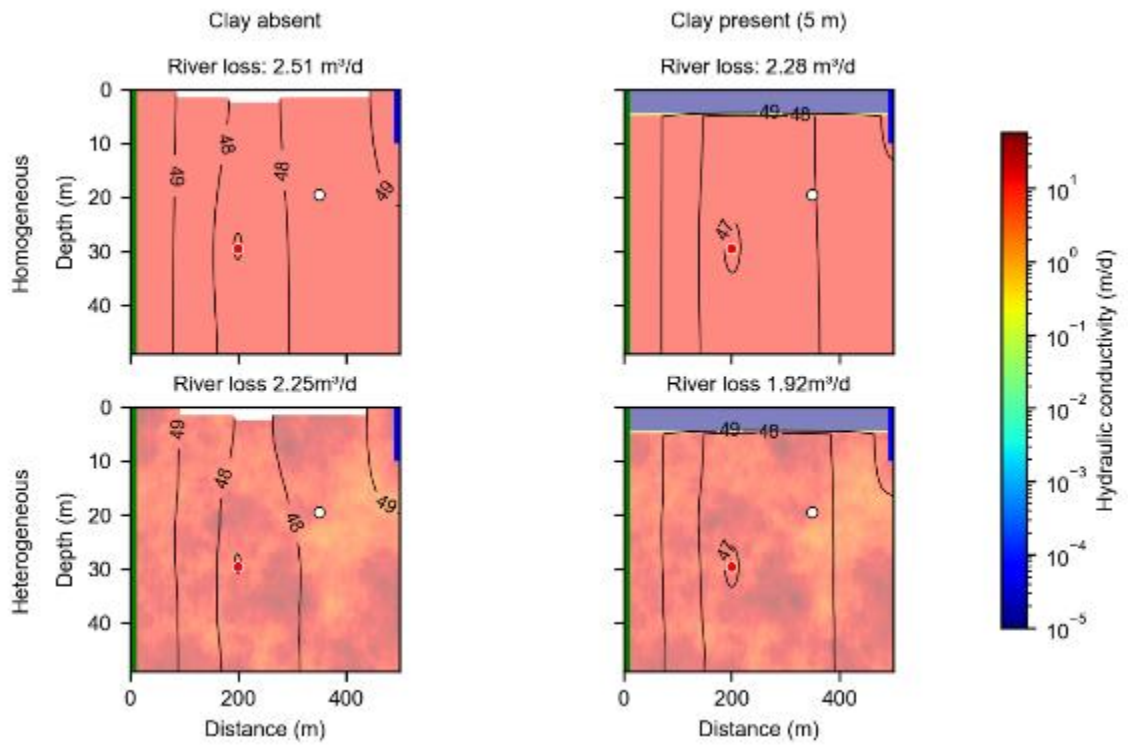

Figure 4.1 Hydrogeological reference models representing different clay conditions and heterogeneities. The green column denotes a constant head boundary, the blue column denotes a river boundary, the red dot denotes the screen of an extraction well, the white dot denotes the screen of an observation well, the contours represent groundwater levels (m asl) from the second stress period where pumping occurs, and the blank space represents dry cells caused by the pumping. A vertical exaggeration of 10 is applied.

The models consist of two stress-periods. The first stress-period is steady-state and represents pre-pumping conditions. Its initial groundwater levels were set to the surface elevation. The second stress-period is transient and has a length of 1 year, 10 time-steps and a time-step multiplier of 1.2. Groundwater extraction is simulated in the second stress-period at a rate of 0.1 L/s, located at column 200 and layer 30 (Figure 4.1). Groundwater level observations were measured at the extraction well and an observation well located at column 350 and layer 20 (Figure 4.1).

A river boundary was set at column 500 and between layers 1 and 10 (Figure 4.1). The river stage was set to the surface elevation. A river depth of 10 m was used, which is greater than the average River Murray depth of ~5 m (Bormans et al., 1998) but adopted to increase the river-aquifer interactions. Riverbed conductance was set to 1 m²/d.

A constant head boundary was created at column 1 for all layers to provide lateral inflow. The head-value was set to the surface elevation. Combined with the river boundary, this resulted in the water table being at the surface prior to pumping. This condition may be uncommon in the

field but was adopted to simplify the development of the TEM and SNMR reference models by omitting the unsaturated zone. Additionally, for parsimony reasons groundwater recharge and evapotranspiration were not simulated.

The modelled aquifer comprises predominantly of medium grain size sands with a hydraulic conductivity of 10 m/d (Fetter, 2018). This value was applied uniformly in the homogeneous models. For the heterogeneous models, this value was used as the mean value to generate a randomly distributed geostatistical field via FIELDGEN (Doherty et al., 1994), ranging between 1.3 and 56.3 m/d (Figure 4.1). For models with clay, a surface clay layer with a uniform thickness of 5 m was included. This clay layer comprises of fluvial clays and silts with a hydraulic conductivity of 10^{-5} m/d (Fetter, 2018). Heterogeneity is not considered for the clay layer due to its relatively low hydraulic conductivity and hence small impact on the river loss compared to the sand layer. The vertical-to-horizontal hydraulic conductivity anisotropy ratio was set to 0.1 (Domenico and Schwartz, 1998, Todd, 1980). A uniform specific storage of 2 x 10^{-4} m^{-1} was adopted for sand and 2 x 10^{-3} m^{-1} for clay (Domenico and Mifflin, 1965), and a uniform specific yield of 0.15 was used for sand and 0.01 for clay (Fetter, 2018).

4.2.2 TEM reference models

Two TEM reference models with different uniform groundwater salinities of 40,000 and 550 µS/cm were developed for each hydrogeological reference model. The TEM reference models contain the true bulk EC (σ_{bulk}) distribution that was derived from groundwater EC (σ_{water}) and hydraulic conductivity.

Permeability and σ_{bulk} are mutually dependent on properties such as pore surface area and volume, and are commonly related via a petrophysical relationship (Slater, 2007). The petrophysical relationship from Purvance and Andricevic (2000) was adopted as follows:

$$k = \frac{\chi \, \sigma_{bulk}^{\frac{m_k}{m\theta}}}{s^2 \, \sigma_{water}^{\frac{m_k}{m\theta}}} \qquad 4.1$$

where k is permeability (m^2), χ is a proportionality empirical constant (dimensionless), s is the pore surface area to volume ratio (m^2/m^3), σ_{bulk} is bulk EC (S/m), σ_{water} is pore water EC (S/m), m_k is the k-porosity power law empirical exponent (dimensionless) and m_θ is the σ_{bulk}-porosity power law empirical exponent (dimensionless).

Permeability is related to hydraulic conductivity by (Fetter, 2018):

$$k = \frac{K \nu}{\rho g} \tag{4.2}$$

where K is hydraulic conductivity (m/s), ν is fluid dynamic viscosity (kg m^{-1} s^{-1}), ρ is fluid density (kg m^{-3}) and g is gravity acceleration (m s^{-2}). By rearranging Equation 4.1 and combining it with Equation 4.2:

$$\sigma_{bulk} = \left(\frac{K \nu s^2}{\rho g \chi}\right)^{\frac{m_\theta}{m_k}} \sigma_{water} \tag{4.3}$$

Equation 4.3 can be simplified to a linear log-log relationship (Purvance and Andricevic, 2000, Slater, 2007):

$$\sigma_{bulk} = \alpha \sigma_{water} K^{\beta} \tag{4.4}$$

where

$$\alpha = \left(\frac{\nu s^2}{\rho g \chi}\right)^{\beta} \tag{4.5}$$

$$\beta = \frac{m_\theta}{m_k} \tag{4.6}$$

where α and β are empirical constants. To derive physically sensible values for these empirical constants, the hydrogeophysical data collected in a typical South Australian River Murray floodplain from Li et al. (2020) and Fitzpatrick and Munday (2009) were used. For the sand aquifer in this floodplain, the airborne-EM data (Fitzpatrick and Munday, 2009) indicate a nominal σ_{bulk} of 10,000 µS/cm, while the hydrogeological data suggest a nominal σ_{water} of 40,000 µS/cm and hydraulic conductivity of 10 m/d (Li et al., 2020). Additionally, we constrained the empirical constant β to be between 0.1 and 1, which is the same order of magnitude as the literature values of 0.55 – 0.9 (Purvance and Andricevic, 2000, Frohlich et al., 1996, Heigold et al., 1979). A simple optimization technique was used to estimate α and β within their respective range that would yield a σ_{bulk} of 10,000 µS/cm, and it was found that α = 0.13 and β = 0.3. Applying these empirical constants in Equation 4.4 yielded a true σ_{bulk} distribution ranging

between 5600 and 17,000 µS/cm for the high salinity case and 80 and 240 µS/cm for the low salinity case.

Equation 4.4 is applicable to aquifers that are predominantly comprised of sands, where a higher σ_{bulk} indicates a higher interconnected pore volume and hence a higher hydraulic conductivity (Purvance and Andricevic, 2000, Slater, 2007). However, Equation 4.4 is not applicable to formations that are predominantly comprised of clays, where a higher σ_{bulk} indicates a higher clay content and hence a lower hydraulic conductivity. Hence the σ_{bulk} of the clay layer was set to a uniform value of 30,000 µS/cm for the high salinity case and 1000 µS/cm for the low salinity case based on the airborne-EM data (Fitzpatrick and Munday, 2009). These σ_{bulk} values were not used to derive hydraulic parameters for the clay layer and were included solely for continuity reasons, which were required for the geophysical inversion.

4.2.3 SNMR reference models

A SNMR reference model was developed for each hydrogeological scenario. The SNMR reference models contain the true water content (a proxy for porosity in the saturated zone), decay time constant T_2* and empirical constant c.

The decay time constant T_2* is estimated from the decay pattern of the received signal and susceptible to magnetic field heterogeneity (Behroozmand et al., 2015). By assuming the geology to be weakly magnetic, T_2* can be used to estimate hydraulic conductivity via the Schlumberger-Doll-Research (SDR) equation (Kenyon et al., 1988):

$$K = c\,\phi^{m}(T_{2ML}{}^{*})^{2} \qquad 4.7$$

where K is hydraulic conductivity (m/s), c is an empirical constant (m s^{-3}), ϕ is porosity (dimensionless), m is an empirical constant (dimensionless) and T_{2ML}* (s) is the geometric mean of the T_2* distribution. A value of c = 0.05 m s^{-3} and m = 1 were adopted based on the values reported by Knight et al. (2016) for unconsolidated aquifers. Porosity was uniformly set to 0.3 for the sand layer (Fetter, 2018). Applying these values in Equation 4.7 yielded a true T_2* field ranging between 30 and 210 ms, which is in the same order of magnitude as the literature values of 90 – 429 ms (Behroozmand et al., 2015).

For the clay layer, a uniform T_2* of 3 ms (Schirov et al., 1991, Sen et al., 1990) and porosity of 0.4 (Fetter, 2018) were applied. These values were not used to derive hydraulic parameters for the clay layer and were included solely for continuity reasons, as the decay time of clay is too short to be detected by conventional SNMR (Walsh et al., 2011).

4.2.4 Hydrogeological reference model sampling

Hydrogeological synthetic data include two groundwater level observations and one aquifer test, comparable to real-world hydrogeological investigations. Groundwater level measurements were derived at the pumping and observation wells from the second stress period where pumping occurs. To account for observation error, predictive data were generated by applying random noise to the true groundwater levels from the reference models (Table 4.1).

Table 4.1 True and Measured Groundwater Levels and Hydraulic Parameters. WL = water level, K = hydraulic conductivity, Ss = specific storage, Sy = specific yield.

Reference model type		WL at pumping well (m asl)		WL at observation well (m asl)	
Distribution	**Clay thickness (m)**	**True**	**Measured**	**True**	**Measured**
Homogeneous	0	45.79	45.94	48.33	48.20
	5	45.50	45.65	47.96	47.83
Heterogeneous	0	45.65	45.81	48.21	48.08
	5	45.32	45.47	47.78	47.65

Reference model type		K (m/d)		Ss (m^{-1})		Sy (-)	
Distribution	**Clay thickness (m)**	**True**	**Measured**	**True**	**Measured**	**True**	**Measured**
Homogeneous	0	10.0	21.8	2.0E-04	3.5E-04	0.15	0.19
	5	10.0	21.8	2.0E-04	3.5E-04	0.15	0.19
Heterogeneous	0	11.6	25.3	2.0E-04	3.5E-04	0.15	0.19
	5	11.1	24.2	2.0E-04	3.5E-04	0.15	0.19

Hydraulic parameters, including hydraulic conductivity, specific storage and specific yield, are commonly estimated using aquifer tests, which represent an areal average. To account for measurement error, the aquifer test data were generated by applying random noise to the mean of the true hydraulic parameters in the reference models (Table 4.1). The aquifer test is assumed to provide information only for the sand layer but not the clay layer.

4.2.5 TEM reference model sampling

The TEM reference models were sampled in 1D using AarhusInv (Auken et al., 2015). Forward modelling was undertaken to calculate the expected voltage signals given the true σ_{bulk} values in the TEM reference models. A single-turn receiver loop with a side length of 5 m was positioned at the centre of a single-turn 25 m x 25 m transmitter loop. The transmitter system produced a 50% duty cycle transmitter square waveform at 2 amps (parameters based on Zonge

Engineering's NanoTEM system, which was selected based on its relatively fast transmitter turn-off time, making it suitable for near-surface applications such as the river loss prediction in this study). With a horizontal model extent of 500 m, 20 soundings were generated as would typically be done in the field. For each sounding, the geometric mean of the true σ_{bulk} values below the loop was calculated for each layer and used as input for the forward modelling. The layer setup is the same as the hydrogeological models (i.e. 50 layers with a uniform layer thickness of 1 m). To reflect field conditions, Gaussian random noise with a standard deviation of 5% was applied. Inversion was then performed on the modelled TEM responses to yield σ_{bulk} estimates. A vertical smoothing constraint of 0.3 was applied to improve the numerical stability and ensure the conductivity variation from layer to layer is smooth.

The true and inverted σ_{bulk} are compared in Figure 4.2, which shows an overall match with a mean absolute residual of 500 – 2400 µS/cm for the high salinity case, and 7 – 55 µS/cm for the low salinity case. However, there is a considerable discrepancy across the clay and sand boundary, which is sharp and well-defined in the reference models but blurred in the inversion due to the implicit smoothing. This caused hydraulic conductivity to be overestimated in the top few layers of sand, but as σ_{bulk} was not used to derive hydraulic conductivity for the clay layer, discrepancies in the clay layer are expected to have minimal impact.

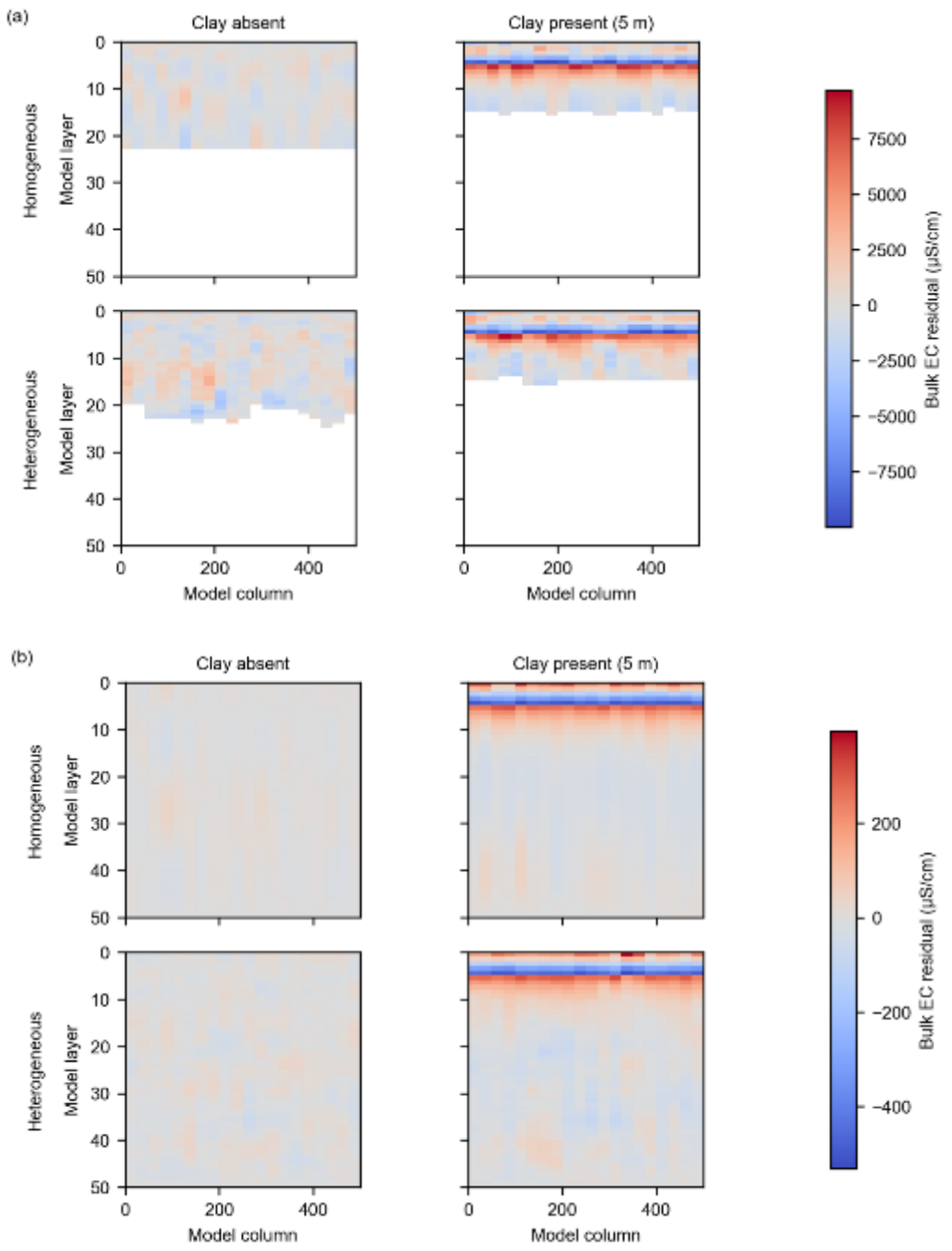

Figure 4.2 Residuals between true and inverted σ_{bulk} for (a) the high salinity case and (b) the low salinity case. Positive values indicate overestimation and negative values indicate underestimation. The blank areas in (a) illustrate the relatively shallow depth of investigation in the high salinity case.

4.2.6 SNMR reference model sampling

The SNMR reference models were also sampled in 1D using AarhusInv (Auken et al., 2015). In practice, SNMR has a considerably longer sounding time than TEM and hence is usually less spatially continuous due to fewer soundings being taken. To reflect this sampling density, only one SNMR sounding was performed at the pumping well and one at the observation well.

Forward modelling was used to estimate the expected voltage signals given the true water content and T_2* in the SNMR reference models and the true σ_{bulk} in the TEM reference models. A single-turn square coincident loop configuration with a side length of 50 m was used. To ensure the SNMR settings are physically sensible, the South Australian River Murray floodplain conditions from Li et al. (2020) were adopted, including a Larmor frequency of 2494.9 Hz, a magnetic field inclination of -66° and a declination of 0°. Time gates range between 0.05 and 0.5 s and pulse moments range between 0.1 and 20 As. To reflect field conditions, Gaussian random noise with a standard deviation of 5% was applied. Inversion was performed to convert the voltage signals from the forward modelling to water content and T_2* estimates. A vertical smoothing constraint of 0.3 was applied and the layer setup is the same as the forward model.

True and inverted T_2* and water content for the sand layer are compared in Figure 4.3 and Figure 4.4 respectively. Figure 4.3 shows an overall reasonable match for T_2*, although the match is less satisfactory at depths greater than 20 m. Figure 4.4 shows an oscillating pattern for the inverted water content, which is different from the uniform pattern of the true value, although the inverted water content is mostly centred around the true value. As the decay time of clay is too short to be detected by conventional SNMR (Walsh et al., 2011), the inverted results for the clay layer were not used in this study.

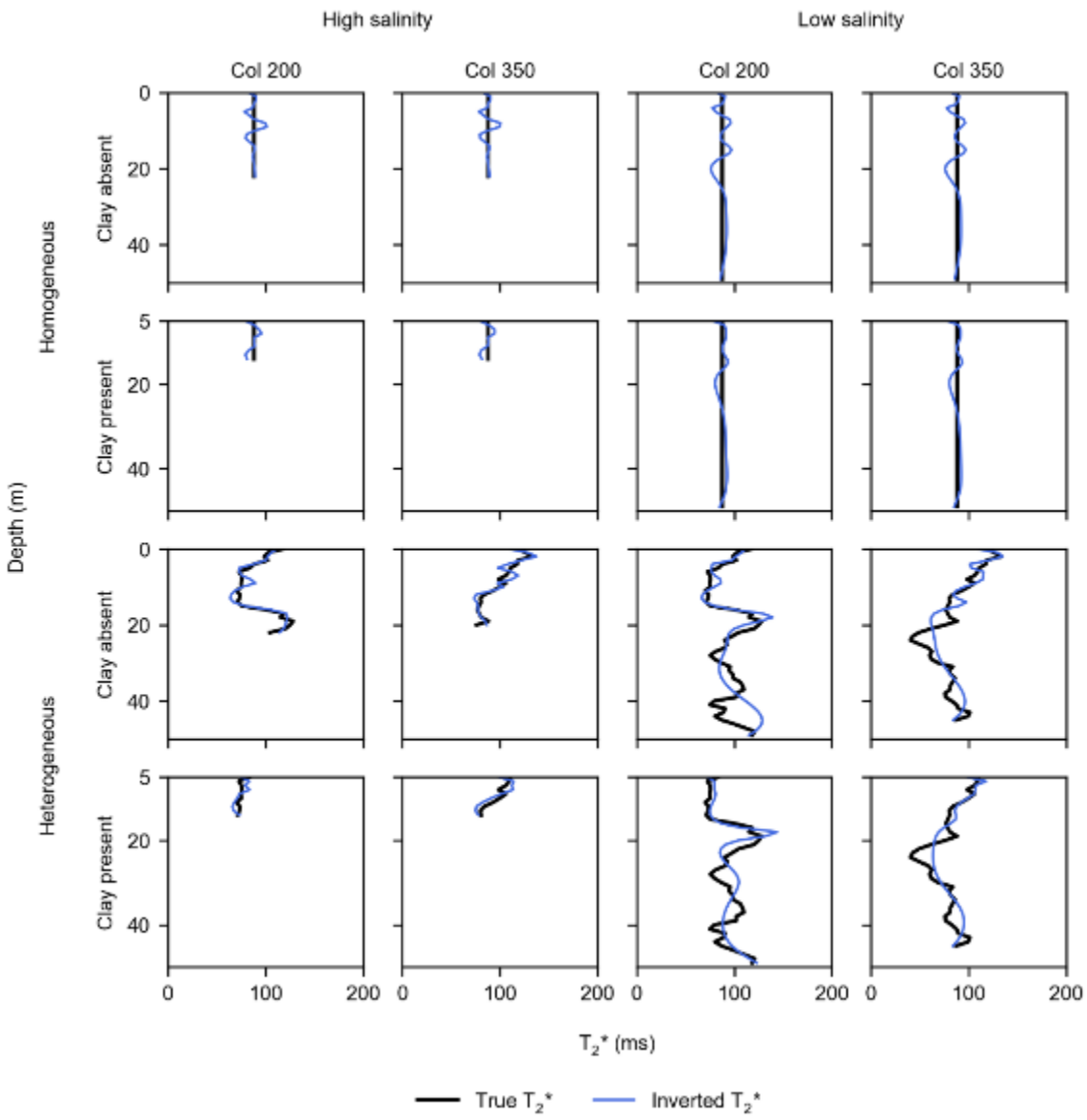

Figure 4.3 True and inverted T_2* for the sand layer at the pumping well (column 200) and observation well (column 350).

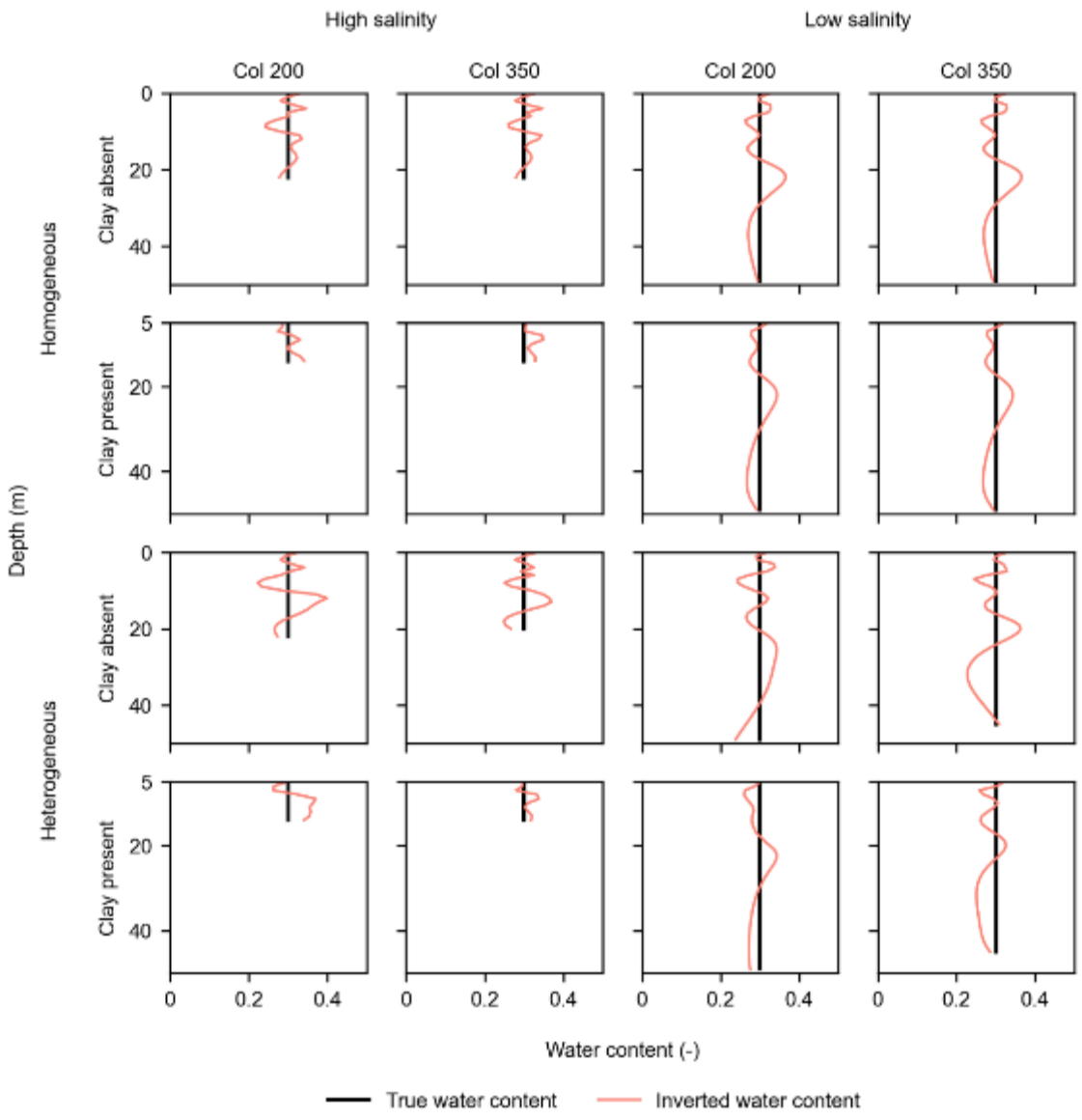

Figure 4.4 True and inverted water content for the sand layer at the pumping well (column 200) and observation well (column 350).

4.2.7 Developing ensembles of groundwater model realizations

Hydrogeological, TEM and SNMR predictive data were used in different combinations to create three ensembles of groundwater model realizations: (i) hydrogeological data only (denoted H); (ii) hydrogeological and TEM data (denoted HE); and (iii) hydrogeological, TEM and SNMR data (denoted HEN). In groundwater modelling, it is common to use a zonal parameterization approach, where a zone of uniform parameter value is used to represent part or all of a geological formation. This approach was adopted for the H ensemble with a single zone due to the lack of spatial pattern information from geophysics. Hydraulic parameters for clay were held constant with a uniform value of 1×10^{-4} m/d for hydraulic conductivity, 1×10^{-3} m^{-1} for specific storage and 0.025 for specific yield. These values are the mean calculated from a number of literature sources (Domenico and Mifflin, 1965, Domenico and Schwartz, 1998, Fetter, 2018, Todd, 1980) and are different from the true values in the reference models, which are rarely known in practice.

Groundwater model ensembles were created using Markov-Chain Monte Carlo (MCMC) with the Metropolis sampler (Gilks et al., 1995). Two individual Markov chains with 10,000 steps each were used, totalling 20,000 steps. The performance of MCMC depends on the proposal width of the Metropolis sampler, which was tuned at the beginning using 1000 iterations to optimize the acceptance rate (Roberts et al., 1997).

The MCMC approach is a Bayesian technique for sampling posterior probability distribution. In the context of this study, posterior probability represents belief of parameter distributions after calibrating the groundwater models against the groundwater level observations. Posterior probability is proportional to the product of likelihood and prior probability. Likelihood represents the probability of observing the groundwater level measurements given the proposed model parameters and was calculated as the reciprocal of the root mean square error between the measured and simulated groundwater levels. Prior probability represents our belief of parameter distributions before calibration and was mostly informed by the aquifer test data.

The prior probability settings for the sand layer are summarized in Table 4.2. Mean hydraulic parameter values were provided by the aquifer test data, while the upper and lower bounds were sourced from the literature (Domenico and Mifflin, 1965, Fetter, 2018, Frohlich et al., 1996, Heigold et al., 1979, Purvance and Andricevic, 2000). It is assumed that the difference between parameter upper and lower bounds is equal to six standard deviations of its prior probability

distribution. A log-normal distribution was used for hydraulic conductivity (Shapiro and Wilk, 1965) and a normal distribution was used for specific storage and specific yield.

For the HE ensemble, the σ_{bulk} from the TEM inversion was interpolated to each groundwater model cell. For models with a high groundwater salinity and hence shallow TEM penetration depth, the σ_{bulk} was linearly extrapolated to cover the whole groundwater model. The σ_{bulk} field was used to derive a hydraulic conductivity field (K_{TEM}) via Equation 4.4. Empirical constants α and β were proposed using a uniform distribution (Table 4.2). A prior probability was computed by comparing the mean of K_{TEM} with the prior specifications in Table 4.2.

For the HEN ensembles, as the SNMR soundings do not cover the groundwater models completely, they were mainly used to provide constraints for K_{TEM}. The empirical constant c in Equation 4.7 was computed using the mean of K_{TEM} and the water content and T_2* from the SNMR inversion, assuming m = 1. The proposed K_{TEM} field would only be accepted if the resulting empirical constant c was between 0.05 and 0.12 m s^{-3} (Knight et al., 2016).

Table 4.2 Prior Probability Settings for the Sand Layer. Std = Standard deviation.

Parameter	Mean	Std	Lower bound	Upper bound	Source(s) for the upper and lower bounds
Log hydraulic conductivity (m/d)	1.34 – 1.4	0.5	-1	2	Fetter (2018)
Empirical constant α	-	-	0	1	-
Empirical constant β	-	-	0.1	1	Frohlich et al. (1996) Heigold et al. (1979) Purvance and Andricevic (2000)
Specific storage (m^{-1})	3.5×10^{-4}	1.5×10^{-4}	1×10^{-4}	1×10^{-3}	Domenico and Mifflin (1965)
Specific yield (-)	0.19	0.042	0.1	0.35	Fetter (2018)

4.3 Results

4.3.1 MCMC diagnostics

Trace plots of hydraulic conductivity are given in Figure 4.5, which show the evolution of hydraulic conductivity over the 10,000 iterations of the two Markov chains for different hydrogeological conditions. The figure shows a reasonable change in the sampling state, where the H and HE ensembles cover most of the parameter space, while the HEN ensemble covers a narrower range due to the constraints provided by SNMR. The mean acceptance rate is 17.6%, which is slightly lower than the recommended value of 23.4% (Gelman et al., 1996) but is considered to be acceptable given the uniform priors for the empirical constants.

To determine the convergence of MCMC, the Gelman-Rubin technique was used (Gelman and Rubin, 1992). This technique is based on the notion that the Markov chains should be similar to each other if convergence has been achieved. The similarity between chains can be assessed by analysing the between-chain variance and within-chain variance. Such variances are used to calculate the potential scale reduction, a key indicator that should be as close to 1 as possible and less than 1.1. Our model ensembles yielded a potential scale reduction of 1 – 1.017, suggesting convergence was achieved.

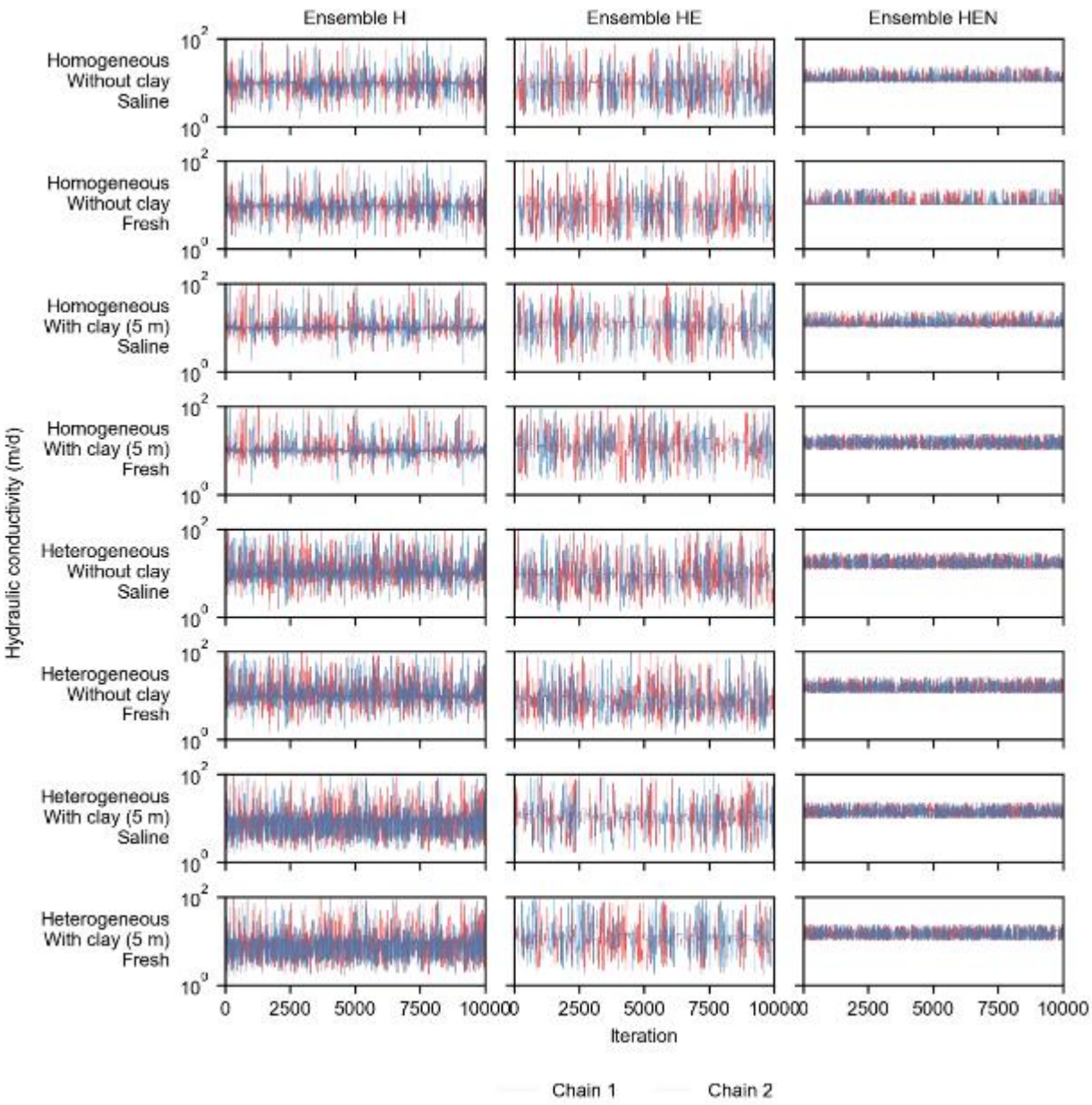

Figure 4.5 Trace plots of hydraulic conductivity showing its evolution over the 10,000 iterations of the two Markov chains for different hydrogeological conditions. The y-axis is in log-scale.

4.3.2 Posterior model parameters and predictions

The posterior distributions for river loss are shown in Figure 4.6 and summarized in Table 4.3. The prediction error was calculated using the mode, which represents the maximum likelihood. The error is relatively small for the homogeneous models, ranging between -1.9% and 1.8% with an absolute mean of 0.9%. However, the error for the heterogeneous models is considerably larger, ranging between -9.4% and 23.9% with an absolute mean of 12.6%. The heterogeneous model results suggest that including TEM alone only reduces the prediction error when the clay layer is absent (~20% error reduction), while using a combination of TEM and SNMR reduces the prediction error under all conditions by 8.7% - 54.4% with a mean of 27.6%. On average the prediction error for the heterogeneous models is increased by 112.5% due to the presence of clay and 46.4% due to the higher groundwater salinity. The standard deviation was used as an indicator of prediction uncertainty and is relatively large for the HE ensemble.

The posterior distributions for the hydraulic parameters are shown in Figure 4.6 and the statistics of hydraulic conductivity are given in Table 4.4. As the MCMC sampler pursued the maximum posterior, the hydraulic conductivity distribution was shifted from the measured value towards the true value to varying extent depending on the modelled conditions. The HEN ensemble generally has a higher hydraulic conductivity than the other ensembles due to the additional constraints provided by SNMR. Specific storage and specific yield are mostly centred around the measured value, indicating their role is relatively minor in this study.

The posterior distributions for the empirical constants α, β and c are shown in Figure 4.7. The constant α was given the widest bounds (Table 4.2), yet its posterior distribution is mostly between 0.01 and 0.2. The constant c is mostly between 0.05 and 0.1 m s^{-3} and rarely reaches the upper bound of 0.12 m s^{-3}. All constants generally show a positive skew in the heterogeneous models with varying skewness depending on the modelled conditions.

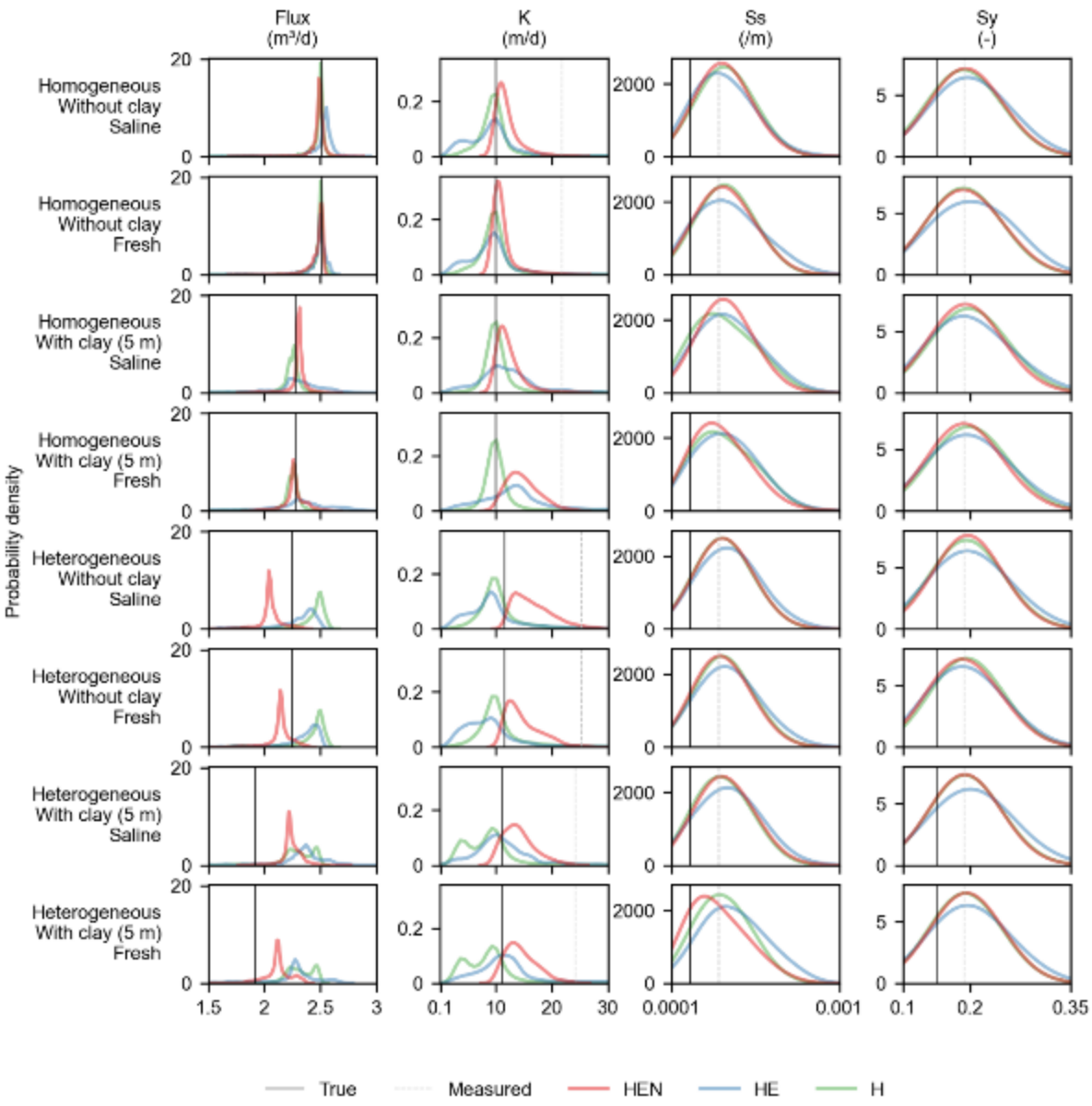

Figure 4.6 Posterior distributions for river loss and hydraulic parameters. The H ensemble uses hydrogeological data only, the HE ensemble uses hydrogeological and TEM data, and the HEN ensemble uses hydrogeological, TEM and SNMR data. Only the main portion of the x-axis range is shown to increase the visibility of the distributions.

Table 4.3 Summary Statistics for the Posterior Distributions of River Loss. Std = Standard deviation.

Reference model	Ensemble	Salinity	River loss (m^3/d)				
			True	Mean	Mode	Std	Error
Homogeneous without clay	H	-	2.51	2.47	2.50	0.12	-0.20%
	HE	Saline	2.51	2.49	2.55	0.20	1.76%
		Fresh	2.51	2.45	2.51	0.20	-0.15%
	HEN	Saline	2.51	2.48	2.49	0.07	-0.95%
		Fresh	2.51	2.46	2.53	0.09	0.61%
Homogeneous with clay	H	-	2.28	2.23	2.27	0.13	-0.64%
	HE	Saline	2.28	2.28	2.24	0.26	-1.85%
		Fresh	2.28	2.30	2.29	0.32	0.34%
	HEN	Saline	2.28	2.30	2.32	0.08	1.58%
		Fresh	2.28	2.27	2.26	0.09	-0.80%
Heterogeneous without clay	H	-	2.25	2.41	2.48	0.19	10.33%
	HE	Saline	2.25	2.27	2.44	0.26	8.53%
		Fresh	2.25	2.32	2.43	0.23	8.04%
	HEN	Saline	2.25	2.06	2.04	0.10	-9.43%
		Fresh	2.25	2.15	2.14	0.10	-4.71%
Heterogeneous with clay	H	-	1.92	2.29	2.25	0.19	17.09%
	HE	Saline	1.92	2.33	2.38	0.25	23.94%
		Fresh	1.92	2.21	2.27	0.32	18.23%
	HEN	Saline	1.92	2.24	2.22	0.08	15.59%
		Fresh	1.92	2.12	2.12	0.11	10.55%

Table 4.4 Summary Statistics for the Posterior Distribution of Hydraulic Conductivity. Std = Standard deviation.

Reference model	Ensemble	Salinity	Hydraulic conductivity (m/d)				
			True	Mean	Mode	Std	Error
Homogeneous without clay	H	-	10.0	10.0	10.0	4.8	-0.3%
	HE	Saline	10.0	10.3	10.1	8.6	0.8%
		Fresh	10.0	10.2	9.9	8.7	-0.7%
	HEN	Saline	10.0	12.0	10.7	2.1	6.7%
		Fresh	10.0	11.1	10.1	2.0	0.6%
Homogeneous with clay	H	-	10.0	10.8	9.9	5.6	-0.5%
	HE	Saline	10.0	13.8	13.5	10.4	35.4%
		Fresh	10.0	15.9	13.7	12.4	36.7%
	HEN	Saline	10.0	12.2	10.5	2.2	5.4%
		Fresh	10.0	14.8	17.9	2.8	79.4%
Heterogeneous without clay	H	-	11.6	11.6	9.6	7.8	-17.1%
	HE	Saline	11.6	11.6	9.4	11.0	-18.6%
		Fresh	11.6	9.9	9.3	9.0	-20.0%
	HEN	Saline	11.6	16.6	12.8	3.5	10.2%
		Fresh	11.6	14.8	12.9	3.1	11.5%
Heterogeneous with clay	H	-	11.1	9.2	9.6	7.2	-13.8%
	HE	Saline	11.1	12.6	9.7	9.7	-12.9%
		Fresh	11.1	14.4	12.4	11.8	12.2%
	HEN	Saline	11.1	14.1	16.9	2.8	52.3%
		Fresh	11.1	14.5	17.3	2.8	55.8%

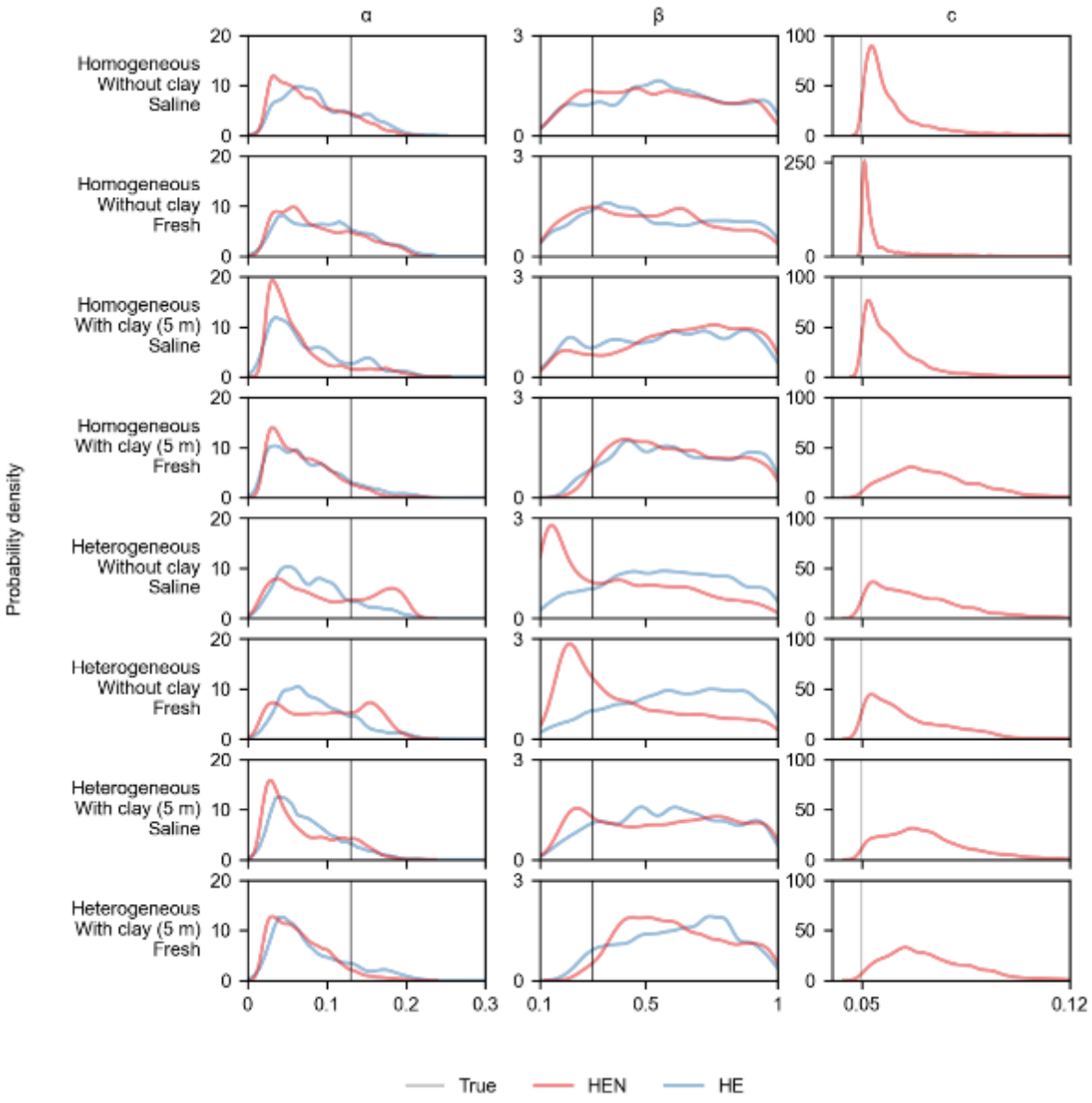

Figure 4.7 Posterior distributions for the empirical constants α, β and c. The HE ensemble uses hydrogeological and TEM data, and the HEN ensemble uses hydrogeological, TEM and SNMR data. Only the main portion of the x-axis range is shown to increase the visibility of the distributions. The plots for constant c have inconsistent y-axis range.

4.4 Discussion

For the homogeneous models, all ensembles yield a small prediction error under all conditions. This is expected for the H ensemble as drillhole and aquifer test information alone are adequate to characterize the system. However, prediction error of the HE and HEN ensembles is generally slightly greater than that of the H ensemble, possibly due to the model variability propagated from random noise introduced into the predictive geophysical data (Figure 4.2 - Figure 4.4).

In the case of the heterogeneous model, the H ensemble has a large prediction error under all conditions, due to the fact that the zonal parameterization approach is an inferior representation of the aquifer system compared to the HE and HEN ensembles, which contain more spatial information. The results indicate that using a zonal parameterization approach to represent a heterogeneous aquifer may lead to a large prediction error.

The HE ensemble results show that including TEM reduces the prediction error when clay is absent but increases the prediction error when clay is present, due to the TEM inversion smoothing across the boundary between the clay and sand layers (Figure 4.2), causing hydraulic conductivity to be overestimated in the top few layers of sand. The prediction uncertainty of the HE ensemble is relatively large compared to the other ensembles. This is mostly due to the additional uncertainty on the two empirical constants to derive hydraulic conductivity from σ_{bulk}. Compared to the HEN ensemble, the empirical constants in the HE ensemble were relatively poorly constrained using limited literature values.

The HEN ensemble indicates that using a combination of TEM and SNMR reduces the prediction error and uncertainty of groundwater models under all conditions. This is due to the additional constraints provided by SNMR for the empirical constants and hence hydraulic conductivity. The hydraulic conductivity space for the HEN ensemble was reduced dramatically by almost threefold (Figure 4.5). Consequently, the posterior distribution of hydraulic conductivity for the HEN ensemble is considerably higher than the other ensembles, resulting in a notably different river loss prediction (Figure 4.6). Results suggest that SNMR is a very important complement to TEM for groundwater modelling by providing much better constrained hydraulic conductivity estimates, reducing the prediction error and uncertainty of groundwater models.

4.5 Conclusion

This study evaluates the value of TEM and SNMR to derive additional hydraulic conductivity constraints for groundwater modelling in a sedimentary setting. Ensembles of groundwater models generated with a combination of hydrogeological and geophysical parameters suggest that for homogeneous aquifers, the inclusion of TEM and SNMR data does not necessarily improve the groundwater model performance due to the propagation of geophysical uncertainties to the groundwater models. A simple aquifer test with sparse observation wells characterize the whole groundwater system, as would be expected. However, for the more realistic heterogeneous aquifer scenario, a zonal parameterization approach for groundwater modelling from a single aquifer test and sparse observation wells results in a large predictive error for groundwater discharge. Adding dense transects or arrays of TEM data to derive spatial sub-surface maps of hydraulic conductivity does not necessarily improve the predictive groundwater models. This is due to a poorly constrained petrophysical relationship between modelled bulk electrical and hydraulic conductivities, as well as over- and under-estimation of true bulk electrical conductivity implicit in model smoothing. However, including even a few sparse sets of SNMR data, which provides better constraints on the empirical relationship between electrical and hydraulic conductivity, greatly reduces the prediction error and uncertainty of groundwater models. This method of coupling TEM and SNMR with groundwater modelling can be particularly useful in areas with limited aquifer test data.

Acknowledgements

This research is supported by an Australian Government Research Training Program (RTP) Scholarship through the University of Adelaide of South Australia and a CSIRO Research Plus scholarship. We would like to thank Brady Flinchum, Luk Peeters and Chris Turnadge for their technical advice.

5 Constraining regional-scale groundwater transport predictions with multiple geophysical techniques

Chris Li[a, b]

Rebecca Doble[a]

Michael Hatch[b]

Graham Heinson[b]

Ben Kay[b]

[a] CSIRO Land and Water, Glen Osmond, South Australia, Australia

[b] The University of Adelaide, Adelaide, South Australia, Australia

Submitted to *Journal of Hydrology* in August 2020

Statement of Authorship

Title of Paper	Constraining regional-scale groundwater transport predictions with multiple geophysical techniques
Publication Status	Submitted for Publication
Publication Details	In review with the *Journal of Hydrology* (submitted 20 Aug 2020)

Principal Author

Name of Principal Author (Candidate)	Ho Yin Li (Chris)		
Contribution to the Paper	Conception and design Analysis and interpretation of data Writing the manuscript		
Overall percentage (%)	90		
Certification:	This paper reports on original research I conducted during the period of my Higher Degree by Research candidature and is not subject to any obligations or contractual agreements with a third party that would constrain its inclusion in this thesis. I am the primary author of this paper.		
Signature		Date	20 August 2020

Co-Author Contributions

By signing the Statement of Authorship, each author certifies that:

i. the candidate's stated contribution to the publication is accurate (as detailed above);

ii. permission is granted for the candidate in include the publication in the thesis; and

iii. the sum of all co-author contributions is equal to 100% less the candidate's stated contribution.

Name of Co-Author	Rebecca Doble		
Contribution to the Paper	Conception and design Critically revising the manuscript		
Signature		Date	20 August 2020

Name of Co-Author	Michael Hatch		
Contribution to the Paper	Conception and design Collection and analysis of data Critically revising the manuscript		
Signature		Date	20 August 2020

Name of Co-Author	Graham Heinson		
Contribution to the Paper	Conception and design Critically revising the manuscript		
Signature		Date	20 August 2020

Name of Co-Author	Ben Kay		
Contribution to the Paper	Collection and analysis of data		
Signature		Date	20 August 2020

Abstract

Geophysics is commonly used to complement groundwater models due to its denser spatial coverage, but the coupling is usually performed in a deterministic manner and the uncertainty of geophysical data is rarely incorporated. This study demonstrates how multiple geophysical techniques of Audio-frequency Magnetotellurics (AMT), Time-domain Electromagnetics (TEM) and Nuclear Magnetic Resonance (NMR), along with scattered and sparse hydrological measurements, can be coupled with stochastic groundwater models. These geophysical techniques provide constraints on hydraulic conductivity, water table depth, hydrostratigraphy and porosity. The challenge of coupling geophysics with groundwater modeling is that geophysical techniques rarely provide direct quantification of hydrogeological properties. When using geophysical data as targets in groundwater model inversion, it is critical to quantify and account for their uncertainty to avoid incorrectly biasing model outcomes. This study shows how this can be achieved using the ensemble-smoother method via PESTPP-IES. Observation uncertainty can be expressed as a prior variance and used to form a random observation ensemble, allowing the inversion to fit to the observation distribution instead of the observation itself. In addition, the ensemble-smoother method produces an ensemble of calibrated models that can be considered to represent the posterior distribution of parameters and predictions, which can be readily used for non-linear uncertainty analysis and probabilistic predictions. This approach is illustrated using the geophysical and hydrological data from Kapunda, South Australia, to evaluate the impact of a simulated In-Situ Recovery (ISR) copper mining operation.

5.1 Introduction

Numerical modelling is useful for informing management decisions about groundwater resources (Hunt and Zheng, 2012). However, the effectiveness of groundwater models is hampered by various sources of uncertainty, including data, conceptualization and parameterization (Doherty and Simmons, 2013). This is partly because groundwater models generally require spatially continuous data, while most classical hydrogeological techniques provide point-scale information (Brunner et al., 2006). This mismatch can be mitigated by complementing groundwater models with geophysics due to its denser spatial coverage (relatively to drillhole-based hydrogeological techniques), non-invasiveness and relatively low cost on an areal basis (Slater, 2007).

Audio-frequency Magnetotellurics (AMT) and Time-domain Electromagnetics (TEM) are electromagnetic methods that estimate subsurface electrical resistivity, which is related to groundwater salinity, sediment texture, mineralogy and degree of saturation (Everett, 2013). Nuclear Magnetic Resonance (NMR) is a geophysical technique that detects subsurface water directly and provides information on pore size distribution and water content, the latter of which is a proxy for porosity in the saturated zone (Legchenko et al., 2002). These geophysical techniques have proven useful in previous studies for constraining important components of groundwater models, including conceptualizations, geological framework and hydraulic properties. For example, Wagner (2007) used AMT to determine the freshwater-saltwater transition zone under Amchitka Island to model the transport of subsurface radioactive materials to the sea floor. Marker et al. (2015) used TEM to improve the hydrostratigraphic characterization for a hydrological model to estimate groundwater levels in Norsminde, Denmark. Boucher et al. (2012) used NMR to estimate transmissivity and specific yield for a groundwater model to assess recharge to a sandstone aquifer in Niger. However, these studies only coupled geophysics with groundwater modelling in a deterministic manner, where a single, best-calibrated groundwater model was developed and used to make predictions. In addition, the uncertainty inherent in geophysical data was rarely quantified and accounted for in groundwater model inversion.

For groundwater model inversion, the Gauss-Levenberg-Marquardt (GLM) algorithm (Hanke, 1997) is commonly used for parameter estimation and uncertainty analysis via programs such as PEST (Doherty et al., 1994), PESTPP (Welter et al., 2015) and UCODE (Poeter et al., 2014). The GLM algorithm requires a sensitivity matrix known as the Jacobian matrix, which is commonly constructed using a finite-difference approach. An alternative approach was proposed by White

(2018), who implemented the ensemble-smoother form of the GLM algorithm from Chen and Oliver (2013) into the PESTPP suite, referred to as PESTPP-IES. The ensemble-smoother method derives the Jacobian matrix empirically from an ensemble of random parameter values (White, 2018), which has several advantages. Firstly, it produces an ensemble of calibrated models that can be considered to represent the posterior distribution of parameters and predictions, which can be readily used for non-linear uncertainty analysis and probabilistic predictions. In addition, observation uncertainty can be expressed as a prior variance and used to form a random observation ensemble, allowing the inversion to fit to the observation distribution instead of the observation itself. Furthermore, the ensemble-smoother method decouples the number of parameters being estimated from the number of model runs required, greatly reducing the computational time needed for highly parameterized models (White, 2018).

The objective of this paper is to couple multiple geophysical techniques of AMT, TEM and NMR with stochastic groundwater modelling using the ensemble-smoother framework. We demonstrate how this framework can be used as a data assimilation tool to facilitate the flow of information from geophysical and hydrogeological data to the groundwater model prediction of interest. We also show how the uncertainty of geophysical data can be expressed in a manner that is relevant for groundwater model inversion. This modelling framework was applied in the context of an In-Situ Recovery (ISR) copper mining operation, which involves injecting lixiviant into the ground to dissolve and extract minerals through a system of injection and extraction wells (Sinclair and Thompson, 2015). The model ensemble was used to predict the regional-scale hydrological impact of a hypothetical ISR trial operation, the results of which are presented in a probabilistic manner.

5.2 Methods

5.2.1 Site descriptions

The historical Kapunda copper mine is located approximately 80 km north east of Adelaide, South Australia (Figure 5.1). The region has a semi-arid climate with a mean annual rainfall of 490 mm/y and evaporation of 1800 mm/y (Bureau of Meteorology, 2020). Established in 1842, Kapunda was the first mining town in Australia and its open-pit mine was a key economic driver for the whole continent until its closure in 1879 (Nirola et al., 2016). The remnant low-grade copper surrounding the mine was considered to be sub-economic, and the mine has since been developed into a heritage site and tourist attraction (Bogenes et al., 2003). With the recent advances in ISR (Sinclair and Thompson, 2015), the feasibility of recovering the remnant copper is under consideration again.

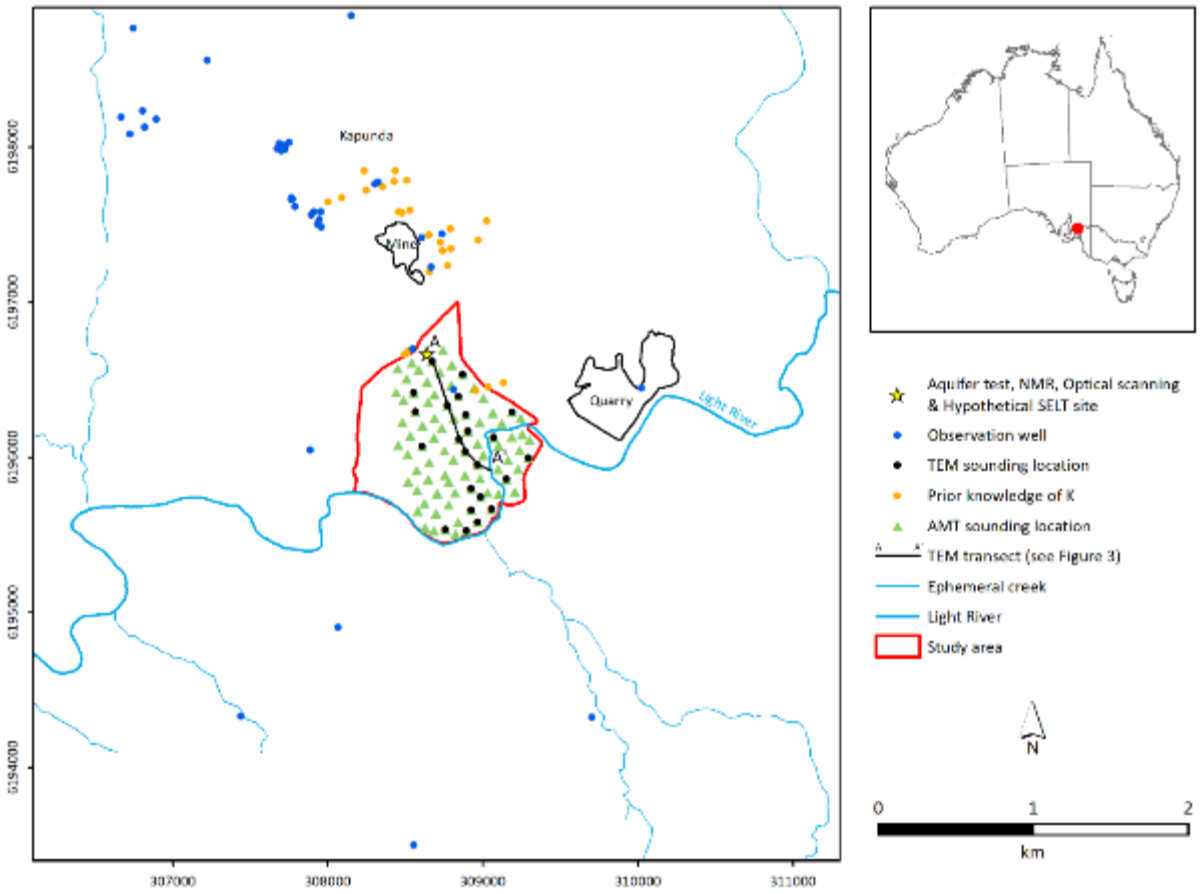

Figure 5.1 Kapunda site map, with spatial extent of the groundwater model domain.

The proponent is developing a Site Environmental Lixiviant Test (SELT), which is a small-scale operation using a limited number of injection and extraction wells to test various recovery options. The SELT operation is planned to be followed by a remediation phase, where the remaining injectant is retrieved using the extraction well. From a management perspective, the key hydrological issues of concern are: (1) the flow paths of the injectant and whether it will reach the Light River (Figure 5.1), an important environmental asset; and (2) the residence time of the injectant in the aquifer. This study demonstrates how these questions can be addressed by using a combination of multiple geophysical techniques and stochastic groundwater modelling.

5.2.2 Hydrogeological data

Kapunda is located within the Adelaide Geosyncline, a major geological province in central South Australia. The local geology is dominated by Neoproterozoic aged formations (Lambert et al., 1980). The main geological formations in the study area include the Tapley Hill Formation to the north, which covers the hypothetical SELT site, and the Brighton Limestone to the south. The Tapley Hill Formation primarily consists of blue-grey laminated siltstone and slate, while the Brighton Limestone is typically characterized by coarse-grained and recrystallized marble units (Akker and Watson, 2017). From a hydrogeological perspective, these formations behave as an interconnected fractured rock aquifer, the hydraulic behaviour of which is largely governed by the secondary porosity developed from fracturing (Jeuken and Magarey, 2017).

A total of 42 observations wells were used in this study (Figure 5.1), most of which only have a single groundwater level reading, often collected in the 1970s. There are no metered groundwater usage data in Kapunda. As groundwater EC is relatively high in Kapunda, ranging between 1900 and 22,000 µS/cm with a mean of 5800 µS/cm (~3300 mg/L total dissolved solids), groundwater usage is assumed to be negligible.

Hydraulic conductivity was estimated from well yield and draw-down data using Logan Approximation (Logan, 1964) by Jeuken and Magarey (2017). This approach provided 28 estimates of hydraulic conductivity (Figure 5.1) ranging between 0.0007 and 0.4 m/d, with a geometric mean of 0.04 m/d. The error of this method is likely to be in the order of ±50% (Logan, 1964). In addition, a 9-hour aquifer test was performed in February 2020 in the northern part of the study area (Figure 5.1) and reported a hydraulic conductivity of 0.07 m/d. Effective porosity was estimated to be 1% near the aquifer test site based on fracture logging using a downhole optical scanner to ~65 m depth and assuming 50% cementation (Jeuken and Magarey, 2017).

An initial assessment of groundwater recharge was undertaken using the chloride mass balance method (Wood, 1999). This technique assumes 1D vertical advective flow only and no chloride derived from flow upgradient of the bores. The chloride mass balance equation is as follows:

$$\text{Recharge} = \frac{\text{Rainfall} \times \text{Cl}_{\text{Rainfall}}}{\text{Cl}_{\text{Groundwater}}} \quad 5.1$$

where Cl is chloride concentration (mg/L). In Kapunda, the average chloride concentration is ~9 mg/L in rainfall (Davies and Crosbie, 2018) and ~1100 mg/L in groundwater according to the observation well data. Based on this analysis, the long-term average recharge rate is ~4 mm/y, which is ~0.8% of rainfall. Note that this method estimates net recharge, which already accounts for groundwater evapotranspiration.

The regional groundwater sink is the Light River. Lamontagne et al. (2020) applied various environmental tracers, including δD and δ^{18}O of water, EC, chloride and radon-222, to evaluate the surface water – groundwater connectivity of the Light River. They estimated baseflow to the Light River within our study area in 2019 to be in the order of 400 – 3000 m³/d. They also identified a zone of higher groundwater discharge in the eastern part of our study area (i.e. upstream of A' in Figure 5.1).

5.2.3 Geophysical data

5.2.3.1 Audio-frequency Magnetotellurics

AMT is an electromagnetic method that uses naturally-occurring, passive electromagnetic field sources, such as global lightning strikes, to map geological structures (Garcia and Jones, 2002). Time-varying magnetic fields induce electrical currents into the earth that can be measured using grounded dipoles and magnetic field antennas over a wide range of frequencies (Vozoff, 1991). The received signal is used to estimate ground electrical resistivity and the depth of investigation is generally in kilometres (Spies, 1989).

As part of this study, a broadband, audio frequency magnetotellurics (AMT) survey was undertaken in April 2019 on a grid of 87 sites with a nominal spacing of 100 m (Figure 5.1). Data were recorded at each site for about 20 hours using the Phoenix MTU-5A systems, yielding good quality AMT responses in the bandwidth of 1 to 10,000 Hz.

The collected AMT data were inverted in 3D using ModEM (Kelbert et al., 2014). The model consists of 100 cells in the east-west direction and 120 cells in the north-south direction with a minimum cell dimension of 12 m. The vertical dimension was discretised into 120 layers with a

minimum thickness of 5 m, increasing at a rate of 2% with depth. Impedance error floors were set to 7% for all components. The inversion included 26 frequencies, spread evenly from 0.001 to 100 Hz with five estimates per decade. The model roughness was set with a tau of 0.1 and no weighting was applied for either horizontal or vertical smoothing. The model misfit with the data has a root mean square error (RMSE) of 1.9.

The electrical conductivity (EC) estimates from the 3D inversion at 50 and 100 m depth are shown in Figure 5.2. The 50 m depth slice shows two distinctly different zones in the study area. The more conductive zone to the north is interpreted to be related to the Tapley Hill Formation, while the more resistive zone to the south is interpreted to be related to the Brighton Limestone. The 100 m depth slice indicates that EC generally decreases with depth. In addition, phase tensor analysis of the high frequency AMT data suggests that the top 100 m of the fractured rock aquifer is electrically isotropic over the survey area, possibly due to deep-weathering of the existing bedrock fabric.

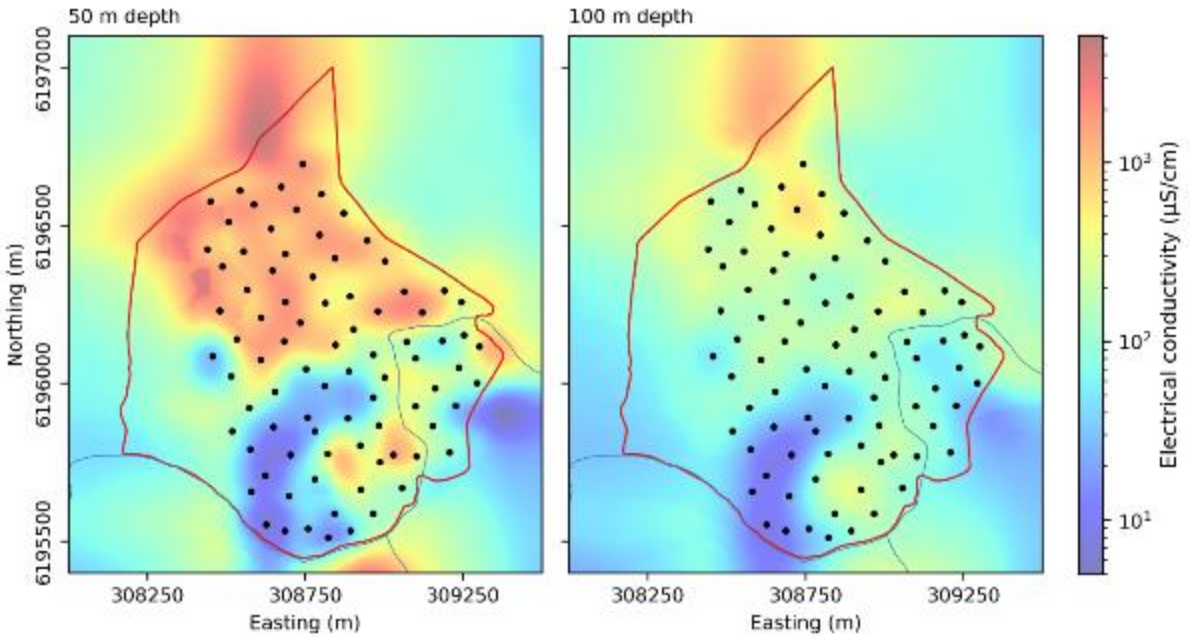

Figure 5.2 EC depth slice of the inverted AMT data at 50 and 100 m depth. The black dots denote AMT stations, the red line denotes the study area and the blue lines denote rivers and creeks.

The EC estimates from the inverted AMT data can also be used to provide information on hydraulic conductivity via the following petrophysical relationship (Purvance and Andricevic, 2000):

$$\mathrm{EC} = \mathrm{a}\mathrm{K}^{\mathrm{b}} \qquad 5.2$$

where K is hydraulic conductivity (m/d), and a and b are empirical constants, which were calibrated using data from the aquifer test and the closest AMT station. With a hydraulic conductivity of 0.07 m/d (Section 5.2.2) and a geometric EC mean of ~520 µS/cm, it was estimated that a = 950 and b = 0.23.

5.2.3.2 Time-domain Electromagnetics

TEM involves applying a direct current to a transmitter loop and then shutting the current off abruptly (Everett, 2013). This produces a time-varying magnetic field into the earth, subsequently generating eddy currents in subsurface conductors. Such eddy currents create a secondary magnetic field that is measured by a receiver loop. The decay rate of the secondary magnetic field is directly related to ground electrical resistivity (Everett, 2013). Compared to AMT, TEM generally has a shallower depth of investigation but a finer resolution at the near-surface (Spies, 1989).

A TEM survey was conducted in May 2019 at 85 sites with a nominal spacing of 100 m (note that not all the TEM soundings were used for groundwater modelling, as explained below). The TEM sites were chosen to be as close to the AMT sites as possible. The soundings were collected using the Zonge Engineering NanoTEM system. This system has fast transmitter turn-off and sampling rate to collect near-surface data down to ~80 m depth in our study area. A central loop configuration was used where a single-turn 5 m × 5 m receiver loop was placed at the centre of a single-turn 20 m × 20 m transmitter loop. The transmitter was set to 2 amps and powered by a 12 V battery. Three data stacks were collected at each station using a repetition rate of 64 Hz and sampling period of 1.6 µS. The collected TEM data were processed to remove noisy late time data and then inverted in 1D using AarhusInv (Auken et al., 2015) as a smooth 20-layer model.

A transect of the inverted TEM data is shown in Figure 5.3. The south-eastern side of the transect (i.e. near A') shows a thin layer with moderate EC near the surface, probably representing the unsaturated zone. It is then followed by a highly conductive layer, possibly indicating the weathered part of the saturated zone with relatively high porosity and groundwater salinity. It then gradually transitions into a more resistive layer, potentially representing the unweathered

part of the saturated zone with low porosity. This layering conceptualization is believed to be applicable throughout Kapunda, although the unweathered layer may extend to greater depths in other parts of the area (Figure 5.2 and Figure 5.3).

Given the relative shallowness and high salinity of groundwater in the survey area, the water table is expected to be detectable in the TEM data as an EC high. Therefore, the EC peak of the TEM soundings was used as an indicator of water table depth. Due to a paucity of groundwater level observations for ground-truthing, a quality assurance process was performed on the water table estimates using a pseudo-Bayesian approach, where our prior knowledge is based on a potentiometric surface developed using groundwater level observations and water levels of the Light River. Given the absence of groundwater-affecting activities (e.g. pumping) in the survey area, the potentiometric surface is assumed to be a reasonable approximation of the system. Therefore, only the groundwater levels derived from TEM that are within ±2 m of our prior knowledge, totalling 23 estimates (Figure 5.1), were used in the groundwater model inversion.

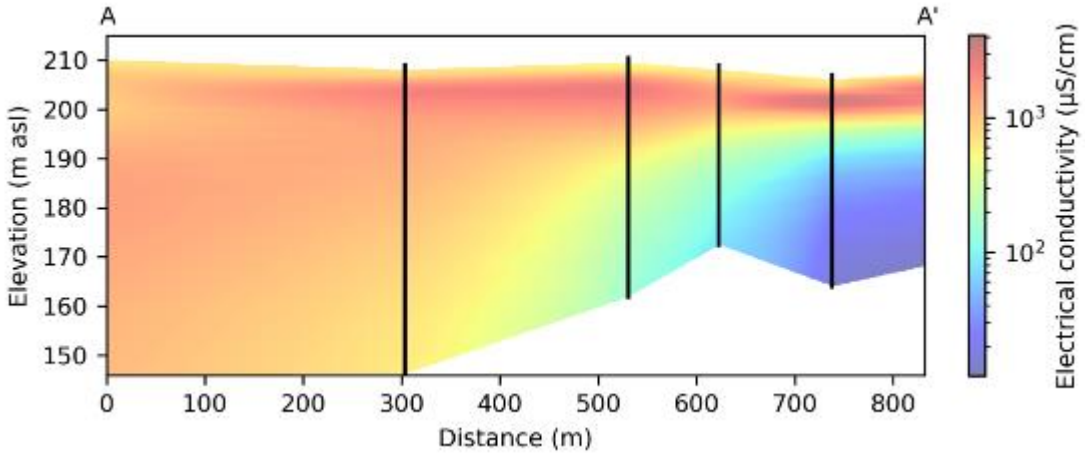

Figure 5.3 A transect of the inverted TEM data. The transect location is shown in Figure 5.1. The black lines denote TEM stations, and asl stands for above sea level.

5.2.3.3 Nuclear Magnetic Resonance

NMR, also known as Magnetic Resonance Sounding (MRS), is a geophysical technique that exploits the quantum physical properties of hydrogen protons in subsurface water to gain hydrogeological information (Legchenko et al., 2002). The initial amplitude of the received signal is directly related to water content, which is a proxy for porosity in the saturated zone. In

addition, a decay time constant T_2 is estimated from the decay pattern of the received signal, which provides information about pore size distribution (Behroozmand et al., 2015).

Borehole NMR data were collected in the northern part of the study area (Figure 5.1) using Vista Clara's Javelin system equipped with a JPY 350 probe (88.9 mm in diameter) to ~28 m depth. The Carr-Purcell-Meiboom-Gill (CPMG) pulse sequence was used (Carr and Purcell, 1954, Meiboom and Gill, 1958). The collected NMR data were processed and inverted using Vista Clara's Javelin Pro Plus program.

The decay time constant T_2 and total water content from the NMR inversion below the water table are shown in Figure 5.4. Note that the total water content includes both connected and isolated pores, and it is the former that contributes to groundwater flow. Therefore, the total water content was separated into water content in small, moderate and large pores using T_2 cut-off times of 3 and 33 ms (Behroozmand et al., 2015). We assume groundwater flows primarily in larger pores, hence the water content in large pores was used as a proxy for effective porosity. However, the water content in large pores below ~17 m depth appears to be affected by some localized features that may not be regionally representative (Figure 5.4) and hence was excluded from the analysis. The remaining data indicate a mean effective porosity of 5.6%. This is considerably higher than the value of 1% as suggested by optical scanning, but is consistent with Akker and Watson (2017) who reported an effective porosity of 5% for the same Tapley Hill Formation, but approximately 80 km south of the study area. The uncertainty in effective porosity is explored further in the groundwater model inversion.

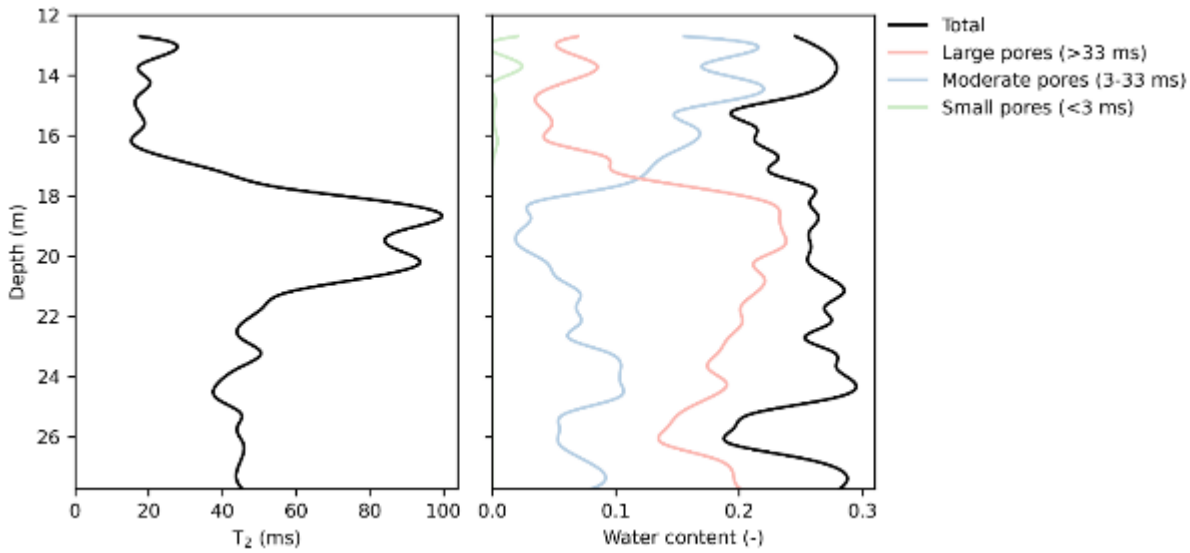

Figure 5.4 Profiles of the decay time constant T_2 (left) and water content (right) from the NMR inversion. The water content in large pores is assumed to be a proxy for effective porosity.

5.2.4 Groundwater modelling

5.2.4.1 Model development

Due to the lack of detailed fracture data at a regional scale in Kapunda, the fractured rock aquifer was simulated using the equivalent porous medium approach (Long et al., 1982). A 3D regional-scale numerical groundwater model was developed using MODFLOW-Unstructured Grid (USG) (Panday et al., 2017). The model domain is 5.5 km × 5.2 km in area and the model edges were set ~2 km away from the study area to avoid boundary effects (Figure 5.1). The Voronoi grid was generated using AlgoMesh (Merrick, 2016) with a nominal cell size of 10 m² in the study area and up to ~25,000 m² in the regional area. The same grid was applied to two layers, resulting in a total of 294,356 cells.

The top layer of the model represents the more permeable, weathered part of the fractured rock aquifer, while the bottom layer represents the less permeable, unweathered part of the aquifer. The top model surface was sourced from the DEM that has a resolution of 5 m × 5 m. The thickness of the weathered layer was estimated using the AMT data, where the EC sounding at each station was divided into two layers using the K-means clustering technique (Jain, 2010), assuming electrical and hydraulic properties are related. These thickness estimates were interpolated within the AMT survey area and extrapolated to their geometric mean of ~100 m outside the survey area. A constant thickness of 100 m was applied to the bottom layer, allowing all observation wells to be included in the model.

The Light River and other ephemeral creeks were simulated using MODFLOW's RIV package (Panday et al., 2017). Time-varying river depths were used for the Light River based on data from the nearest gauging station. The local ephemeral creeks are usually dry except for the wetter winter months, hence their river depth was set to 0 m (i.e. river stage equals riverbed elevation). River bathymetry was sourced from the DEM. Riverbed conductance was mostly set to 0.1 m²/d based on the regional hydraulic conductivity (Section 5.2.2), except for the eastern part of the Light River in the study area where a higher conductance of 10 m²/d was applied, as this reach was identified to be a zone of higher groundwater discharge (Lamontagne et al., 2020). The historical mine and quarry were represented as groundwater discharge features using MODFLOW's DRN package (Panday et al., 2017). The drain elevation was sourced from the DEM and the drain conductance was set to 0.1 m²/d. The regional lateral groundwater inflows from the northern and southern sides were modelled in both layers using MODFLOW's GHB package

(Panday et al., 2017). The head values were derived from groundwater level observations and the conductance was set to 0.1 m^2/d.

Net groundwater recharge was simulated using MODFLOW's RCH package (Panday et al., 2017). Annually-varying rainfall data were incorporated into the model as recharge multipliers, which were multiplied with the spatially-varying rainfall-to-recharge ratios (a calibration parameter) to derive net recharge. Groundwater evapotranspiration is not explicitly included in the model as it is already accounted for in net recharge. Given the relatively high groundwater salinity in Kapunda (Section 5.2.2), groundwater extraction is assumed to be negligible and hence not simulated in the model.

The model consists of 53 stress periods. The first period is steady-state and represents the pre-1970 period, which was selected based on the observation data availability. This stress period provides the initial conditions for the subsequent 50 transient annual stress periods, which represent the time period between 1970 and 2019 and were used for history-matching. The last two stress periods represent the hypothetical SELT operation and remediation phase, with a duration of two months and three years respectively. All transient stress periods have 10 time steps and a time step multiplier of 1.2.

The hypothetical SELT operation consists of four injection wells, separated by 20 m, and one extraction well at the centre. The operation rate is 0.02 L/s for each injection well and 0.1 L/s for the extraction well. During the remediation phase, the extraction well continues to operate at the same rate of 0.1 L/s while all the injection wells are switched off.

Transport of the injectant was simulated using the particle-tracking code mod-PATH3DU (Craig et al., 2020). The only transport mechanism modelled is advection, while processes such as dispersion, chemical reaction and sorption are considered beyond the scope of this study. A circle of 12 particles, representing the injectant, were placed around each injection well and released at the commencement of the SELT operation. The model was set to extend the tracking time beyond the end of simulation time by using the flow field from the last time step.

5.2.4.2 Model inversion

Groundwater model inversion was performed using the ensemble-smoother method via PESTPP-IES (White, 2018). A brief description of the ensemble-smoother method is provided here and readers are referred to White (2018) and Chen and Oliver (2013) for further details.

The ensemble-smoother method reformulates the GLM algorithm by empirically deriving the Jacobian matrix from an ensemble of random parameter values (Chen and Oliver, 2013):

$$\Delta_\theta = -\left(\left(J_{emp}^T \Sigma_\varepsilon^{-1} J_{emp}\right) + (1+\lambda)\Sigma_\theta^{-1}\right)^{-1}\left(\Sigma_\theta^{-1}(\Theta - \Theta_0) + J_{emp}^T(D_{sim} - D_{obs})\right) \quad 5.3$$

where

$$J_{emp} \approx \Sigma_\varepsilon^{\frac{1}{2}} \Delta_{sim} \Delta_{par}^{-1} \Sigma_\theta^{-\frac{1}{2}} \quad 5.4$$

$$\Delta_{sim} = \frac{\Sigma_\varepsilon^{-\frac{1}{2}}(D_{sim} \ominus \overline{D}_{sim})}{\sqrt{N_e - 1}} \quad 5.5$$

$$\Delta_{par} = \frac{\Sigma_\theta^{-\frac{1}{2}}(\Theta \ominus \overline{\Theta})}{\sqrt{N_e - 1}} \quad 5.6$$

where Δ_θ is the parameter upgrade matrix, J_{emp} is the empirically-derived Jacobian matrix, Σ_ε is the observation noise covariance matrix, Σ_θ is the prior parameter covariance matrix, λ is the Marquardt dampening parameter, Θ and Θ_0 are the current and initial parameter vector respectively, D_{obs} and D_{sim} are the observation and simulated-equivalent ensembles respectively, $\overline{D}_{sim}$ and $\overline{\Theta}$ are the mean of the simulated-equivalents to observations and parameters across their respective ensembles respectively, N_e is the number of realizations, and $\ominus$ denotes broadcast subtraction.

In this study, the ensemble size was initially set to 105 realizations to account for situations where some realizations may fail to converge. The dampening of the parameter upgrade factor is controlled by λ (Equation 5.3), where a high value of λ leads to rapid improvement in the objective function, while a low value of λ is better at navigating the objective function space. The optimal value for λ is automatically estimated for each inversion iteration through a trial-and-error procedure based on a subset of the parameter ensemble (the whole ensemble is not used to reduce computational time). In this study, the inversion was converged after 9 iterations based on the following termination criteria: (1) if the relative decrease in the mean objective function was less than 1% over 3 iterations, or (2) if there was no reduction in the mean objective function for 3 iterations. The top 100 realizations with the smallest objective function were used to form the final ensemble.

The inversion workflow in this study is illustrated in Figure 5.5. The modelled hydraulic conductivity was compared with our prior knowledge, including the aquifer test and Logan Approximation estimates. In addition, to provide more constraints in the study area, the modelled hydraulic conductivity was compared with the AMT data. This was achieved by converting the hydraulic conductivity field to an EC field using 5.2 and the empirical constants estimated in Section 5.2.3.1. The empirical constants are assumed to be spatially uniform due to the limited aquifer test data. Given the uncertainty in the petrophysical relationship, the AMT data were aggregated into five zones using the K-means clustering technique (Jain, 2010). The EC comparison was only undertaken for the weathered layer as the unweathered layer possesses a different electrical property (Figure 5.2 and Figure 5.3) where the estimated empirical constants may not apply.

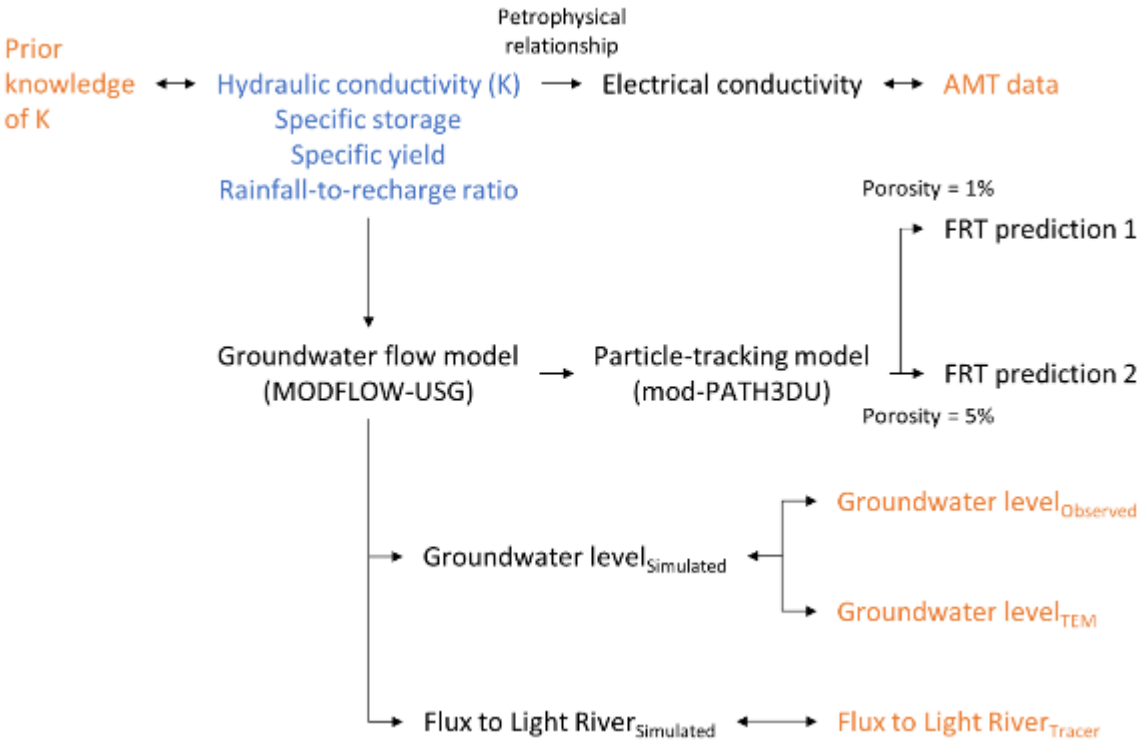

Figure 5.5 Inversion workflow in this study. Parameter groups that were varied during the inversion are in blue colour, observation groups that were used as inversion targets to compute the objective function are in orange colour. Due to the uncertainty in effective porosity and the lack of inversion targets, two separate particle-tracking runs were undertaken with different uniform effective porosity values of 1% and 5%. Each double arrow denotes a residual calculation.

Groundwater levels computed by the flow model were compared with groundwater levels from the observation wells and TEM. In addition, the simulated groundwater flux to the Light River within the study area in 2019 was compared with the mean of tracer estimates from Lamontagne et al. (2020).

Due to the lack of inversion targets, effective porosity was not included as a calibration parameter. To address its uncertainty, two separate particle-tracking runs were undertaken with different uniform effective porosity values of 1% and 5%, which are considered to represent the lower and upper bounds respectively.

Pilot points, a method for spatial parameterisation, were used for all parameter groups (Doherty, 2003). Given the fractured rock environment, pilot points were placed at each observation to capture the local heterogeneity. In addition, gaps in the pilot point coverage were filled using a maximum separation distance of 25 m in the study area and 250 m elsewhere in the weathered layer, and 500 m in the unweathered layer. This resulted in 1397 pilot points in the weathered layer and 103 pilot points in the unweathered layer for each corresponding parameter group. Spatial correlation between the pilot points were defined using an exponential variogram, with nugget = 0, sill = 1 and a = 1100, where "a" describes the decay rate of spatial correlation with distance and was set to ~20% of the model extent.

The calibration parameters are detailed in Table 5.1. All parameters were log-transformed during the inversion. The prior parameter variance was calculated based on the assumption that the difference between the upper and lower bound of a parameter group is equal to four standard deviations of its prior probability distribution (White, 2018). Based on the AMT data, horizontal hydraulic conductivity is assumed to be isotropic (i.e. $K_x = K_y$). A similar assumption was adopted for vertical hydraulic conductivity (i.e. $K_{horizontal} = K_{vertical}$). The effect of this assumption is expected to be small given the relatively low permeability of the unweathered layer and therefore the already dominant lateral flow. Hydraulic conductivity of the unweathered layer was forced to be at least an order of magnitude lower than the hydraulic conductivity of the weathered layer. The storage parameter settings are based on the aquifer tests in the adjacent Barossa region (~30 km away) that has a similar hydrogeological setting (Li and Cranswick, 2016). Specific storage was predominately used for the bottom layer, which is confined, and for simplicity the same values were applied to the top layer (vice versa for specific yield). The rainfall-to-recharge ratios vary spatially but were fixed with time for parsimony reasons.

Table 5.1 Inversion settings for the parameter groups. The initial and bound parameter values are before log-transformation. Prior parameter variance was calculated based on the assumption that the difference between the upper and lower bound of a parameter group is equal to four standard deviations of its prior probability distribution.

Parameter group	Layer	Initial value	Lower bound	Upper bound	Variance †	Source
Hydraulic conductivity (m/d)	1	0.1	$1e^{-5}$	1	1.562	Aquifer test Logan Approximation
Hydraulic conductivity (m/d)	2	$1e^{-4}$	$1e^{-5}$	$1e^{-3}$	0.25	Aquifer test Logan Approximation
Specific storage (m^{-1})	2	$1e^{-6}$	$1e^{-7}$	$1e^{-5}$	0.25	Li and Cranswick (2016)
Specific yield (-)	1	0.01	0.001	0.05	0.18	Li and Cranswick (2016)
Rainfall-to-recharge ratio (-)	1	0.008	$1e^{-4}$	0.05	0.455	Chloride mass balance

† Based on log-transformed parameter values

The observation groups are detailed in Table 5.2. Prior observation variance was calculated in a similar fashion to the prior parameter variance. The error bounds are assumed to be ±0.2 m for groundwater levels from the observation wells (Rau et al., 2019), ±2 m for groundwater levels derived from TEM and ±50% for prior knowledge of hydraulic conductivity (Logan, 1964). The bounds for the EC and baseflow observation groups are based on the actual range of the AMT data and tracer estimates (Lamontagne et al., 2020). The EC, hydraulic conductivity and baseflow observations were log-transformed. The prior observation variance values were used to derive the random observation ensemble and observation weights, the latter were then adjusted using the program PWTADJ1 (Doherty et al., 1994), which automatically scales the observation weights so that all observation groups are equally visible in the objective function.

Table 5.2 Inversion settings for the observation groups. Prior observation variance was estimated by assuming the difference between the upper and lower bound of an observation is equal to four standard deviations of its prior probability distribution.

Observation group	Unit	Number of observations	Variance
Groundwater levels from observation wells	m asl	42	0.01
Groundwater levels from TEM	m asl	23	1
Zoned EC from AMT †	µS/cm	5	0.008 – 0.03
Prior knowledge of hydraulic conductivity †	m/d	29	0.014
Baseflow to Light River †	m^3/d	1	4.57

† Log-transformed

5.3 Results

5.3.1 History-matching performance

The history-matching performance of the model ensemble for all observation groups is shown in Figure 5.6. For groundwater levels from the observation wells, the residual map shows some potential conflicts between data, where positive residuals are adjacent negative residuals. This may be caused by local heterogeneity given the fractured rock environment, or simply a measurement error, which cannot be resolved with the currently available data. The scatter plot shows a reasonable match between the observed and simulated values, with the cloud of points being cantered around the 1:1 line and a scaled root mean square error (SRMSE, calculated as RMSE divided by the observation range) of 7.3%.

For groundwater levels derived from TEM, both the residual map and scatter plot show an overall overestimation by the model. This potentially suggests that the peak of EC profile may be a sub-optimal indicator of true water table depth. It is possible that the top of the saturated zone may have been diluted by mixing with the relatively fresh rainwater, or there is a significant capillary zone. Nevertheless, an RMSE of 1.3 m is considered to be within the uncertainty bounds of these groundwater level estimates.

Prior knowledge of hydraulic conductivity includes the aquifer test data and Logan Approximation estimates. The prior knowledge functions like regularization in that the objective function is penalized as the modelled values deviate from the prior values. It is worth noting that hydraulic conductivity is a model input, not an output that requires calculation like groundwater levels, and hence is relatively easy to fit. The misfit of hydraulic conductivity between the prior and modelled values is a trade-off for the inversion to fit other observation groups, especially groundwater levels from the observation wells as most of the prior hydraulic conductivity values are located outside the study area. The misfit suggests a potential conflict between these two observation groups, which may be caused by the heterogeneous nature of the fractured rock aquifer and/or errors in the Logan Approximation estimates and groundwater level observations.

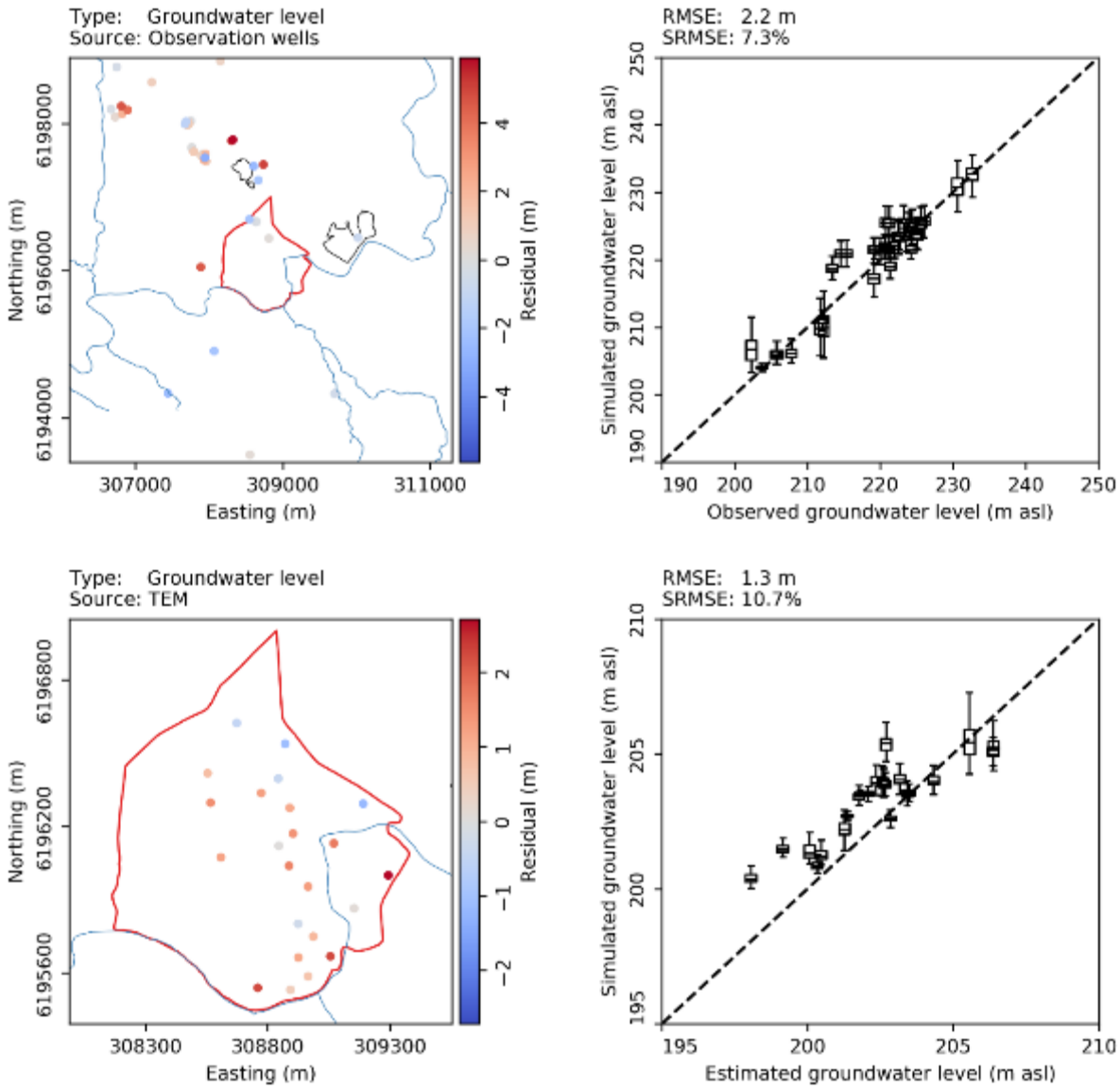

Figure 5.6 History-matching performance of the model ensemble for all observation groups. The left column shows the residual maps, where positive value indicates overestimation and negative value indicates underestimation by the model. The right column shows the scatter plots of simulated against target values. The RMSE and SRMSE were calculated based on the maximum likelihood of the simulated values.

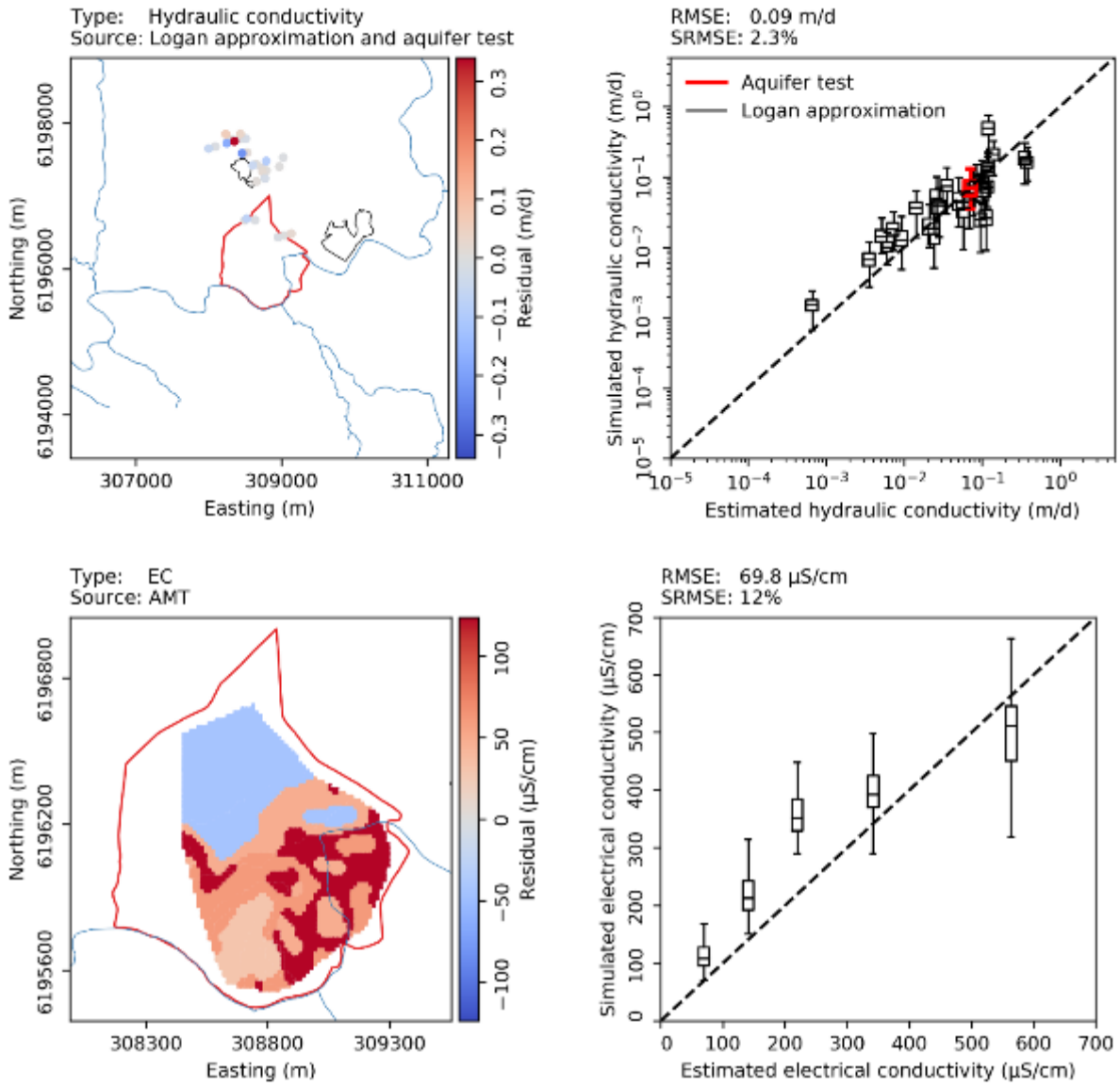

Figure 5.6 (continued) History-matching performance of the model ensemble for all observation groups. The left column shows the residual maps, where positive value indicates overestimation and negative value indicates underestimation by the model. The right column shows the scatter plots of simulated against target values. The RMSE and SRMSE were calculated based on the maximum likelihood of the simulated values.

For the EC observation group, the residual map shows two distinct zones: an underestimated zone to the north and an overestimated zone to the south, which coincide with the location of Tapley Hill Formation and Brighton Limestone respectively. This suggests that using the same petrophysical relationship empirical constants for these two formations is sub-optimal. The fit can be improved by undertaking an additional aquifer test so that a separate set of empirical constants can be derived for each of these formations.

The simulated baseflow to the Light River within the study area in 2019 ranges between 290 and 780 m^3/d with a mean of 560 m^3/d, which is mostly within the tracer estimate range of

400 – 3000 m^3/d (Lamontagne et al., 2020), albeit on the lower end of the range. This discrepancy may be due to the difference in time scale between the tracer and modelled estimates or the riverbed conductance term used.

5.3.2 Posterior parameter distribution and uncertainty

The maximum likelihood and logarithmic standard deviation of the posterior distribution for the calibration parameters are shown in Figure 5.7. Hydraulic conductivity in the weathered layer is higher in the north-eastern part and lower in the south-western part of the study area. Regionally, there is a substantial permeable zone to the east and a less permeable zone to the west of the study area, potentially indicating the differences in the amount of weathering. The unweathered layer typically has a lower hydraulic conductivity, although there is a relatively permeable zone in the north-eastern part of the study area. Specific storage is generally high except to the east and south-east of the study area, while specific yield is higher to the north and lower to the south. The rainfall-to-recharge ratio generally follows topography and is higher in the outer, elevated areas and lower in the centre, low-lying areas.

The logarithmic standard deviation in Figure 5.7 was calculated using parameter values from the 100 model realizations on a cell-by-cell basis and can be used as an indicator of posterior parameter uncertainty, which is highest for hydraulic conductivity in the weathered layer. Its uncertainty is relatively high in the study area, probably due to the limited physical measurements of groundwater level in this area. In contrast, the uncertainty is relatively low near the historical mine, which is probably due to the abundance of Logan Approximation estimates in this area (Figure 5.1). Both hydraulic conductivity in the unweathered layer and specific yield show a relatively high uncertainty in the southern part of the study area, while the uncertainty of specific storage is relatively uniform. Although the uncertainty of rainfall-to-recharge ratio is considerably high in the regional areas, it is relatively low in most part of the study area.

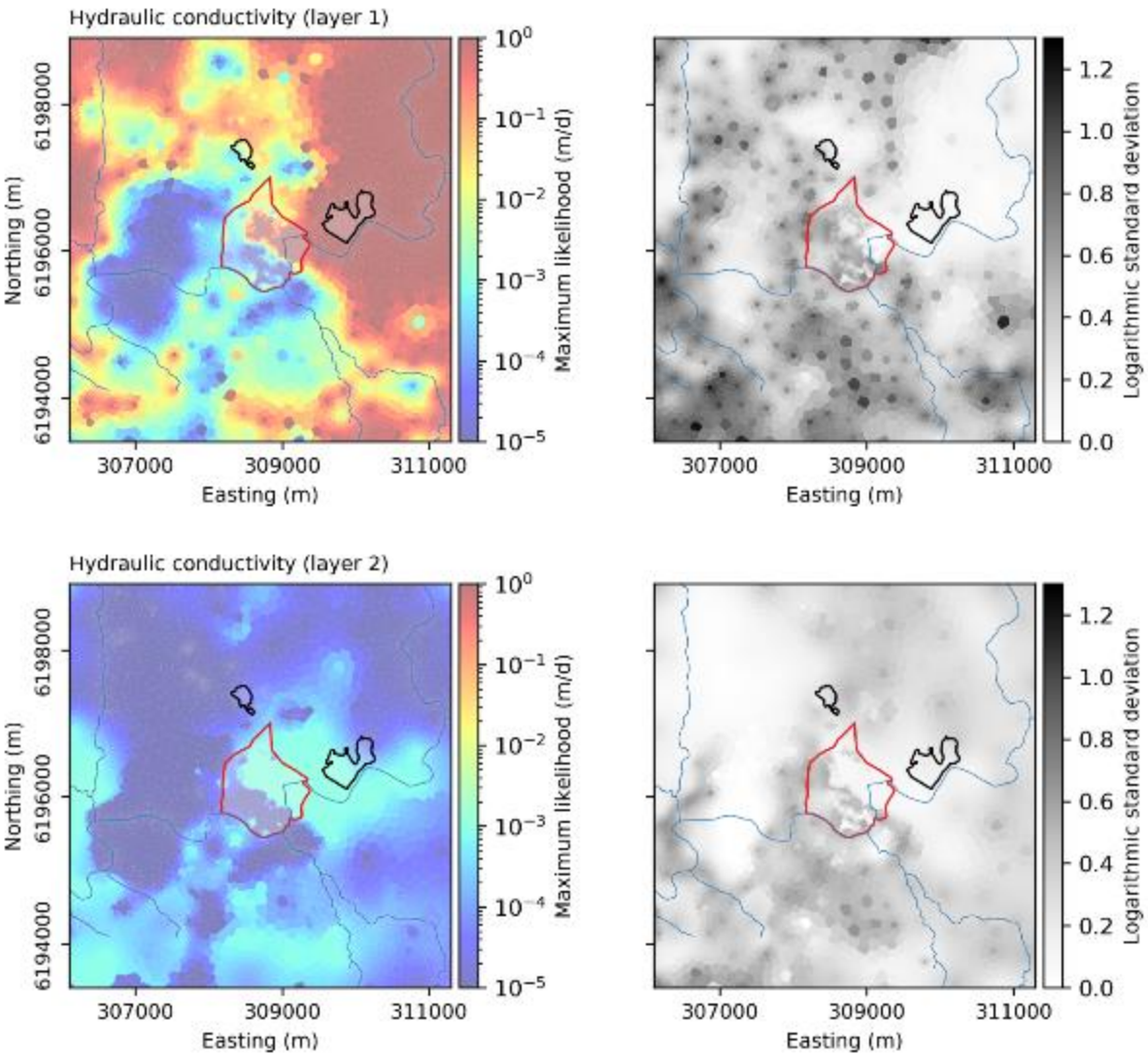

Figure 5.7 The maximum likelihood and logarithmic standard deviation of the posterior distribution for the calibration parameters. The logarithmic standard deviation can be used as an indicator of posterior parameter uncertainty.

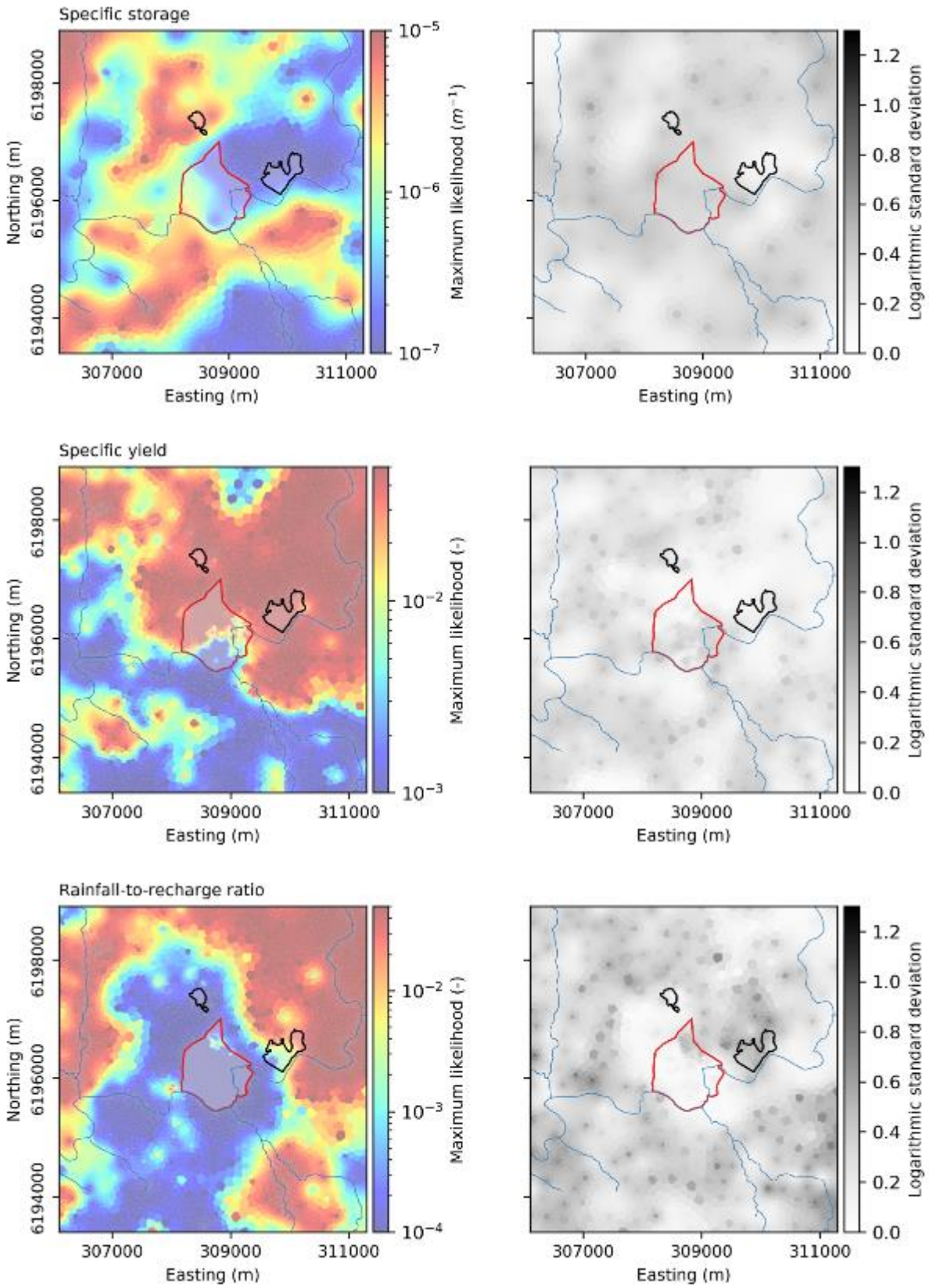

Figure 5.7 (continued) The maximum likelihood and logarithmic standard deviation of the posterior distribution for the calibration parameters. The logarithmic standard deviation can be used as an indicator of posterior parameter uncertainty.

5.3.3 Prediction distribution and uncertainty

The predicted injectant flow paths for the hypothetical SELT operation are shown in Figure 5.8. For an effective porosity of 1%, 95 out of the 100 model realizations indicate that all of the injectant may be retrieved, while 5 realizations show that the injectant has the potential to reach the Light River. For an effective porosity of 5%, 99 out of the 100 model realizations suggest complete removal of the injectant and only 1 realization shows the potential for injectant to reach the river. As the travel speed of injectant is inversely proportional to effective porosity, the injectant travels at a slower speed in the 5% porosity scenario and hence has a higher probability to be completely retrieved. The modelling suggests that it would take 9 to 175 years after the SELT commencement for the injectant to reach the river, with a median of ~35 years. It is important to note that these model runs represent the worst-case scenario as processes such as degradation and attenuation are not considered in the modelling. Also, as the porous medium approach was adopted in this study, results may differ substantially if a fractured rock simulation was considered.

It would be worth noting the fact that the equivalent porous media approach was used here and that results may differ significantly if a fractured rock simulation was considered.

It is worth noting that the injectant under consideration is highly biodegradable. It is expected that ~90% of the injectant will degrade completely within 28 days of exposure to groundwater (Hidalgo et al., 2020, Hidalgo et al., 2019, ECHA, 1999). Our modelling shows no evidence that the injectant can leave the SELT site, much less reach the Light River within this timeframe.

Further analysis was performed on the injectant residence time in the aquifer after the SELT commencement (Figure 5.9). This analysis assumes that the injectant does not degrade with time. For an effective porosity of 1%, the results suggest that most of the injectant may be retrieved between 200 and 400 days after the SELT commencement. This relatively long residence time was unexpected given the small scale of the SELT operation and is likely due to the need of some injectant to travel against the regional groundwater flow gradient to reach the extraction well. The relatively low extraction rate and permeability (compared to sedimentary aquifers) may also contribute to this relatively long residence time. For an effective porosity of 5%, the results indicate that there may still be up to 20% of injectant remaining in the aquifer even after 1000 days, potentially suggesting a longer remediation phase and/or a higher extraction rate may be needed. Again, it is important to note that these residence time results represent the worst-case scenario and do not consider the biodegradability of the injectant.

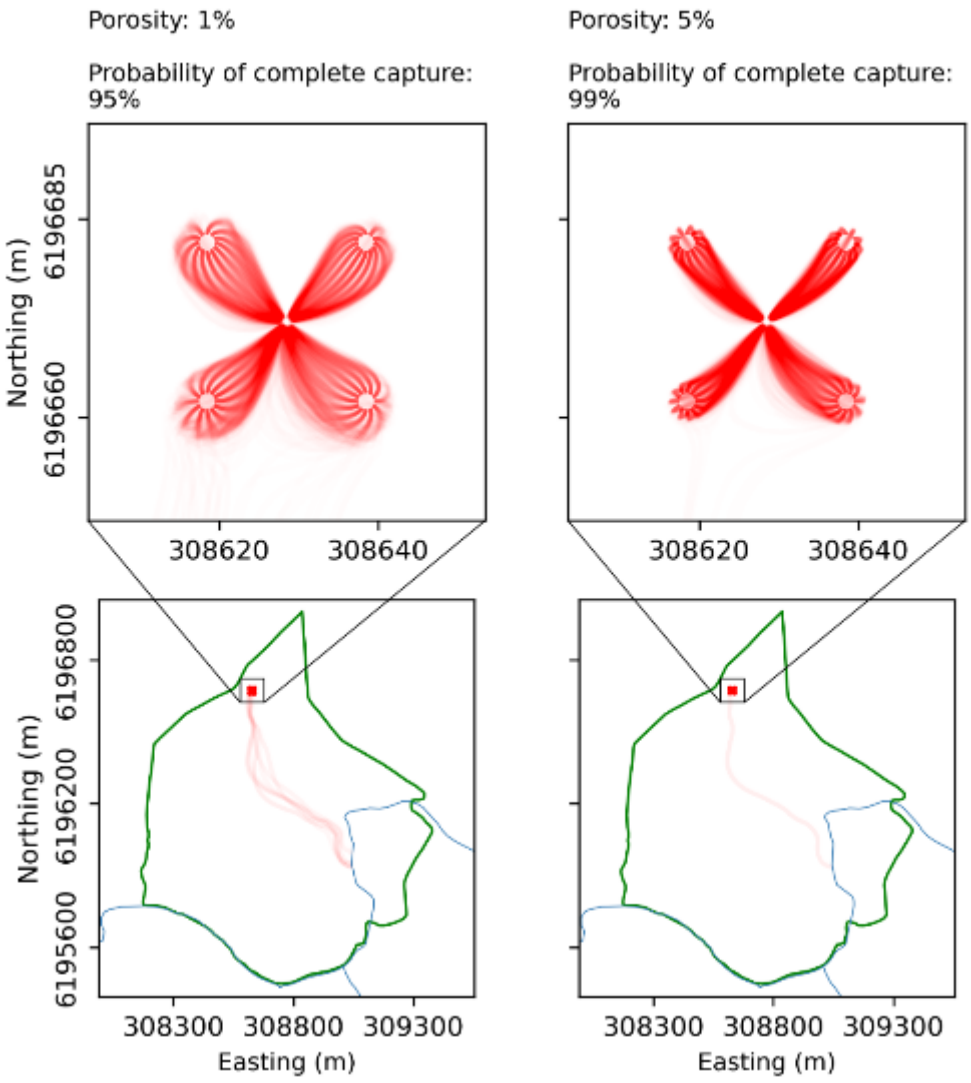

Figure 5.8 Predicted injectant flow paths for the hypothetical SELT operation and the probability of completely capturing the injectant for different effective porosity values of 1% and 5%. Note that the injectant under consideration is highly biodegradable (~90% degradation over 28 days). Our modelling shows no evidence that the injectant can leave the SELT site or reach the Light River within this timeframe. The red lines denote injectant flow paths, the opacity of the red lines denotes likelihood, the green line denotes the study area and the blue line denotes rivers and creeks.

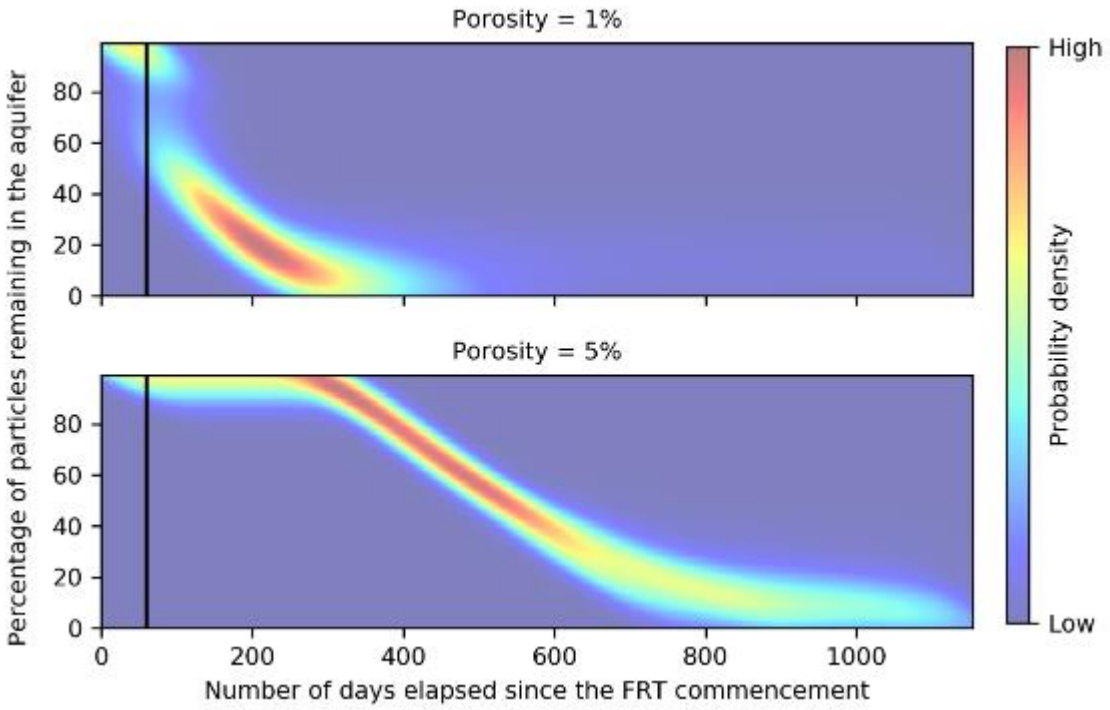

Figure 5.9 Predicted injectant residence time in the aquifer since the SELT commencement for different effective porosity values of 1% and 5%. Note that these residence time results represent the worst-case scenario and do not consider the biodegradability of the injectant (~90% degradation over 28 days). The vertical black line denotes when the SELT ceases.

5.4 Discussion

There are various levels of coupling geophysics and groundwater modeling, ranging from basic manual conceptual interpretation (e.g. Harrington et al., 2014) to sequential inversion (e.g. Christensen et al., 2017) to joint inversion (e.g. Herckenrath et al., 2013). For sequential inversion, outputs from geophysical inversion are used for groundwater model inversion, while for joint inversion both the geophysical and groundwater models are inverted simultaneously. This study performed a relatively complex sequential inversion that uses AMT, TEM and NMR data to constrain stochastic groundwater modeling. This method facilitates the flow of information from geophysical and hydrogeological data to the groundwater model prediction of interest.

The challenge of coupling geophysics with groundwater modeling is that geophysical techniques rarely provide direct information about hydrogeological properties. Additional methods and assumptions, such as petrophysical relationships, are often required to bridge this gap, potentially increasing the uncertainty of geophysically-derived observations, as these relationships may vary depending on local site conditions. When using these observations as targets in groundwater model inversion, it is critical to quantify and account for their uncertainty to avoid incorrectly biasing model outcomes. The ensemble-smoother method potentially provides a means to achieve this via the prior observation variance (Table 5.2), which expresses observation uncertainty as a prior probability distribution. For a given observation, a random sample is drawn from its prior probability distribution for each realisation, forming an ensemble of random observations. This allows the inversion to fit to the observation distribution, which incorporates the observation uncertainty, instead of the observation itself, which may be uncertain especially for the geophysically-derived observations.

There are some limitations in the modeling presented in this paper. Firstly, it is worth noting that the ensemble-smoother method may not necessarily converge to the global minimum of the objective function space, unlike other stochasic methods such as Markov-Chain Monte Carlo. By using the ensemble-smoother method, a compromise is implicitly made where some accuracy in the posterior parameters and predictions is sacrificed for computational efficiency. Secondly, as with most other Bayesian-based techniques, the ensemble-smoother method is dependent on the priors, the derivation of which may sometimes be subjective for geophysically-derived observations. In this study, the TEM data were used to estimate groundwater levels in the study area, which are acknowledged to be uncertain. We assumed the error to be ±2 m and expressed this uncertainty as a prior observation variance (Table 5.2),

which was then incoporated into the groundwater model inversion. This error bound is a subjective estimation based on our hydrogeological knowledge of the area. Nevertheless, we demonstrated how multiple geophysical techniques can be used to provide a large set of soft data to aid groundwater model development, espeically in areas with limited drillhole informatioion, and more importantly, how the uncertainty in these soft data can be expressed in a transparent and repeatable framework that can be reviewed and adjusted as needed.

As for site-specific limitations, there are some areas in the model where the parameters are at their upper bound, especially hydraulic conductivity in the weathered layer and recharge (Figure 5.7). It is hypothesised that the baseflow estimate may be too high, forcing these parameters to reach their upper bound. This hypothesis can be tested by collecting more field data, including baseflow analysis and aquifer tests. Meanwhile, the EC estimates from the AMT inversion were used to provide information on hydraulic conductivity via a petrophysical relationship. This requires calibrating the empirical constants against field data, ideally aquifer test data. Due to the limited aquifer test data in the study area, we assumed the empirical constants to be spatially uniform. The model results suggest that this approach may be sub-optimal when applied across multiple geological formations with variable electrical properties. The model results are likely to be improved if an additional aquifer test was performed so that a separate set of empirical constants could be derived for each of these formations.

5.5 Conclusions

In this study, we coupled multiple geophysical techniques with stochastic groundwater modelling to predict the regional-scale hydrological impact of a hypothetical ISR trial operation for copper recovery in Kapunda, South Australia. The geophysical techniques, including AMT, TEM and NMR, were used to provide constraints on hydraulic conductivity, water table depth, hydrostratigraphy and porosity in a data sparse region. The groundwater model was used as a data assimilation tool to facilitate the flow of information from the geophysical and hydrogeological data to the model prediction of interest. This was achieved using the ensemble-smoother method via PESTPP-IES, which produced an ensemble of 100 calibrated models with a reasonable history-matching performance (an average SRMSE of 7.3% for groundwater level observations). These calibrated models can be considered to represent the posterior distribution of parameters and predictions that can be readily used for non-linear uncertainty analysis and probabilistic predictions. The model ensemble shows no evidence that the injectant can leave the SELT site or reach the Light River within its biodegradation timeframe.

The challenge of coupling geophysics with groundwater modeling is that geophysical techniques rarely provide direct quantification of hydrogeological propoerties. Additional methods, such petrophysical relationships, are required to bridge this gap, potentially increasing the uncertainty of geophysically-derived observations. When using these observations as targets in groundwater model inversion, it is critical to quantify and account for their uncertainty to avoid incorrectly biasing outcomes. The ensemble-smoother method potentially provides a means to achieve this via the prior observation variance and random observation ensemble, allowing the inversion to fit to the observation distribution, which incorporates the observation uncertainty, instead of the observation itself. However, as with most other Bayesian-based techniques, the ensemble-smoother method is dependent on the priors, the derivation of which may sometimes be subjective for geophysically-derived observations. Nevertheless, we demonstrated how multiple geophysical techniques can be used to provide a large set of soft data to aid groundwater model development, espeically in areas with limited drillholes, and more importantly, how the uncertainty in these soft data can be expressed in a transparent and repeatable framework that can be reviewed and adjusted as needed.

Acknowledgements

This research is supported by an Australian Government Research Training Program Scholarship and a CSIRO Research Plus Scholarship. We would like to thank Jeremy White, Matthew Knowling, Luk Peeters, Andrew Taylor, Chris Turnadge and Elliot Grunewald for their technical advice and assistance; Leon Faulkner, Philippa Faulkner, Ben Jeuken and Sébastien Lamontagne for providing site data and information. Geophysical and hydrological data are provided from a CRC-P program entitled “Kapunda In-Situ Copper and Gold Field Recovery Trial”. We thank the landholders and the Light Regional Council for access to undertake measurements. AuScope, Geoscience Australia and CSIRO are thanked for providing access to field equipment.

6 Conclusions

6.1 Summary

The overall objective of this thesis is to investigate how geophysics can be used to assist and improve hydrogeological modelling in a quantitative manner. There are three main contributions to the discipline of hydrogeophysics, which are presented in Chapters 3 to 5.

A coupling method is presented in Chapter 3 to use TEM and surface NMR with limited drillhole data to estimate hydrogeological properties in a non-invasive manner, including groundwater salinity and hydraulic conductivity. This coupling reduces the ambiguity in the hydrogeological interpretations of TEM data by estimating porosity independently using surface NMR and calibrating the empirical constants in Archie's Law against field observations of groundwater salinity. This method was applied to the Calperum floodplain of South Australia to evaluate the impact of artificial watering on the shallow groundwater salinity, which is important for floodplain ecology. The coupling method was upscaled from several geophysical transects to the whole study area using airborne EM data, and the resulting groundwater salinity estimates were found to compare favourably with field observations, except for a few areas which may be influenced by the presence of clay. Despite the lack of aquifer test data for calibration, this work shows that the hydraulic conductivity estimates from surface NMR can still be used in a relative sense to provide insights for hydrogeological investigations.

In Chapter 4, the impact of using TEM and surface NMR to derive hydraulic conductivity on the prediction error and uncertainty of groundwater models was quantified in a sedimentary setting via a synthetic approach. A suite of reference models representing the pre-determined truth was developed for various hydrogeological conditions. Hydrogeological and geophysical data were collected from these reference models and used in different combinations to generate a range of groundwater model ensembles. The performance of these model ensembles was evaluated by comparing their prediction with those of the reference models. It was found that using only TEM to derive hydraulic conductivity via an empirical petrophysical relationship does not necessarily reduce the prediction uncertainty of groundwater models. This appears to be primarily due to two factors: (1) a poorly constrained petrophysical relationship between EC and hydraulic conductivity; and (2) a tendency of the geophysical inversion to slightly over- and under-estimate the EC implicit at model boundaries. However, by including even a few sparse sets of surface NMR data provides better constraints on the petrophysical relationship and greatly reduces the prediction error and uncertainty of groundwater models. This method of

coupling TEM and surface NMR with groundwater modelling can be useful especially in areas with limited aquifer test data.

A modelling framework is presented in Chapter 5 to couple datasets collected using a number of geophysical techniques, including TEM, surface NMR and audio-frequency MT, with stochastic groundwater modelling via the ensemble-smoother method. This framework allows the uncertainty in geophysically-derived observations to be quantified and accounted for in groundwater model inversion by expressing each observation and its associated uncertainty as a prior probability distribution, enabling the inversion to fit to the observation distribution instead of the observation itself. Additionally, the ensemble-smoother method produces an ensemble of different groundwater models that are all calibrated to field data. These models can be considered to represent the posterior distribution of parameters and predictions, which can be readily used for non-linear uncertainty analysis and allows the predictions to be presented in a probabilistic manner. This approach was applied to a scenario based on a potential in-situ recovery site for copper to evaluate the regional-scale impact of a hypothetical operation trial on the local aquifer, including flow paths and residence time of the injectant.

6.2 Future directions

The scientific contributions and advancements made in this thesis bring together two disciplines of geophysics and hydrogeological modelling. A brief overview is given below for further development in the work presented in this thesis.

In Chapter 3, TEM and surface NMR were coupled with limited drillhole data to evaluate the impact of artificial watering on the shallow groundwater salinity in a South Australian River Murray floodplain. Ultimately this was intended to assess the effectiveness of artificial watering in improving the health of floodplain vegetation, which depends on water in both the saturated and unsaturated zone. For the saturated zone, the key factors for vegetation health include water table depth and shallow groundwater salinity, which were successfully addressed in this work by coupling time-lapsed TEM measurements before and after a watering event with the porosity values estimated independently using surface NMR. For the unsaturated zone, the critical factors for vegetation health are water content and salinity. While the TEM data show some changes in EC before and after a watering event in the unsaturated zone, the interpretations of these changes are ambiguous as they can be related to changes in saturation, salinity and clay content. The coupling with surface NMR has limited benefit here as the signal in the unsaturated zone is too small to be detected using currently available surface NMR instrumentation. As instrument specifications advance over time, it will be useful to investigate

how the coupling method presented in Chapter 3 can be applied to the unsaturated zone for ecological health monitoring.

Chapter 4 is a synthetic study that evaluates the impact of using TEM and surface NMR to derive hydraulic conductivity on the prediction accuracy and uncertainty of groundwater models in a sedimentary setting. There is a large degree of uncertainty in petrophysical relationships and their associated empirical constants that are used to derive hydraulic conductivity. These empirical constants are usually calibrated against field data, ideally aquifer test data. However, due to the sporadic nature of aquifer test data and non-uniqueness, there are different combinations of empirical constants that can achieve a similar fit to the aquifer test data. This type of problem can usually be mitigated by reducing the parameter space through the use of upper and lower bounds. However, there is a very limited database of values to provide useful bounds for the empirical constants, leaving a large range of uncertainty in their values. The coupling method presented in Chapter 4 will benefit greatly from more studies of petrophysical relationships and their empirical constants for different hydrogeological conditions. Also, this chapter only considers one reference hydraulic conductivity field. It will be useful to extend this work to multiple reference hydraulic conductivity fields and evaluate whether the conclusion still holds.

A modelling framework is presented in Chapter 5 to couple multiple geophysical techniques with stochastic groundwater modelling. While this framework allows the uncertainty in geophysically-derived observations to be expressed in a manner that can be accounted for in groundwater model inversion, the coupling is performed in a sequential fashion where the geophysical datasets are inverted first, independently of the groundwater model, and these outputs are then used for groundwater modelling. This makes it difficult to assess and quantify the uncertainty in geophysical inversion and how it propagates to and affects the groundwater model. It will be useful to expand the modelling framework presented in Chapter 5 to joint-inversion of geophysical and hydrogeological models, so that the uncertainty propagation between the two model types becomes more transparent.

7 References

AKKER, J. V. D. & WATSON, T. 2017. Bird-in-Hand Gold Project Groundwater Assessment. Adelaide: AGT report 1300-14-TAB.

ALLEN, D., FLAUM, C., RAMAKRISHNAN, T., BEDFORD, J., CASTELIJNS, K., FAIRHURST, D., GUBELIN, G., HEATON, N., MINH, C. C. & NORVILLE, M. A. 2000. Trends in NMR logging. *Oilfield Review,* 12**,** 2-19.

ALLEY, W. M., HEALY, R. W., LABAUGH, J. W. & REILLY, T. E. 2002. Flow and storage in groundwater systems. *Science,* 296**,** 1985-90.

ALMASRI, M. N. & KALUARACHCHI, J. J. 2007. Modeling nitrate contamination of groundwater in agricultural watersheds. *Journal of Hydrology,* 343**,** 211-229.

AMERASINGHE, N., WALTER, T., SLATTER, E., HAMMOND, A. & MULLEN, I. 2011. Calperum Station Groundwater and Salinity Investigation. Canberra: Department of Agriculture, Fisheries and Forestry ABARES.

ANDERSON, M. P., WOESSNER, W. W. & HUNT, R. J. 2015. *Applied groundwater modeling: simulation of flow and advective transport*, Academic press.

ARCHIE, G. E. 1942. The electrical resistivity log as an aid in determining some reservoir characteristics. *Transactions of the American Institute of Mining and Metallurgical Engineers,* 146**,** 54-61.

AUKEN, E., CHRISTIANSEN, A. V., KIRKEGAARD, C., FIANDACA, G., SCHAMPER, C., BEHROOZMAND, A. A., BINLEY, A., NIELSEN, E., EFFERSO, F., CHRISTENSEN, N. B., SORENSEN, K., FOGED, N. & VIGNOLI, G. 2015. An overview of a highly versatile forward and stable inverse algorithm for airborne, ground-based and borehole electromagnetic and electric data. *Exploration Geophysics,* 46**,** 223-235.

BAUER-GOTTWEIN, P., GONDWE, B. N., CHRISTIANSEN, L., HERCKENRATH, D., KGOTLHANG, L. & ZIMMERMANN, S. 2010. Hydrogeophysical exploration of three-dimensional salinity anomalies with the time-domain electromagnetic method (TDEM). *Journal of Hydrology,* 380**,** 318-329.

BEHROOZMAND, A. A., KEATING, K. & AUKEN, E. 2015. A Review of the Principles and Applications of the NMR Technique for Near-Surface Characterization. *Surveys in Geophysics,* 36**,** 27-85.

BOGENES, T., CHAPPEL, S. & KROLIKOWSKI, C. 2003. Kapunda, heritage and tourism. *CAUTHE 2003: Riding the Wave of Tourism and Hospitality Research***,** 1161.

BORMANS, M., MAIER, H., BURCH, M. & BAKER, P. 1998. Temperature stratification in the lower River Murray, Australia: implication for cyanobacterial bloom development. *Marine and Freshwater Research,* 48**,** 647-654.

BOUCHER, M., COSTABEL, S. & YARAMANCI, U. 2011. The detectability of water by NMR considering the instrumental dead time–a laboratory analysis of unconsolidated materials. *Near Surface Geophysics,* 9**,** 145-154.

BOUCHER, M., FAVREAU, G., NAZOUMOU, Y., CAPPELAERE, B., MASSUEL, S. & LEGCHENKO, A. 2012. Constraining groundwater modeling with magnetic resonance soundings. *Ground Water,* 50**,** 775-84.

BRODIE, R. & SAMBRIDGE, M. 2006. A holistic approach to inversion of frequency-domain airborne EM data. *Geophysics,* 71**,** G301-G312.

BRUNETTI, C. & LINDE, N. 2018. Impact of petrophysical uncertainty on Bayesian hydrogeophysical inversion and model selection. *Advances in Water Resources,* 111**,** 346-359.

BRUNNER, P., HENDRICKS FRANSSEN, H. J., KGOTLHANG, L., BAUER-GOTTWEIN, P. & KINZELBACH, W. 2006. How can remote sensing contribute in groundwater modeling? *Hydrogeology Journal,* 15**,** 5-18.

BUREAU OF METEOROLOGY 2018. Climate statistics for Loxton Research Centre (024024).
BUREAU OF METEOROLOGY 2019. Climate statistics for Nuriootpa (023373).
BUREAU OF METEOROLOGY 2020. Climate statistics for Kapunda (023307).
CARDIFF, M., BARRASH, W., DAFFLON, B. & MALAMA, B. 2010. Non-uniqueness in relationships between geophysical and hydrologic parameters: Existence, implications, and improving methods of data integration. *AGUFM,* 2010**,** H23L-01.
CAROTHERS, J. 1968. A statistical study of the formation factor relation to porosity: The Log Analyst, 9.
CARR, H. Y. & PURCELL, E. M. 1954. Effects of Diffusion on Free Precession in Nuclear Magnetic Resonance Experiments. *Physical Review,* 94**,** 630-638.
CHAKKA, K. & MUNSTER, C. 1997. Atrazine and nitrate transport to the brazos river floodplain aquifer. *Transactions of the ASAE,* 40**,** 615-621.
CHEN, Y. & OLIVER, D. S. 2013. Levenberg–Marquardt forms of the iterative ensemble smoother for efficient history matching and uncertainty quantification. *Computational Geosciences,* 17**,** 689-703.
CHRISTENSEN, N. K., FERRE, T. P. A., FIANDACA, G. & CHRISTENSEN, S. 2017. Voxel inversion of airborne electromagnetic data for improved groundwater model construction and prediction accuracy. *Hydrology and Earth System Sciences,* 21**,** 1321-1337.
CHULLIAT, A., MACMILLAN, S., ALKEN, P., BEGGAN, C., NAIR, M., HAMILTON, B., WOODS, A., RIDLEY, V., MAUS, S. & THOMSON, A. 2015. The US/UK world magnetic model for 2015-2020.
COATES, G. R., XIAO, L. & PRAMMER, M. G. 1999. *NMR logging: principles and applications,* Houston, Haliburton Energy Services.
CONNELL, D. & GRAFTON, R. Q. 2011. Water reform in the Murray-Darling Basin. *Water Resources Research,* 47.
CRAIG, J. R., RAMADHAN, M. & MUFFELS, C. 2020. A Particle Tracking Algorithm for Arbitrary Unstructured Grids. *Groundwater,* 58**,** 19-26.
CROSBIE, R. S., MCEWAN, K. L., JOLLY, I. D., HOLLAND, K. L., LAMONTAGNE, S., MOE, K. G. & SIMMONS, C. T. 2009. Salinization risk in semi-arid floodplain wetlands subjected to engineered wetting and drying cycles. *Hydrological Processes,* 23**,** 3440-3452.
CUI, T., MOORE, C. & RAIBER, M. 2018. Probabilistic assessment of the impact of coal seam gas development on groundwater: Surat Basin, Australia. *Hydrogeology Journal,* 26**,** 2357-2377.
DARCY, H. P. G. 1856. *Les Fontaines publiques de la ville de Dijon. Exposition et application des principes à suivre et des formules à employer dans les questions de distribution d'eau, etc*, V. Dalamont.
DAVIES, P. J. & CROSBIE, R. S. 2018. Mapping the spatial distribution of chloride deposition across Australia. *Journal of Hydrology,* 561**,** 76-88.
DOBLE, R., SIMMONS, C., JOLLY, I. & WALKER, G. 2006. Spatial relationships between vegetation cover and irrigation-induced groundwater discharge on a semi-arid floodplain, Australia. *Journal of Hydrology,* 329**,** 75-97.
DOCKER, B. & ROBINSON, I. 2014. Environmental water management in Australia: experience from the Murray-Darling Basin. *International Journal of Water Resources Development,* 30**,** 164-177.
DOHERTY, J. 2003. Ground water model calibration using pilot points and regularization. *Ground water,* 41**,** 170.
DOHERTY, J., BREBBER, L. & WHYTE, P. 1994. PEST: Model-independent parameter estimation. *Watermark Computing, Corinda, Australia,* 122**,** 336.
DOHERTY, J. & SIMMONS, C. T. 2013. Groundwater modelling in decision support: reflections on a unified conceptual framework. *Hydrogeology Journal,* 21**,** 1531-1537.

DOHERTY, J. & VOGWILL, R. 2016. Models, decision-making and science. *Solving the Groundwater Challenges of the 21st Century,* 22**,** 95-113.
DOMENICO, P. & MIFFLIN, M. 1965. Water from low-permeability sediments and land subsidence. *Water Resources Research,* 1**,** 563-576.
DOMENICO, P. A. & SCHWARTZ, F. W. 1998. *Physical and chemical hydrogeology,* New York, Wiley.
ECHA 1999. Biodegradation of Methanesulphonic acid in water: screening tests. Finland.
EVANS, W. & KELLETT, J. 1989. The hydrogeology of the Murray Basin, southeastern Australia. *BMR Journal of Australian Geology and Geophysics,* 11**,** 147-166.
EVERETT, M. E. 2013. *Near-surface applied geophysics*, Cambridge University Press.
FAMIGLIETTI, J. S. 2014. The global groundwater crisis. *Nature Climate Change,* 4**,** 945-948.
FERRÉ, T. P. 2017. Revisiting the relationship between data, models, and decision-making. *Groundwater,* 55**,** 604-614.
FETTER, C. W. 2018. *Applied hydrogeology*, Waveland Press.
FITZPATRICK, A. & MUNDAY, T. 2009. Holistic Conductivity Modelling of the Calperum and Pike Floodplain RESOLVE helicopter electromagnetic surveys. *Water for a healthy Country Flagship Report.*
FREYBERG, D. L. 1988. An exercise in ground-water model calibration and prediction. *Groundwater,* 26**,** 350-360.
FROHLICH, R. K., FISHER, J. J. & SUMMERLY, E. 1996. Electric-hydraulic conductivity correlation in fractured crystalline bedrock: Central Landfill, Rhode Island, USA. *Journal of Applied Geophysics,* 35**,** 249-259.
GARCIA, X. & JONES, A. G. 2002. Atmospheric sources for audio-magnetotelluric (AMT) sounding. *GEOPHYSICS,* 67**,** 448-458.
GARRICK, D., BARK, R., CONNOR, J. & BANERJEE, O. 2012. Environmental water governance in federal rivers: opportunities and limits for subsidiarity in Australia's Murray–Darling River. *Water Policy,* 14**,** 915-936.
GELMAN, A., ROBERTS, G. O. & GILKS, W. R. 1996. Efficient Metropolis jumping rules. *Bayesian statistics,* 5**,** 42.
GELMAN, A. & RUBIN, D. B. 1992. Inference from iterative simulation using multiple sequences. *Statistical science,* 7**,** 457-472.
GEORGE, A. K., WALKER, K. F. & LEWIS, M. M. 2005. Population status of eucalypt trees on the River Murray floodplain, South Australia. *River Research and Applications,* 21**,** 271-282.
GILKS, W. R., RICHARDSON, S. & SPIEGELHALTER, D. 1995. *Markov chain Monte Carlo in practice*, Chapman and Hall/CRC.
GLOVER, P. 2009. What is the cementation exponent? A new interpretation. *The Leading Edge,* 28**,** 82-85.
GLOVER, P., GOMEZ, J., MEREDITH, P., HAYASHI, K., SAMMONDS, P. & MURRELL, S. 1997. Damage of saturated rocks undergoing triaxial deformation using complex electrical conductivity measurements: experimental results. *Physics and Chemistry of the Earth,* 22**,** 57-61.
GLOVER, P. W. J. 2016. Archie's law – a reappraisal. *Solid Earth,* 7**,** 1157-1169.
GLOVER, P. W. J., HOLE, M. J. & POUS, J. 2000. A modified Archie's law for two conducting phases. *Earth and Planetary Science Letters,* 180**,** 369-383.
GUNTHER, T. & MULLER-PETKE, M. 2012. Hydraulic properties at the North Sea island of Borkum derived from joint inversion of magnetic resonance and electrical resistivity soundings. *Hydrology and Earth System Sciences,* 16**,** 3279-3291.
HANKE, M. 1997. A regularizing Levenberg-Marquardt scheme, with applications to inverse groundwater filtration problems. *Inverse Problems,* 13**,** 79-95.

HARBAUGH, A. W. 2005. *MODFLOW-2005, the US Geological Survey modular ground-water model: the ground-water flow process*, US Department of the Interior, US Geological Survey Reston, VA.

HARRINGTON, G. A., GARDNER, W. P. & MUNDAY, T. J. 2014. Tracking Groundwater Discharge to a Large River using Tracers and Geophysics. *Groundwater,* 52**,** 837-852.

HATCH, M., MUNDAY, T. & HEINSON, G. 2010. A comparative study of in-river geophysical techniques to define variations in riverbed salt load and aid managing river salinization. *GEOPHYSICS,* 75**,** WA135-WA147.

HEIGOLD, P. C., GILKESON, R. H., CARTWRIGHT, K. & REED, P. C. 1979. Aquifer Transmissivity from Surficial Electrical Methods. *Ground Water,* 17**,** 338-345.

HERCKENRATH, D., FIANDACA, G., AUKEN, E. & BAUER-GOTTWEIN, P. 2013. Sequential and joint hydrogeophysical inversion using a field-scale groundwater model with ERT and TDEM data. *Hydrology and Earth System Sciences,* 17**,** 4043.

HERCZEG, A., DOGRAMACI, S. & LEANEY, F. 2001. Origin of dissolved salts in a large, semi-arid groundwater system: Murray Basin, Australia. *Marine and Freshwater Research,* 52**,** 41-52.

HIDALGO, T., KUHAR, L., BEINLICH, A. & PUTNIS, A. 2019. Kinetics and mineralogical analysis of copper dissolution from a bornite/chalcopyrite composite sample in ferric-chloride and methanesulfonic-acid solutions. *Hydrometallurgy,* 188**,** 140-156.

HIDALGO, T., VERRALL, M., BEINLICH, A., KUHAR, L. & PUTNIS, A. 2020. Replacement reactions of copper sulphides at moderate temperature in acidic solutions. *Ore Geology Reviews,* 123**,** 103569.

HILL, H. J. & MILBURN, J. 1956. Effect of clay and water salinity on electrochemical behavior of reservoir rocks.

HILL, M. C. & TIEDEMAN, C. R. 2006. *Effective groundwater model calibration: with analysis of data, sensitivities, predictions, and uncertainty*, John Wiley & Sons.

HØJBERG, A. & REFSGAARD, J. 2005. Model uncertainty–parameter uncertainty versus conceptual models. *Water Science and Technology,* 52**,** 177-186.

HOLLAND, K. L., JOLLY, I. D., OVERTON, I. C. & WALKER, G. R. 2009. Analytical model of salinity risk from groundwater discharge in semi-arid, lowland floodplains. *Hydrological Processes,* 23**,** 3428-3439.

HUNT, R. J. & ZHENG, C. M. 2012. The Current State of Modeling. *Ground Water,* 50**,** 329-333.

JAIN, A. K. 2010. Data clustering: 50 years beyond K-means. *Pattern recognition letters,* 31**,** 651-666.

JEUKEN, B. & MAGAREY, P. 2017. Kapunda Copper Project - Baseline Hydrogeological Assessment. Adelaide: Groundwater Science.

JOLLY, I. D., WALKER, G. R. & THORBURN, P. J. 1993. Salt accumulation in semi-arid floodplain soils with implications for forest health. *Journal of Hydrology,* 150**,** 589-614.

JOYCE, S., HARTLEY, L., APPLEGATE, D., HOEK, J. & JACKSON, P. 2014. Multi-scale groundwater flow modeling during temperate climate conditions for the safety assessment of the proposed high-level nuclear waste repository site at Forsmark, Sweden. *Hydrogeology Journal,* 22**,** 1233-1249.

KELBERT, A., MEQBEL, N., EGBERT, G. D. & TANDON, K. 2014. ModEM: A modular system for inversion of electromagnetic geophysical data. *Computers & Geosciences,* 66**,** 40-53.

KENYON, W., DAY, P., STRALEY, C. & WILLEMSEN, J. 1988. A three-part study of NMR longitudinal relaxation properties of water-saturated sandstones. *SPE formation evaluation,* 3**,** 622-636.

KINGSFORD, R. T. 2000. Ecological impacts of dams, water diversions and river management on floodplain wetlands in Australia. *Austral Ecology,* 25**,** 109-127.

KNIGHT, R., GRUNEWALD, E., IRONS, T., DLUBAC, K., SONG, Y. Q., BACHMAN, H. N., GRAU, B., WALSH, D., ABRAHAM, J. D. & CANNIA, J. 2012. Field experiment provides ground truth

for surface nuclear magnetic resonance measurement. *Geophysical Research Letters,* 39.

KNIGHT, R., WALSH, D. O., BUTLER, J. J., JR., GRUNEWALD, E., LIU, G., PARSEKIAN, A. D., REBOULET, E. C., KNOBBE, S. & BARROWS, M. 2016. NMR Logging to Estimate Hydraulic Conductivity in Unconsolidated Aquifers. *Ground Water,* 54**,** 104-14.

KOSINSKI, W. K. & KELLY, W. E. 1981. Geoelectric Soundings for Predicting Aquifer Properties. *Ground Water,* 19**,** 163-171.

LAMBERT, I. B., DONNELLY, T. H. & ROWLANDS, N. J. 1980. Genesis of upper proterozoic stratabound copper mineralization, Kapunda, South Australia. *Mineralium Deposita,* 15**,** 1-18.

LAMONTAGNE, S., KIRBY, J. & JOHNSTON, C. 2020. Groundwater – surface water connectivity in a chain-of-ponds semiarid river. *Manuscript submitted for publication*.

LEGCHENKO, A., BALTASSAT, J. M., BEAUCE, A. & BERNARD, J. 2002. Nuclear magnetic resonance as a geophysical tool for hydrogeologists. *Journal of Applied Geophysics,* 50**,** 21-46.

LEGCHENKO, A., EZERSKY, M., CAMERLYNCK, C., AL-ZOUBI, A. & CHALIKAKIS, K. 2009. Joint use of TEM and MRS methods in a complex geological setting. *Comptes Rendus Geoscience,* 341**,** 908-917.

LI, C. & CRANSWICK, R. H. 2016. Barossa PWRA Groundwater Resource Capacity: Numerical Groundwater Flow Modelling. Adelaide: DEWNR Technical Report 2016/05.

LI, C., DOBLE, R., HATCH, M. & HEINSON, G. 2020. Investigating the impact of artificial environmental watering on a semi-arid, highly saline floodplain using electromagnetics and surface nuclear magnetic resonance. *Hydrological Processes,* 34**,** 2337-2350.

LOGAN, J. 1964. Estimating transmissibility from routine production tests of water wells. *Groundwater,* 2**,** 35-37.

LONG, J., REMER, J., WILSON, C. & WITHERSPOON, P. 1982. Porous media equivalents for networks of discontinuous fractures. *Water Resources Research,* 18**,** 645-658.

LUBCZYNSKI, M. & ROY, J. 2003. Hydrogeological interpretation and potential of the new magnetic resonance sounding (MRS) method. *Journal of Hydrology,* 283**,** 19-40.

MAHESHWARI, B., WALKER, K. & MCMAHON, T. 1995. Effects of regulation on the flow regime of the River Murray, Australia. *Regulated Rivers: Research & Management,* 10**,** 15-38.

MARKER, P. A., FOGED, N., HE, X., CHRISTIANSEN, A. V., REFSGAARD, J. C., AUKEN, E. & BAUER-GOTTWEIN, P. 2015. Performance evaluation of groundwater model hydrostratigraphy from airborne electromagnetic data and lithological borehole logs. *Hydrology and Earth System Sciences,* 19**,** 3875-3890.

MAURER, J. & KNIGHT, R. 2016. Models and methods for predicting hydraulic conductivity in near-surface unconsolidated sediments using nuclear magnetic resonance. *Geophysics,* 81**,** D503-D518.

MCKENNA, S. A., DOHERTY, J. & HART, D. B. 2003. Non-uniqueness of inverse transmissivity field calibration and predictive transport modeling. *Journal of Hydrology,* 281**,** 265-280.

MEIBOOM, S. & GILL, D. 1958. Modified spin-echo method for measuring nuclear relaxation times. *Review of scientific instruments,* 29**,** 688-691.

MERRICK, D. 2016. AlgoMesh User Guide. Australian Capital Territory: HydroAlgorithmics.

MOONEY, C. & TAN, P.-L. 2012. South Australia's River Murray: Social and cultural values in water planning. *Journal of Hydrology,* 474**,** 29-37.

MOORE, C. & DOHERTY, J. 2005. Role of the calibration process in reducing model predictive error. *Water Resources Research,* 41.

MOORE, C. R., DOHERTY, J., HOWELL, S. & ERRIAH, L. 2015. Some Challenges Posed by Coal Bed Methane Regional Assessment Modeling. *Groundwater,* 53**,** 737-747.

MOORE, W. R., MA, Y. Z., URDEA, J., BRATTON, T., MA, Y. Z. & LA POINTE, P. R. 2011. Uncertainty Analysis in Well-Log and Petrophysical Interpretations. *Uncertainty Analysis and Reservoir Modeling.* American Association of Petroleum Geologists.

NARAYAN, K. A., SCHLEEBERGER, C. & BRISTOW, K. L. 2007. Modelling seawater intrusion in the Burdekin Delta Irrigation Area, North Queensland, Australia. *Agricultural Water Management,* 89**,** 217-228.

NIROLA, R., MEGHARAJ, M., ARYAL, R. & NAIDU, R. 2016. Screening of metal uptake by plant colonizers growing on abandoned copper mine in Kapunda, South Australia. *International Journal of Phytoremediation,* 18**,** 399-405.

PANDAY, S., LANGEVIN, C. D., NISWONGER, R. G., IBARAKI, M. & HUGHES, J. D. 2017. MODFLOW-USG version 1.4.00: An unstructured grid version of MODFLOW for simulating groundwater flow and tightly coupled processes using a control volume finite-difference formulation. United States: U.S. Geological Survey.

PARASNIS, D. S. 2012. *Principles of applied geophysics*, Springer Science & Business Media.

POETER, E. P., HILL, M. C., LU, D., TIEDEMAN, C. & MEHL, S. W. 2014. UCODE_2014, with new capabilities to define parameters unique to predictions, calculate w eights using simulated values, estimate parameters w ith SVD, evaluate uncertainty with MCMC, and more. Integrated Groundwater Modeling Center (IGWMC), of the Colorado School of Mines.

PONZINI, G., OSTROMAN, A. & MOLINARI, M. 1984. Empirical Relation between Electrical Transverse Resistance and Hydraulic Transmissivity. *Geoexploration,* 22**,** 1-15.

POSTMA, D., LARSEN, F., MINH HUE, N. T., DUC, M. T., VIET, P. H., NHAN, P. Q. & JESSEN, S. 2007. Arsenic in groundwater of the Red River floodplain, Vietnam: Controlling geochemical processes and reactive transport modeling. *Geochimica et Cosmochimica Acta,* 71**,** 5054-5071.

PURVANCE, D. T. & ANDRICEVIC, R. 2000. On the electrical-hydraulic conductivity correlation in aquifers. *Water Resources Research,* 36**,** 2905-2913.

RAMSAR CONVENTION BUREAU 1971. Convention on Wetlands of International Importance especially as Waterfowl Habitat. Iran: Ramsar Iran.

RAU, G. C., POST, V. E., SHANAFIELD, M., KREKELER, T., BANKS, E. W. & BLUM, P. 2019. Error in hydraulic head and gradient time-series measurements: a quantitative appraisal. *Hydrology & Earth System Sciences,* 23.

RIVERO, O. G. Some considerations about the possible use of the parameters a and m as a formation evaluation tool through well logs. SPWLA 18th annual logging symposium, 1977. Society of Petrophysicists and Well-Log Analysts.

ROBERTS, G. O., GELMAN, A. & GILKS, W. R. 1997. Weak convergence and optimal scaling of random walk Metropolis algorithms. *The annals of applied probability,* 7**,** 110-120.

ROHDE, M. M., FROEND, R. & HOWARD, J. 2017. A Global Synthesis of Managing Groundwater Dependent Ecosystems Under Sustainable Groundwater Policy. *Ground Water,* 55**,** 293-301.

RUBIN, Y. & HUBBARD, S. S. 2006. *Hydrogeophysics*, Springer Science & Business Media.

RUSHTON, K. R. & REDSHAW, S. C. 1979. *Seepage and groundwater flow: Numerical analysis by analog and digital methods*, John Wiley & Sons.

SCHIROV, M., LEGCHENKO, A. & CREER, G. 1991. A new direct non-invasive groundwater detection technology for Australia. *Exploration Geophysics,* 22**,** 333-338.

SEN, P. N., STRALEY, C., KENYON, W. E. & WHITTINGHAM, M. S. 1990. Surface-to-volume ratio, charge density, nuclear magnetic relaxation, and permeability in clay-bearing sandstones. *GEOPHYSICS,* 55**,** 61-69.

SHAPIRO, S. S. & WILK, M. B. 1965. An analysis of variance test for normality. *Biometrika,* 52**,** 591-611.

SHIKLOMANOV, I. 1993. World fresh water resources, water in crisis: A guide to the world's fresh water resources. Oxford University Press, New York.

SIEBERT, S., BURKE, J., FAURES, J.-M., FRENKEN, K., HOOGEVEEN, J., DÖLL, P. & PORTMANN, F. T. 2010. Groundwater use for irrigation—a global inventory. *Hydrology and earth system sciences,* 14**,** 1863-1880.

SINCLAIR, L. & THOMPSON, J. 2015. In situ leaching of copper: Challenges and future prospects. *Hydrometallurgy,* 157**,** 306-324.

SLATER, L. 2007. Near Surface Electrical Characterization of Hydraulic Conductivity: From Petrophysical Properties to Aquifer Geometries—A Review. *Surveys in Geophysics,* 28**,** 169-197.

SPIES, B. R. 1989. Depth of investigation in electromagnetic sounding methods. *GEOPHYSICS,* 54**,** 872-888.

STEGGLES, T. & TUCKER, P. 2003. *The management of Lake Merreti : using past experiences to guide future practices*, Australian Landscape Trust.

TELFORD, W. M., GELDART, L. & SHERIFF, R. E. 1990. *Applied geophysics*, Cambridge university press.

TIAB, D. & DONALDSON, E. C. 2015. *Petrophysics: theory and practice of measuring reservoir rock and fluid transport properties*, Gulf professional publishing.

TOCKNER, K. & STANFORD, J. A. 2002. Riverine flood plains: present state and future trends. *Environmental Conservation,* 29**,** 308-330.

TODD, D. K. 1980. *Groundwater hydrology*.

VILHELMSEN, T. N., BEHROOZMAND, A. A., CHRISTENSEN, S. & NIELSEN, T. H. 2014. Joint inversion of aquifer test, MRS, and TEM data. *Water Resources Research,* 50**,** 3956-3975.

VILHELMSEN, T. N., CHRISTENSEN, S. & AUKEN, E. 2016. On determining uncertainties of magnetic resonance sounding estimated transmissivities for groundwater modeling. *GEOPHYSICS,* 81**,** WB63-WB73.

VISTA CLARA 2015. GMR Manual and Documentation. United States.

VOZOFF, K. 1991. The magnetotelluric method. *Electromagnetic Methods in Applied Geophysics: Volume 2, Application, Parts A and B.* Society of Exploration Geophysicists.

WAGNER, A. M. 2007. *Using Geophysical Constraints To Determine Groundwater Travel Times, Seafloor Arrival Locations, And Saltwater Concentrations For Transition Zone Depths At Underground Nuclear Detonations On Amchitka Island*.

WALSH, D. O. 2008. Multi-channel surface NMR instrumentation and software for 1D/2D groundwater investigations. *Journal of Applied Geophysics,* 66**,** 140-150.

WALSH, D. O., GRUNEWALD, E., TURNER, P., HINNELL, A. & FERRE, P. 2011. Practical limitations and applications of short dead time surface NMR. *Near Surface Geophysics,* 9**,** 103-111.

WELTER, D. E., WHITE, J. T., HUNT, R. J. & DOHERTY, J. E. 2015. Approaches in highly parameterized inversion—PEST++ Version 3, a Parameter ESTimation and uncertainty analysis software suite optimized for large environmental models. US Geological Survey.

WERNER, A. D. & LAATTOE, T. 2016. Terrestrial freshwater lenses in stable riverine settings: Occurrence and controlling factors. *Water Resources Research,* 52**,** 3654-3662.

WHITE, J. T. 2018. A model-independent iterative ensemble smoother for efficient history-matching and uncertainty quantification in very high dimensions. *Environmental Modelling & Software,* 109**,** 191-201.

WINSAUER, W. O., SHEARIN, H. M., MASSON, P. H. & WILLIAMS, M. 1952. Resistivity of Brine-Saturated Sands in Relation to Pore Geometry. *Aapg Bulletin-American Association of Petroleum Geologists,* 36**,** 253-277.

WOOD, W. W. 1999. Use and misuse of the chloride-mass balance method in estimating ground water recharge. *Ground water,* 37**,** 2-5.

ZGHIBI, A., ZOUHRI, L., CHENINI, I., MERZOUGUI, A. & TARHOUNI, J. 2016. Modelling of the groundwater flow and of tracer movement in the porous and fissured media: Chalk Aquifer (Northern part of Paris Basin, France). *Hydrological Processes,* 30**,** 1916-1928.